Lehrstuhl E15
Physik - Department

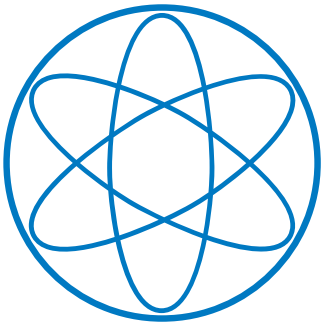

New ^{8}B Neutrino Spectroscopy in Borexino and Search for Sterile Neutrinos

Dissertation
von

Simon Appel

Technische Universität
München

Technische Universität München

TUM School of Natural Sciences

New ^{8}B Neutrino Spectroscopy in Borexino and Search for Sterile Neutrinos

Simon Appel

Vollständiger Abdruck der von der TUM School of Natural Sciences der Technischen Universität München zur Erlangung eines

Doktors der Naturwissenschaften (Dr. rer. nat.)

genehmigten Dissertation.

Vorsitz:	apl. Prof. Dr. Norbert Kaiser
Prüfer*innen der Dissertation:	1. Prof. Dr. Lothar Oberauer
	2. Prof. Dr. Elisa Resconi

Die Dissertation wurde am 11.08.2022 bei der Technischen Universität München eingereicht und durch die TUM School of Natural Sciences am 01.06.2023 angenommen.

Abstract

The work presented in this thesis is based on the solar neutrino experiment Borexino and the reactor neutrino experiment Double Chooz. Both experiments are sensitive to sterile neutrinos which are motivated by several oscillation experiments that are not compatible with the three neutrino case.
Borexino has an active volume of $\approx 300\,\mathrm{t}$ scintillator. It is placed in the Laboratori Nazionali del Gran Sasso (LNGS) with a rock coverage of 3800 meter water equivalent. Borexino is sensitive to all solar neutrinos. This work focuses on the ^{8}B solar neutrinos. The internal background consists mainly of ^{208}Tl decays, which is determined via the branching of the ^{212}Bi –^{212} Po coincidence. The external background is caused by ^{208}Tl and ^{214}Bi decays with gamma energies up to 3.2 MeV. They define the threshold of the analysis at 3 MeV. Cosmic muons muons are identified via Borexino's optically separated subdetectors with an efficiency close to one. Through spallation on ^{12}C cosmogenic radiosotopes are created as secondary background, which can be partly vetoed by two different time windows after a muon. Special care was given to the long lived ^{11}Be which is partly contained in the longer time window . However $(3.2 \pm 0.6) \cdot 10^{-3}\,\mathrm{cpd}/100\,\mathrm{t}$ events survive the veto. Within the inner 3 m a simple counting analysis is possible which gives a ^{8}B neutrino rate of $0.24 \pm 0.01\,\mathrm{cpd}/100\,\mathrm{t}$. In a further step the fiducial volume could be increased to the full sensitive volume. Probability density functions (pdf) containing the spectral and radial distributions of the signal and background were created via monte carlo. The pdf's were fitted to the dataset resulting in a neutrino count rate of $0.24 \pm 0.01\,\mathrm{cpd}/100\,\mathrm{t}$. Sterile neutrinos would change the neutrino's survival probability. The simulation was adjusted accordingly and the changed model compared to the MSW-LMA solution. No hints for sterile neutrinos were found.
The Double Chooz experiment consists of two identical detectors with a baseline of 1050 m and 400 m, respectively, to the Chooz B reactor in France. It detects reactor antineutrinos via the inverse beta decay. Its main goal is to measure the mixing angle θ_{13}, which was measured to be $\sin^2\theta_{13} = 0.105 \pm 0.014$. The precision on the proton number is dominating the uncertainty of θ_{13}. During decommissioning the scintillator mass was measured and the uncertainty of the proton number could be reduced by a factor of two. Double Chooz is also sensitive to sterile neutrinos. The search for sterile neutrinos is based on a likelihood fit that relies on the comparison of the near and far detector data. No disappearance in addition to the three neutrino case was found.

Zusammenfassung

Die vorliegende Arbeit basiert auf dem solaren Neutrinoexperiment Borexino und dem Reaktorneutrinoexperiment Double Chooz. Beide Experimente sind sensitiv für sterile Neutrinos, die durch verschiedene Oszillationsexperimente motiviert sind, die nicht mit dem Drei-Neutrino-Fall vereinbar sind. Borexino hat ein aktives Volumen von $\approx 300\,\mathrm{t}$ Szintillator. Es befindet sich im Laboratori Nazionali del Gran Sasso (LNGS) mit einer Abschirmung von 3800 Meter Wasseräquivalent. Borexino ist sensitiv für alle solaren Neutrinos. Diese Arbeit konzentriert sich auf die solaren ^{8}B-Neutrinos. Der interne Untergrund besteht hauptsächlich aus ^{208}Tl-Zerfällen, die über die Verzweigung der ^{212}Bi –^{212} Po Koinzidenz bestimmt werden. Der externe Untergrund wird durch ^{208}Tl- und ^{214}Bi-Zerfälle mit Gammaenergien bis zu 3,2 MeV verursacht. Sie definieren die Schwelle der Analyse bei 3 MeV. Kosmische Myonen werden über die optisch getrennten Subdetektoren von Borexino mit einer Effizienz nahe eins identifiziert. Durch Spallation an ^{12}C entstehen kosmogene Radiosotope als sekundärer Untergrund, die durch zwei unterschiedliche Zeitfenster nach einem Myon teilweise gevetot werden können. Besondere Aufmerksamkeit wurde dem langlebigen ^{11}Be gewidmet, das teilweise im längeren Zeitfenster enthalten ist. Allerdings überleben $(3,2 \pm 0,6) \cdot 10^{-3}\,\mathrm{cpd}/100\,\mathrm{t}$ Ereignisse das Veto. Innerhalb der inneren 3 m ist eine einfache Zählanalyse möglich, die eine ^{8}B-Neutrinorate von $0,24 \pm 0,01\,\mathrm{cpd}/100\,\mathrm{t}$ ergibt. In einem weiteren Schritt könnte das Volumen auf das volle empfindliche Volumen vergrößert werden. Wahrscheinlichkeitsdichtefunktionen (pdf), die die spektralen und radialen Verteilungen des Signals und des Untergrunds enthalten, wurden mittels Monte Carlo erstellt. Die pdfs wurden an den Datensatz gefittet, was zu einer Neutrino-Zählrate von $0,24 \pm 0,01\,\mathrm{cpd}/100\,\mathrm{t}$ führte. Sterile Neutrinos würden die Überlebenswahrscheinlichkeit des Neutrinos verändern. Die Simulation wurde entsprechend angepasst und das geänderte Modell mit der MSW-LMA-Lösung verglichen. Es wurden keine Hinweise auf sterile Neutrinos gefunden.
Das Double Chooz Experiment besteht aus zwei identischen Detektoren mit einer Distanz von 1050 m bzw. 400 m zum Chooz B Reaktor in Frankreich. Es weist Reaktor-Antineutrinos über den inversen Betazerfall nach. Sein Hauptziel ist die Messung des Mischungswinkels θ_{13}, der mit $\sin^2\theta_{13} = 0,105 \pm 0,014$ gemessen wurde. Die Genauigkeit der Protonenzahl dominiert die Unsicherheit von θ_{13}. Während des Abbaus wurde die Szintillatormasse gemessen und die Unsicherheit der Protonenzahl konnte um den Faktor zwei verringert werden. Double Chooz ist auch sensitiv für sterile Neutrinos. Die

Suche nach sterilen Neutrinos basiert auf einem Likelihood-Fit, der sich auf den Vergleich der Daten des nahen und fernen Detektors stützt. Es wurde keine Oszillation zusätzlich zum Fall der drei Neutrinos gefunden.

Contents

Chapter 1

Introduction

In 1930 Pauli introduced the neutrino as a way to preserve energy and spin in the β decay of radioactive nuclei. Afterwards during 1956 Cowan and Reines were the first to detect neutrinos [1] and thus founded a new field of physics. While first experiments used reactors as neutrino sources Davies was the first one to detect solar neutrinos in 1968 [2].
In the aftermath of these discoveries several astonishing properties of the neutrinos were revealed, with the solar neutrino problem [3] being the most established one. There was an unexpectedly low rate of observed solar neutrinos, which finally could be resolved by the introduction of neutrino flavor oscillations[4]. Later on this new mechanism was confirmed by reactor experiments [5] and via atmospheric neutrino oscillations [6]. Nevertheless several properties of the neutrino remain unknown. The absolute mass scale of the neutrino mass eigenstates, their ordering, and the size of a possibly CP violating phase δ of the mixing matrix are still open questions[7]. Furthermore, it could not be verified if neutrinos are of Dirac or Majorana nature [8].

As neutrinos interact only weakly and thus are hardly affected by matter, they point directly to their source which renders them excellent messengers. These properties allow to investigate astrophysical phenomena, like solar fusion, supernovae and radiogenic heat production in the Earth.
However, the low cross section of neutrino interactions requires huge detectors, including severe understanding of the device's performance and well established background models.
Thus, the Borexino detector [9], that started data acquisition in 2007, was built. It is designed to perform real time solar neutrino spectroscopy. Due to its high light yield and record high radiopurity the experiment spawned terrific results. It is the first detector to measure all neutrinos of the pp-chain

except the least abundant hep neutrinos[10, 11] . Furthermore it yielded the best limit on the CNO neutrino flux [12] and a spectroscopic measurement of geo neutrinos [13].
The first chapter gives a brief overview of neutrino oscillation, neutrino sources and introduces sterile neutrinos. Chapter 1.8 introduces the Water-Čerenkov technology. In chapter 2 the set up of Borexino and its results are presented. The detection channel of Borexino and the data set used in this work are described. The following chapter 4 introduces internal backgrounds. Muons as backgrounds and isotopes created by them are handled in chapter 5. A simple counting analysis of solar neutrinos is presented in chapter 6. A analysis based on the whole detector volume is discussed in chapter 7. Searches for sterile neutrinos based on the ^{8}B neutrino spectrum are presented in chapter 8. Chapter 9 introduces the upcoming JUNO detector and its possibilities for solar ^{8}B detection. The reactor neutrino experiment Double Chooz, its capabilities for a sterile neutrino search and an improvement of the experiment's systematic are presented in chapter 10 . A overview of the current situation of the search for sterile neutrinos is given in chapter 11. The present work is based on data generated by the Borexino experiment.

1.1 Neutrinos in the Standard Model

The Standard Model of Particle Physics (SM) is described via a local SU(3)× SU(2)×SU(1) gauge symmetry of a quantum field theory. The SU(3) depicts the strong force, the SU(2) the weak force and the SU(1) the electromagnetic force [7]. Furthermore the weak and electromagnetic force can be combined via an SU(2)×SU(1) gauge group, introducing electroweak interactions[14]. Gravitation, being the fourth fundamental force, could not be included in this model yet. However, gravitational effects are insignificant compared to the other three forces, so the SM is able to give a precise predictions of particle interactions.
According to the standard model leptons and antileptons are divided in three generations, each consisting of a charged lepton and a neutral, massless neutrino, where the neutrino just undergoes the weak SU(2) interaction. The left handed fermions form duplets under SU(2), while the right handed fermions so far are described as a singlet[7]. So the fermions are arranged as:

$$\begin{pmatrix} \mathrm{e} \\ \nu_\mathrm{e} \end{pmatrix}_\mathrm{L} \begin{pmatrix} \mu \\ \nu_\mu \end{pmatrix}_\mathrm{L} \begin{pmatrix} \tau \\ \nu_\tau \end{pmatrix}_\mathrm{L}, \mathrm{e}_\mathrm{R}, \mu_\mathrm{R}, \tau_\mathrm{R} \tag{1.1}$$

with L and R indicating the left-and right-handyness of the particle. The weak interaction is induced via Charged current (CC) reactions, by exchange

of a $W^{\pm}$ ($m_W = 80\,\mathrm{GeV}$) that can change the particle type within one generation, while neutral current (NC) reactions, by Z^0 ($m_Z = 92\,\mathrm{GeV}$) exchange don't affect the particle type. As a result of Heisenberg's uncertainty principle these high masses of the exchange bosons result in the short range of the weak interaction. The weak interaction is maximally parity violating, therefore Z^0 and $W^{\pm}$ just couple to left handed particles and right handed antiparticles. This renders it impossible to generate mass via the standard Higgs mechanism, as the Yukawa interactions needed require left- and right-handed interactions, therefore the masslessness of neutrinos in the SM. Hence, the neutrino is always in a pure chirality eigenstate. But there are several experiments on atmospheric[15], solar [4] and reactor neutrinos [5] that prove this model to be incomplete as they have observed flavor changing oscillations. This also implies, that at least two neutrinos do have a rest mass.

1.2 Vacuum Oscillations

In 1962, Maki, Nakagawa and Sakata were the first to introduce flavor changing neutrino oscillations[16]. They express the weak flavor eigenstates of the neutrino $\left(\nu_e, \nu_\mu, \nu_\tau\right)$ as linear superpositions of orthogonal neutrino mass eigenstates (ν_1, ν_2, ν_3)[7]:

$$\begin{pmatrix} \nu_e \\ \nu_\mu \\ \nu_\tau \end{pmatrix} = U \begin{pmatrix} \nu_1 \\ \nu_2 \\ \nu_3 \end{pmatrix} \tag{1.2}$$

The translation between eigenstates is accomplished by the unitary 3×3 Pontecorvo Maki Nakagawa Sakata (PMNS) matrix U. Similar to the CKM in the quark sector [17, 18] the PMNS matrix can be parameterised by three mixing angles θ_{ij} and one CP violating phase δ [7].

$$U = \begin{pmatrix} 1 & 0 & 0 \\ 0 & c_{23} & s_{23} \\ 0 & -s_{23} & c_{23} \end{pmatrix} \begin{pmatrix} c_{13} & 0 & s_{13}e^{-i\delta} \\ 0 & 1 & 0 \\ -s_{13}e^{-i\delta} & 0 & c_{13} \end{pmatrix} \begin{pmatrix} c_{12} & s_{12} & 0 \\ -s_{12} & c_{12} & 0 \\ 0 & 0 & 1 \end{pmatrix} \tag{1.3}$$

The parameters s_{ij} and c_{ij} are abbreviations for $\sin\theta_{ij}$ and $\cos\theta_{ij}$, respectively. If neutrinos are of Majorana nature, i.e. they are their own antiparticles, two additional CP-violating phases would be introduced [19]. These Majorana phases are neglected in the following, as they do not contribute the oscillation probability [7]. In the following the plane wave approach is used to illustrate neutrino oscillation. A more detailed approach using wave packet and quantum field theory is given in [20].
Neutrinos are created and detected in their flavor eigenstates, but propagate

as mass eigenstates. These states have to solve the Schrödinger equation[7], thus the temporal development is given by:

$$|\nu_i\,(t)\rangle = e^{-iE_i t}\,|\nu_i\,(0)\rangle \tag{1.4}$$

with E_i the energy of the mass eigenstate m_i and $\hbar = c = 1$.
Assuming a small finite but small rest mass for the neutrino, so that $m_i \ll p_i$ and $p_i \approx E_i$ is valid, one can approximate the neutrino Energy as:

$$E_i = \sqrt{p_i^2 + m_i^2} \simeq p_i + \frac{mi_i^2}{2p_i} \simeq E + \frac{m_i^2}{2E} \tag{1.5}$$

From formula (1.2)-(1.5) it follows that the probability to detect a neutrino in the flavour eigenstate β which is produced in the flavor eigenstate α flavoured one is:

$$P_{\alpha\to\beta} = |\left\langle \nu_\beta \,\middle|\, \nu_\alpha(t)\right\rangle|^2 \tag{1.6}$$

with$|\nu_\alpha(t)\rangle = \sum_{i=1}^{3} U_{\alpha i}\,|\nu_i(t)\rangle$. Thus the oscillation probability may be expressed as:

$$P_{\alpha\to\beta} = \left|\sum_{i=1}^{3} \left\langle \nu_\beta \,\middle|\, \nu_i\right\rangle e^{-i\frac{m_i^2 t}{2E}}\,\langle \nu_i \,|\, \nu_\alpha\rangle\right|^2 = \left|\sum_{i=1}^{3} U_{\alpha i}U^*_{\beta i}e^{-i\frac{m_i^2 t}{2E}}\right|^2 \tag{1.7}$$

On the other the so called survival probability to detect a neutrino which was produced in the flavor eigenstate α again in the same flavor eigenstate α is given by:

$$P_{\alpha\to\alpha} = \left|\sum_{i=1}^{3} U_{\alpha i}U^*_{\alpha i}e^{-i\frac{m_i^2 t}{2E}}\right|^2 = \left|\sum_{i=1}^{3} |U_{\alpha i}|^2\, e^{-i\frac{m_i^2 t}{2E}}\right|^2 \tag{1.8}$$

For antineutrinos, U has to be replaced by U^* in equation (1.7) and 1.8 [21]. Up to now the ultrarelativistic condition is valid for all neutrinos, which implies that for the distance L the neutrino has travelled since its creation L $\sim$t can be assumed. Thus equation 1.7 and 1.8 become:

$$P_{\alpha\to\beta} = \left|\sum_{i=1}^{3} U_{\alpha i}U^*_{\beta i}e^{-2i\Delta_{pi}}\right|^2 \tag{1.9}$$

and

$$P_{\alpha\to\alpha} = \left|\sum_{i=1}^{3} |U_{\alpha i}|^2\, e^{-2i\Delta_{pi}}\right|^2 \tag{1.10}$$

Parameter	Value
Δm^2_{12}	$7.37^{+0.6}_{-0.44} \cdot 10^{-5}\mathrm{eV}^2$
$\lvert\Delta m^2\rvert$	$\pm\,(2.50 \pm 0.13) \cdot 10^{-3}\mathrm{eV}^2$ (NH)
$\lvert\Delta m^2\rvert$	$\pm\left(2.46^{+0.14}_{-0.13}\right) \cdot 10^{-3}\mathrm{eV}^2$ (IH)
$\sin^2(\theta_{12})$	$0.297^{+0.57}_{-0.47}$
$\sin^2(\theta_{23})$	$0.437^{+0.179}_{-0.058} \pm 0.013$ (NH)
$\sin^2(\theta_{23})$	$0.569^{+0.068}_{-0.186} \pm 0.013$ (IH)
$\sin^2(\theta_{13})$	$0.0214^{+0.0032}_{-0.0029}$ (NH)
$\sin^2(\theta_{13})$	$0.0218^{+0.0030}_{-0.0032}$ (IH)
$\delta\backslash\pi$	$1.35^{+0.64}_{-0.43}$ (NH)
$\delta\backslash\pi$	$1.32^{+0.67}_{-0.49}$ (IH)

Table 1.1: Current neutrino oscillation parameters, with NH indicating normal and IH inverse hierarchy [22]

with fixed index p and:

$$\Delta_{pi} = \left(E_i - E_p\right) t \sim \frac{\Delta m^2_{pi} L}{4E} \tag{1.11}$$

where $\Delta m^2_{pi} = m^2_i - m^2_p$.
So the probability to detect a neutrino created in the flavor eigenstate α in the flavor eigenstate $\alpha\backslash\beta$ will oscillate with L/E. Thus, this phenomenon is called neutrino oscillation. The oscillation amplitude is given by the mixing angles and the CP violating phase δ, while the frequency is proportional to Δm_{ij}. Thus the observation of neutrino indicates that $\Delta|m_{ij}| > 0$ for at least one pair (i,j), meaning that at least one neutrino masseigenstate differs from zero. Furthermore, U is not diagonal, i.e. the mixing angles have non zero values.
Given that $\sin^2(2\theta_{13})$ is very small and $\Delta m^2_{13} \gg \Delta m^2_{12}$ (see table 1.1), it is often justified to just consider oscillations between two neutrinos. With this approach the oscillation probability (1.7) changes to:

$$P_{\alpha\to\beta} = \sin^2(2\theta)\sin^2\left(\frac{m_2^2 - m_1^2}{4E} L\right) \tag{1.12}$$

Up to now, the mixing angles θ_{ij} and the mass differences Δ^2_{12} and $|\Delta m_{23}|^2$ have been measured. Best fit parameters with three σ range, obtained via a global analysis are given in table 1.1 [22]. The sign of Δ^2_{12} is given by solar neutrino experiments [23, 24] (see section 1.3), while the sign of Δm^2_{23}

is still unknown. Therefore, two different orderings of the neutrino mass eigenstates are possible, the normal $m_3 > m_2 > m_1$ (NH) and inverted hierachy $m_2 > m_1 > m_3$ (IH). Hence, $\Delta m = m_3^2 - \left(m_2^1 + m_1^2\right)/2$ is use in table 1.1. With this value being positive for the NH and negative for IH [7].

1.3 Oscillations in Matter

In Normal matter matter neutrinos may scatter coherently on electrons and nucleons. Neutrinos with all flavors can interact via neutral current interactions (NC). On the other hand, for neutrino energies below the rest mass of muons and tauons, only electron neutrinos may scatter via charged current (CC) reactions. Figure 1.1 depicts the Feynman graphs for this interaction. It shows that every flavor can couple vi athe Z^0 boson, while only the electron neutrinos couple via the $W^{\pm}$ bosons.

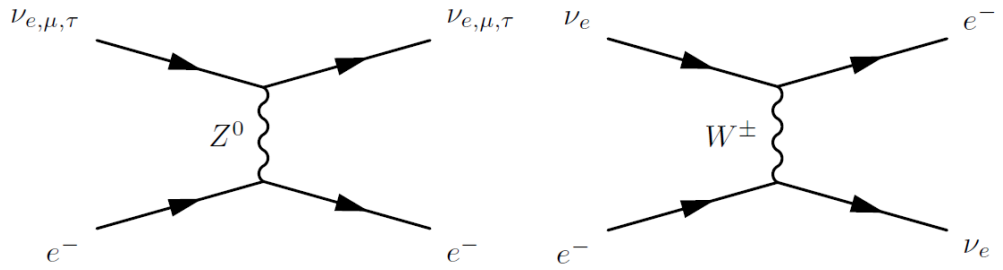

Figure 1.1: First order Feynman diagrams for neutrino-electron scattering. *Left*: Neutral current reaction through Z^0 exchange, possible for all neutrino flavours. *Right*: Charged-current reaction through $W^{\pm}$ exchange. For solar neutrinos only electron neutrinos can interact in this way.

Hence, the electron neutrino cross section is larger compared to the other flavors. This enlarged cross section creates an additional potential

$$V = \sqrt{2} G_F N_e(\vec{x}) \tag{1.13}$$

with the Fermi constant G_f and the electron density $N_e(\vec{x})$. One can interpret this potential as an additional mass term in the Hamiltonian describing the propagation of the neutrino mass eigenstates. As the third matter eigenstate ν_{3m} effectively decouples from the first two mass eigenstates and is not affected my solar nor earth matter ($\nu_{3m} \approx \nu_3$), the electron neutrino survival probability may be approximates by the following term [25]:

$$P_{ee} = c_{13}^4 P_{2f}\left(\theta_{12}, \Delta m_{12}^2, c_{13}^2 V\right) + s_{13}^2 \tag{1.14}$$

where P_{ee} is the electron neutrino survival probability in the two flavor approximation and an effective potential $c_{13}^2 V$.
The two flavor mixing angle in matter is [26]:

$$\cos(2\theta_{12,m}) = \frac{\cos(2\theta_{12}) - 2EV/\Delta m_{12}^2}{\sqrt{\left(\cos(2\theta_{12}) - 2EV/\Delta m_{12}^2\right)^2 + \sin(2\theta_{12})}} \tag{1.15}$$

with the neutrino energy E, the vacuum mixing angle θ_{12} and the vacuum mass difference Δm_{12}. Three special cases can be derived from this eqation:

- $2EV/\Delta m_{12}^2 \ll \cos 2\theta_{12} \Rightarrow \cos 2\theta_{12,m} \approx \cos 2\theta_{12}$: the mixing angle is almost not affected by the matter (vacuum region)
- $2EV/\Delta m_{12}^2 \approx \cos 2\theta_{12} \Rightarrow \theta_{12,m} \approx 45°$ the mixing between the neutrino flavors is maximal, independent of the value of θ_{12}
- $2EV/\Delta m_{12}^2 \gg \cos 2\theta_{12} \Rightarrow \theta_{12,m} \approx 90°$ almost no mixing and $\nu_e \approx \nu_{2,m}$,i.e. an electron neutrino mainly consists of the matter eigenstate $\nu_{2,m}$

The last point is valid for solar neutrinos, that are produced in the solar core for energies above $\sim 10\,\mathrm{MeV}$. As presented in section 1.4 these neutrinos are created as electron neutrinos. Hence, they almost consist purely of the mass eigenstate $\nu_{2,m}$. When these neutrinos propagate through the sun the electron density will decrease towards the solar boarder, thus the mixing angle $\theta_{12,m}$ changes, too. Due to the small gradient of electron density in the sun, it can be assumed as constant over several oscillation length $L_m = L\frac{\sin(2\theta_{12})}{\sin(2\theta_{12,m})}$. Hence, at a resonance point an adiabatic conversion appears leaving the neutrinos in the mass eigenstate $\nu_{2,m}$. This resonant conversion is called the Mikheev-Smirnov-Wolfenstein (MSW) effect [27]. The implications of the effect and a path of neutrino through the sun are depicted in figure 1.2. Since the probability for a non adiabatic transition between $\nu_{2,m}$ and $\nu_{1,m}$ is $P_c = 10^{-9} - 10^{-7}\left(\frac{E}{MeV}\right)^2$ [26] it will be neglected in the following evaluation . When the neutrino leaves the sun the normal PMNS matrix applies, however the neutrinos are in the mass eigenstate $\nu_{2,m}$ and thus, do not oscillate on their travel to earth. When the neutrino traverses the earth a transition $\nu_{2,m} \to \nu_{1,m}$, the so called earth-matter-effect, is possible. However, this only changes the probability P_{ee} by 1-2% and will be neglected in the following [25]. So the probability to detect a electron neutrino produced as ν_e is:

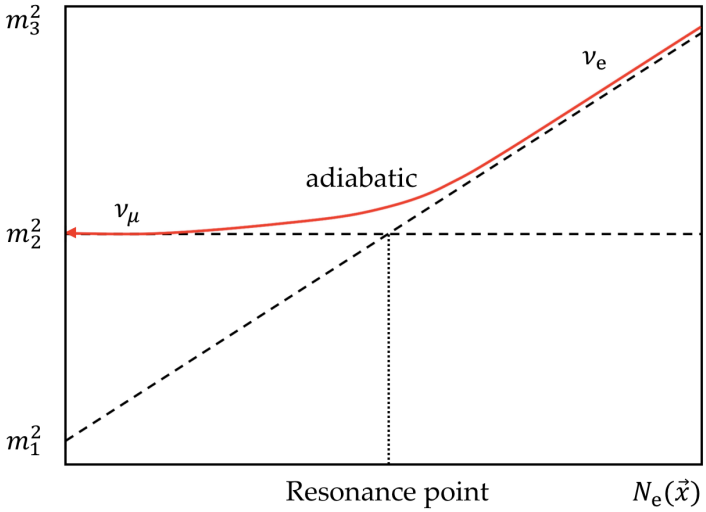

Figure 1.2: Sketch of the MSW effect. The electron density on the right represents the solar core. Neutrinos created in the core, travel to the left towards the vacuum while the electron density decreases. Due to the adiabatic conversion a ν_e leaves the sun in the mass eigenstate ν_2. In the vacuum this becomes a ν_μ [29]

$$P_{ee} = \left|\langle \nu_{2,m} | \nu_e \rangle\right|^2 \approx \sin^2(2\theta_{12})) \approx 30\% \tag{1.16}$$

Averaging over all possible production points of neutrinos, the two flavor survival probability is given by.

$$P_{2f} = \frac{1}{2}\left[1 + \cos 2\theta_{12} \langle \cos 2\theta_{12,m} \rangle\right] \tag{1.17}$$

with $\langle \cos 2\theta_{12,m} \rangle$ being the value of $\cos 2\theta_{12,m}$ averaged over all production points, calculated by:

$$\langle \cos 2\theta_{12,m} \rangle = \int_0^{R_\odot} dr\, f(r) \cos 2\theta_{12} \tag{1.18}$$

Here, $R_\odot$ is the Radius of the sun and f(r) the normalized distribution function of neutrino sources[28]. Equation 1.15 shows that the mixing angle θ_{12} is energy dependant, therefore also the survivial probability P_{ee} is energy dependant.
Figure 1.2 shows the survival probability for solar neutrinos as predicted by the MSW-large mixing angle (MSW-LMA) solution, combined with measurements from the Borexino experiment for different solar neutrinons [30]. The LMA solution is confirmed by the KamLAND [5] and Borexino experiment

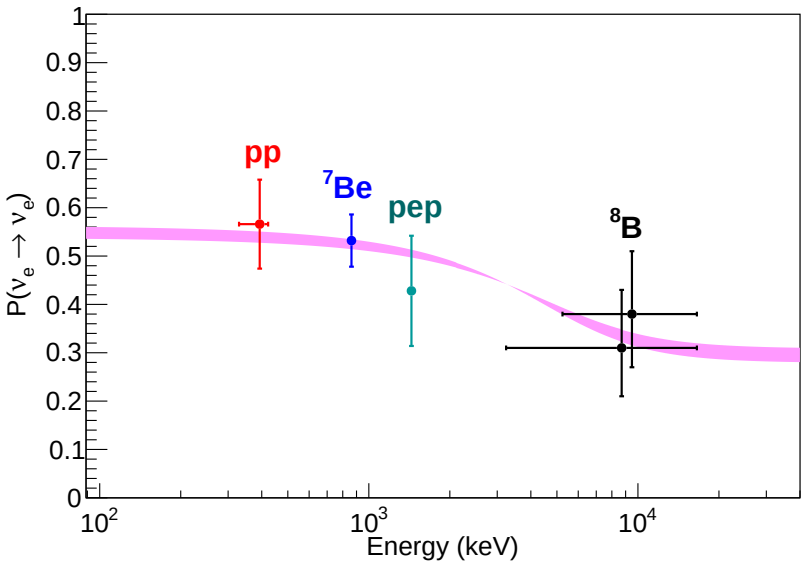

Figure 1.3: The energy dependant survival probability for solar ν_e. The grey band depicts the 1σ range for the predicted survival probability by the MSW-LMA solution. The latest Borexino measurements of ^{7}Be, pep, and pp neutrinos[30] plus the ^{8}B measurement [31] are all in agreement with the prediction.

[32]. Three different regimes may be distinguished. The low energetic pp,^{7}Be and pep neutrinos (see section 1.4) are vacuum dominated, while the high energy part of the ^{8}B neutrinos are matter dominated. In between, at around 2-5 MeV lies the transition regime.
So far all measurements have been performed in the vacuum or matter regime, while the transition region has only slightly been touched. However a measurement in this regime is crucial, as physics that affects the interaction of neutrinos with matter would be visible in the oscillation probability in this region. For example, in a simple extension of the standard model the fermi constant G_f can be exchanged by $A_{MSW}G_f$, with A_{MSW}=1 being the standard model case. For $A_{MSW} < 1$ the matter effect is weakened, while $A_{MSW} > 1$ enhances it. Therefore, the survival probability in the transition region is either reduced or enhanced, respectively. Current solar neutrino data constrains it to:

$$A_{MSW} = 1.47^{-0.42}_{+0.54}, \tag{1.19}$$

which is consistent with the SM.

1.4 Solar Neutrinos

The sun generates its energy by fusion of hydrogen to helium. The net reaction is:

$$4\mathrm{p} \rightarrow^{4} \mathrm{He} + 2\mathrm{e}^{+} + 2\nu_{\mathrm{e}} \tag{1.20}$$

An energy of Q=26.7 MeV is released during this reaction. There are two fusion chains that fuse hydrogen to helium. The pp-chain [33] , being the dominant one in the sun, is depicted in figure 1.4. Here hydrogen is, over several steps directly fused to helium. The neutrinos are named after the reaction in which they are created. The pp-chain produces pp, ^{7}Be, pep, ^{8}B and hep neutrinos. The corresponding neutrinos are marked red in figure 1.4. As pp, ^{8}B and hep neutrinos are produced via a three body decay, they have a continuous spectrum. Contrary the pep and ^{7}Be neutrinos are produced in two body decays and are monoenergetic.
The subdominant chain is the so-called CNO cycle [34]. Due to the higher coulomb barrier of its involved nuclei, it is more sensitive to the star's core temperature than the pp chain. Hence, it also depends more on the metallicity of the star, with metals being elements heavier than helium. Therefore, in heavier stars it is the main source of energy production, while in the sun it contributes $\simeq 1,5\%$ to the energy production. The cycle is depicted in figure 1.5. Carbon, nitrogen and oxygen act as catalysers for this reaction. The ^{13}N, ^{15}O and ^{17}F neutrinos (marked red in figure 1.5) all have continuous spectra.
The total solar neutrino spectrum as predicted by the Standard Solar Model (SSM) is presented in figure 1.6.
As the pp reaction is the first the one in the pp chain and the theoretical branching of the pp and pep branch is well understood, the pp luminosity is directly correlated to the solar luminosity. Hence, it is very well known. Therefore also the theoretical errors on the pep flux are very small. Since for the cross section of the other fusion reactions and the element abundances the uncertainties are rather large, the neutrino fluxes can not be calculated as precisely [35]. For ^{7}Be neutrinos there are two lines, since in 10% the ^{7}Be nucleus decays to an excited state of ^{7}Li.
There are two opposing measurements for the solar metallicity. One favors a low metallicity (AGS)[36], the other a high metallicity (GS) [37] standard solar model. The ^{7}Be, ^{8}B and CNO neutrino flux is strongly correlated to the metallicity. However, so far the theoretical uncertainties for the ^{7}Be and ^{8}B fluxes are too high to distinguish between the models. However, for CNO neutrinos the theoretical uncertainties are small enough that a future

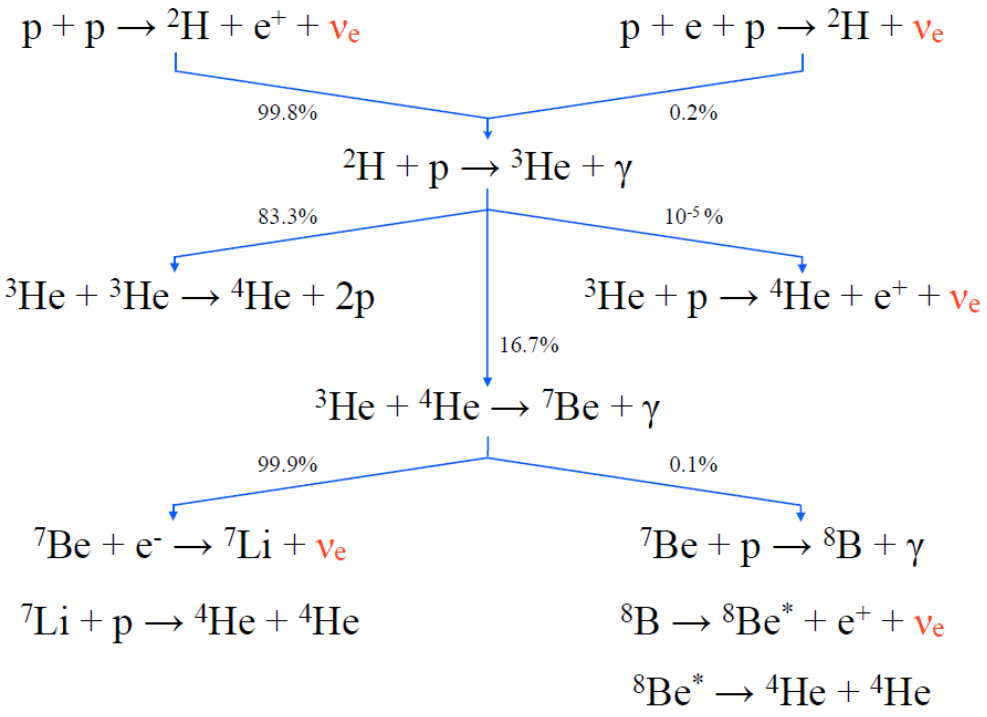

Figure 1.4: The pp chain [33]. There are five neutrino generating reactions. Neutrinos are marked red. Due to the kinematics of the reaction the pp, ^{8}B and have neutrinos have a continuous spectrum, while the ^{7}Be and pep neutrinos are monoergetic.

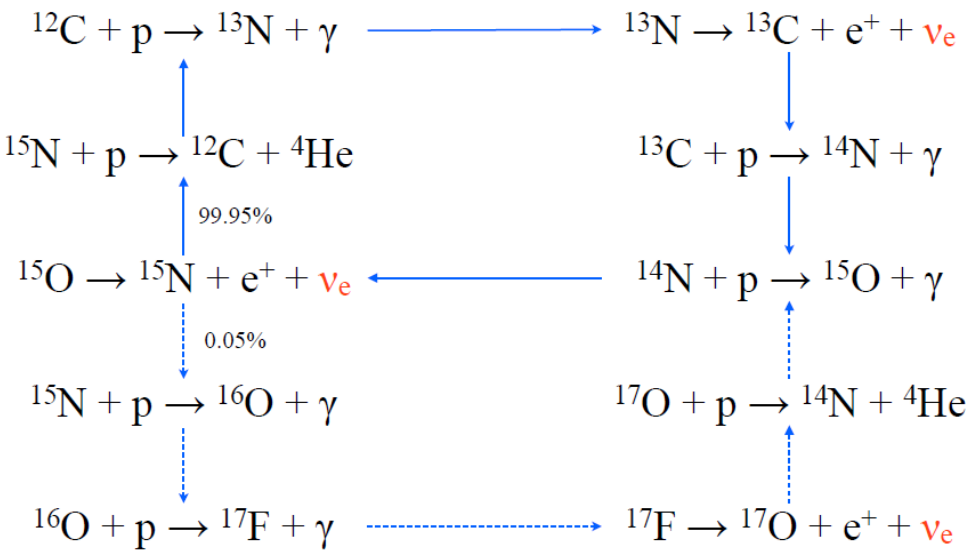

Figure 1.5: The CNO cycle [34]. The three neutrinos from ^{13}N, ^{15}O and ^{17}F have due to the kinematics of the reaction continuous energy spectra and are marked in red.

measurement could solve this issue.

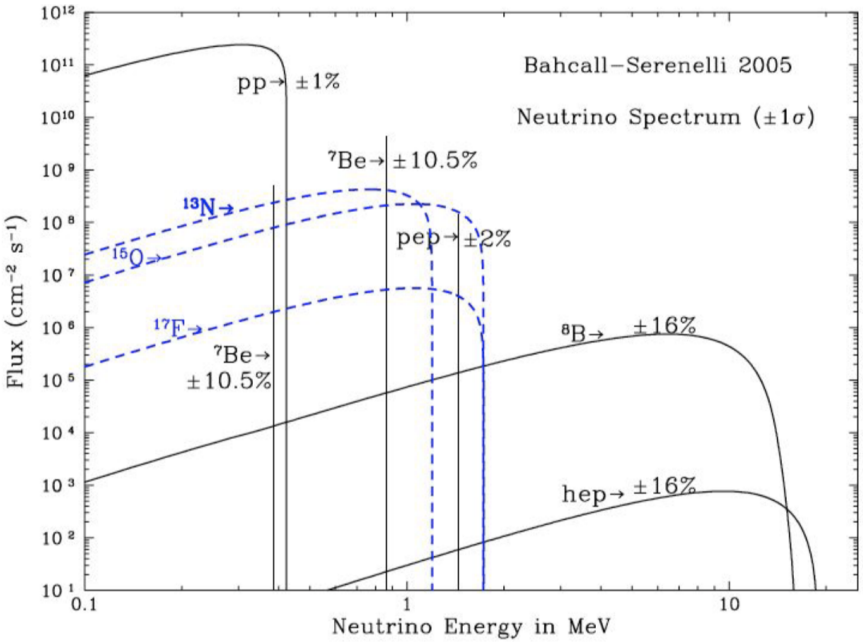

Figure 1.6: The solar neutrino spectrum calculated according to the SSM [28] . Neutrinos generated by the pp-chain are shown in solid black lines, the ones from the CNO-chain in blue dashed lines.

1.5 Supernova Neutrinos

Stars with masses greater than eight solar masses ($M_\odot$) can create energy through fusion until their core consists mainly of iron. It then will be surrounded by an onion like structure of lighter elements. As the binding energy reaches a maximum for iron, the fusion process stops in the core. Beforehand the star was in an equilibrium of gravitation and radiation pressure. The electron's Fermi pressure in the core cannot substitute the missing radiation pressure and the star will collapse. The contraction of the core continues until nuclear densities of $\simeq 10^{14}\,\mathrm{g\,cm} - 3$ are reached. At this point repulsive nuclear forces stop the collapse and the infalling matter of the outer shells bounces off the core. An outwards moving shock wave is formed that dissipates nucleons into free nucleons. Behind the shock electron neutrinos are produced via:

$$\mathrm{e}^- + \mathrm{p} \rightarrow \mathrm{n} + \nu_\mathrm{e}. \tag{1.21}$$

These neutrinos are effectively trapped. At the so called neutrinospehre the neutrinos decouple from the matter, start to propagate in front of the shock wave and thus escape the star. This is called the neutronization burst with a duration of about 20 ms. Some part of the matter is accumulated by the core.

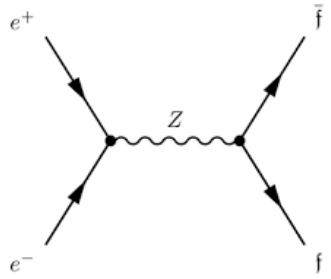

Figure 1.7: Feynmann graph of the coupling of an electron-positron-pair to a fermion-anti-fermion-pair. Via this neutrinos are thermally created during a super nova

Its gravitational energy will thereby transformed to thermal energy. This enables creation of high energetic neutrinos of all flavors through thermal processes for $\simeq 1\,\mathrm{s}$. The feynmann graph for this is shown in figure 1.7. An electron-positron-pair can via the weak interaction form a fermion-anti-fermion-pair and therefor also neutrinos.
In the end the core deloptonizes and forms a neutron star. It will be cooled by emission of thermally created neutrinos for $\simeq 10\,\mathrm{s}$ as other radiation is trapped inside. Meanwhile it is assumed that the shockwave stalls as it loses energy by photodissipation of nuclei and neutrino cooling. The density in the shockwave is still high enough that it can be reheated by the neutrinos created in the core. This ejects the outer shells and creates the optical signal. About 99% of the gravitational energy is transformed into neutrinos, resulting in $\simeq 10^{53}\,\mathrm{erg}$ emitted in the form of neutrinos. In first approximation they follow a Fermi-Dirac distribution with zero chemical potential with a mean energy of 12-18 MeV.

1.6 Reactor Neutrinos

Nuclear reactors are one of the most powerful artificial neutrino sources. The fuel's fission products are neutron rich and therefore undergo several beta decays until a stable isotope is reached. Solely anti neutrinos are produced this way with a mean energy of 3 MeV and maximal energy up to several MeV [7]. Figure 1.8 shows the reactor neutrino production using ^{235}U as example. Besides the neutrino generation steps also the breeding of Uranium and Plutonium is visible.
Every fission produces in average an energy of $\mathrm{E_{fis}} = 210\,\mathrm{MeV}$ and $\langle \mathrm{N} \rangle = 6$

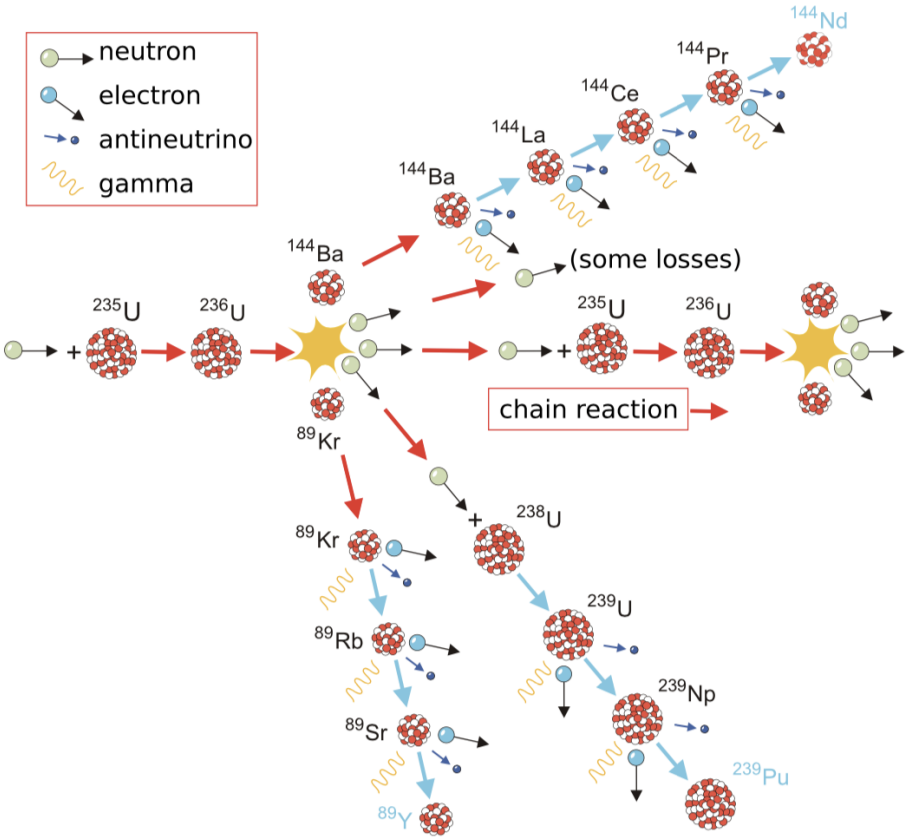

Figure 1.8: Reactor neutrino generation chain using ^{235}U as example. Neutron rich spallation products undergo several beta decays.[38]

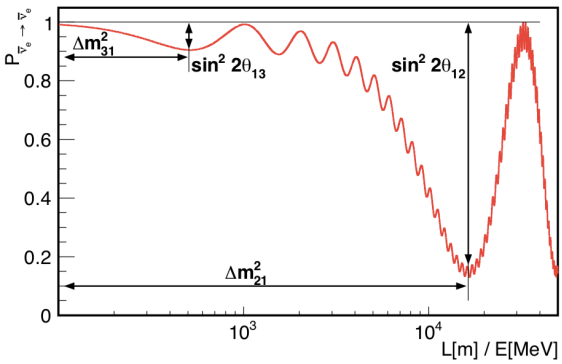

Figure 1.9: Antineutrino survival probability according to equation 1.23. The dominant parameters for the mixing are marked in the plot

anti neutrinos. Hence, the neutrino production rate $\dot{N}_\nu$ is given by:

$$\dot{N}_\nu = \dot{N}_{fis} \cdot \langle N \rangle = \frac{P_{th}}{E_{fis}} \cdot \langle N \rangle \tag{1.22}$$

with the fission rate $\dot{N}_{fis}$ and the reactors thermal power P_{th}. Modern reactors posses a thermal power of several giga watts and therefore are capable of producing more than 10^{21} neutrinos per second. Using equation 1.7 the survival probability for anti neutrinos can be written as [39]

$$\begin{aligned} P_{\bar{\nu}_e \to \bar{\nu}_e} = 1 &- \cos^4\theta_{13}\sin^2 2\theta_{12}\sin^2\Delta_{21} \\ &- \sin^2 2\theta_{13}\left(\cos^2\theta_{12}\sin^2\Delta_{31} + \sin^2\theta_{12}\sin^2\Delta_{32}\right) \end{aligned} \tag{1.23}$$

with $\Delta_{ij} = \frac{\Delta m^2_{ij} L}{4E}$. Figure 1.9 depicts the survival probability of anti neutrinos for an energy of 3 MeV. The first and second minima are given by Δm^2_{31} and Δm^2_{21}, respectively. The amplitude by the sine square of two times the respective mixing angle.
Using $\Delta m^2_{21} \ll \Delta m^2_{31}$ and $\Delta m^2_{31} \approx \Delta m^2_{32}$ one can approximate for the second minimum:

$$P_{\bar{\nu}_e \to \bar{\nu}_e} \approx 1 - \sin^2 2\theta_{13}\left(\frac{\Delta m^2_{31} L}{4E}\right) \tag{1.24}$$

This enables a measurement of θ_{13} with a known Δm^2_{31}.
There are three recent experiments that are using this fact with far detectors at the second minimum and near detectors closer to the reactors ($\lesssim$400 m) to

reduce systematics caused by the uncertainties in the reactor spectrum. The experiments are: Double Chooz [40], Reno [41] and Daya Bay [42]. All three experiments show an excess above the expected neutrino rate in the energy region of $\sim 4-6\,\mathrm{MeV}$. The origin of the excess is still unknown. A possible explanation can be the still limited knowledge of the reactor spectrum. Future high precision reactor neutrino experiments, like Junos near detector Tao [43] will increase the knowledge of the reactor neutrino spectrum and thus maybe explain the origin of the excess.

1.7 Sterile Neutrinos

Sterile neutrinos are theoretical right handed neutrinos that carry no weak charge. Hence, they are not participating in the weak interaction. However, if their restmass in nonzero they can couple via oscillations to the active neutrinos cite [44]. There no no theoretical boundaries for the number and mass of sterile neutrinos [44] There are several that introduce sterile neutrinos that would solve different problems in physics, like the smallness of neutrino masses [45, 46], the matter-antimatter assymmetrie in the universe[47] and dark matter [48]. The simplest model is the so called (3+1) model that introduces one sterile neutrino with a mass eigenstate ν_4. It extends the PMNS matrix to a 4x4 matrix:

$$\begin{pmatrix} \nu_\mathrm{e} \\ \nu_\mu \\ \nu_\tau \\ \nu_\mathrm{s} \end{pmatrix} = \begin{pmatrix} \mathrm{U_{e1}} & \mathrm{U_{e2}} & \mathrm{U_{e3}} & \mathrm{U_{e4}} \\ \mathrm{U}_{\mu 1} & \mathrm{U}_{\mu 2} & \mathrm{U}_{\mu 3} & \mathrm{U}_{\mu 4} \\ \mathrm{U}_{\tau 1} & \mathrm{U}_{\tau 2} & \mathrm{U}_{\tau 3} & \mathrm{U}_{\tau 4} \\ \mathrm{U_{s1}} & \mathrm{U_{s2}} & \mathrm{U_{s3}} & \mathrm{U_{s4}} \end{pmatrix} \begin{pmatrix} \nu_1 \\ \nu_2 \\ \nu_3 \\ \nu_4 \end{pmatrix} \tag{1.25}$$

It ads three mixing angles, two Dirac CP-violating phases and one Majorana CP-violating phase to the PMNS matrix. The sterile neutrino ν_s cannot interact directly. However, ν_4 affects the oscillation behaviour of the active neutrinos, as they contain an admixture of ν_4. For $\mathrm{m_4} \gg \mathrm{m_1}, \mathrm{m_2 m_3}$ the survival probability can be approximated with the two neutrino case as:

$$\mathrm{P}_{\alpha\beta} \approx \left| \delta_{\alpha\beta} - \sin^2\left(2\theta_{\alpha\beta}\right) \sin^2\left(\frac{1.27 \cdot \Delta \mathrm{m}^2_{41}[\mathrm{eV}^2] \cdot \mathrm{L[m]}}{\mathrm{E[MeV]}}\right) \right| \tag{1.26}$$

with $\sin^2\left(2\theta_{\alpha\beta}\right) = 4\left|\mathrm{U}_{\alpha 4}\right|^2 \left|\delta_{\alpha\beta} - \left|\mathrm{U}_{\beta 4}\right|^2\right|$ [44].
There are several experimental hints that point to the existence of a sterile neutrino. They will be briefly summarized in the following.

LSND and Miniboone

The Liquid Scintillator Neutrino Detector (LSND) [49] measured the $\nu_\mu \to \nu_e$ $\bar{\nu}_\mu \to \bar{\nu}_e$ oscillation using a neutrino beam in the energy range of a few tens of MeV. The detector was placed in a distance of $\sim 30\,m$ and measured an excess of$\bar{\nu}_e$ of $\sim 3.8\sigma$ above the expectation from the three neutrino case. This excess could be explained by a fourth neutrino. The purpose of MiniBooNe [50] was to test this results. It uses the same oscillation but at higher energies E$\sim$GeV and baseline L$\sim$540m m. However L/E is the same as for LSND. MiniBooNe found an excess of 4.7σ with the neutrino and antineutrino data, which is also compatible with LSND. The two experiments combined reach a significance of 6.0σ. However, the excess manifest just at the lower energy threshold and is not fully compatible with the (3+1)model [44].

Reactor Neutrino Anomaly

The neutrino rate observed by reactor experiments used to be consistent with the expectations. A recalculation of the reactor flux created the reactor neutrino anomaly[51]. The latest calculation show an increase in the expected reactor neutrino rate of 5% [52], which manifests in a deficit in the measured neutrino rate. The average ratio of measured and expected rate is $R = 0.933 \pm 0.021$ giving a significance of $\sim 3.1\sigma$ [44]. A sterile neutrino with $\Delta m^2_{41} \gtrsim 0.5 eV^2$ could explain the anomaly.

Gallium Anomaly

The radiochemical solar neutrino experiments GALLEX[53] and SAGE[54] used strong ^{37}Ar and ^{51}Cr sources for calibrating the detectors. Both elements decay via electron capture and an endpoint of $\sim 800\,keV$. The neutrinos are detected via the charged current reaction $\nu_e + {}^{71}Ga \to e^- + {}^{71}Ge$. The sources were placed very close to the detector with a baseline of $\sim 1\,m$. Both experiments detected less neutrino than predicted with an average ratio of $R = 0.84 \pm 0.05$, corresponding to a 2.9σ deficit [44].A sterile neutrino with $\Delta m^2_{41} \gtrsim 1 eV^2$ could explain the measurements.

1.8 Real Time Neutrino Detectors

The first detection of solar neutrinos was done by radio chemical experiments. In started in the 1970s with the Homestake[55] experiment by Raymond Davies and continued with GALLEX [53], SAGE[54] and GNO [56]. They are all based on the reaction:

$$\nu_{\mathrm{e}} + {}^{37}\mathrm{Cl} \rightarrow {}^{37}\mathrm{Ar} + \mathrm{e}^{-} \tag{1.27}$$

Hence, these experiments are only sensitive to electron neutrinos. The unstable ^{37}Ar is extracted and a decay rate is measured. As the reaction's energy threshold is below the pp neutrino endpoint, it is possible to measure the full neutrino spectrum. However these experiments just provide an integrated rate above threshold. An lower rate than expected was measured and the so called solar neutrino problem was created.
On the other side Water-Čerenkov (WCD) and Liquid Scintillator detectors (LSD) measure the energy of a neutrino in real-time. WCDs can reconstruct the direction of an interaction, but due to the low light are just sensitive to the solar ^{8}B neutrinos [24]. The higher light yield in LSDs enables a lower threshold, so that a measurement down to pp neutrinos is possible[30]. In the following the Super Kamiokande detector will be described as an example for WCDs and JUNO for LSDs.

1.8.1 Super Kamiokande

Super-Kamiokande is a Water-Čerenkov detector with 50 kt active volume and 22.5 fiducial volume for the most analyses [57]. It is located in the Kamioka Observatory that is covered by 1000 m of rock which corresponds to 2700 m.w.e (meter water equivalent).
Solar neutrinos are detected via elastic neutrino electron scattering:

$$\nu_{\mathrm{x}} + \mathrm{e}^{-} \rightarrow \nu_{\mathrm{x}} + \mathrm{e}^{-} \tag{1.28}$$

For neutrino energies below the rest mass of muons, the cross section for electron neutrinos is roughly six times higher than for muon and tauon neutrinos, as they can interact both via CC and NC reactions. The scattered neutrino leaves the detector whilst the electron is detected via the Čerenkov effect [58].
If a charged particle travels faster through a medium than the phase velocity it emits so called Čerenkov light. The particle polarises the medium's atoms, which then emit light. If the particle exceeds the phase velocity, this light interferes constructively. This radiation forms a conical light front along the

track. A sketch of a track is given in figure 1.10. The opening angle α is given by the material's refractive index n and the particle's velocity $\beta = \frac{\mathrm{v}}{\mathrm{c}}$:

$$\cos\alpha = \frac{1}{\beta \mathrm{n}} \tag{1.29}$$

For the ultra relativistic case $\beta \simeq 1$ the angle reaches a maximum of $\alpha_{\max} = \mathrm{acos}\left(\frac{1}{\mathrm{n}}\right)$.
As the velocity must be at least $\beta \geq \frac{1}{\mathrm{n}}$ the threshold energy is given by:

$$\mathrm{E}_{\mathrm{threshold}} = \frac{1}{\sqrt{1 - \frac{1}{\mathrm{n}^2}}} \tag{1.30}$$

For electrons in water with $\mathrm{n_w} \simeq 1.33$ the threshold energy is $\mathrm{E}_{\mathrm{threshold}} \simeq 800\,\mathrm{keV}$ and the maximal angle $\alpha_{\max} = 41.4°$. The light yield in water is roughly 200 photons per MeV[59]. To detect the Čerenkov radiation Super-Kamiokande is equipped with 11000 20" photo multiplier tubes (PMTs). This corresponds to a 40% optical coverage. Together with improved water-circulation, front end electronics and calibration techniques the experiment obtains an energy threshold of 3.49 MeV [60]. Hence, Super Kamiokande is not sensitive for pp, cno, pep and ^{7}Be neutrinos. However the ^{8}B neutrino flux is determined to be:

$$\phi_{^8\mathrm{B}} = \left(2.308 \pm 0.020 \pm^{+0.039}_{-0.040}\right) \cdot 10^6 \left(\mathrm{cm}^2\mathrm{s}\right) \tag{1.31}$$

with a lifetime of 1664 and $31,918^{+283}_{-281}(\mathrm{stat.}) \pm 543(\mathrm{syst})$ events in an energy range from 3.49 MeV to 19.5 MeV. The SSM predicts more then double the rate. So this is a clear hint that electron neutrinos oscillate to muon and tauon neutrinos, as these have a lower cross section for elastic scattering. The extracted spectrum is compatible with the MSW-LMA solution as well with a flat neutrino survival probability. A üpturnïs slightly favored by fit, by about $1\,\sigma$. However the parameters given by the MSW-LMA solution are slightly disfavored, by about $1.5\,\sigma$

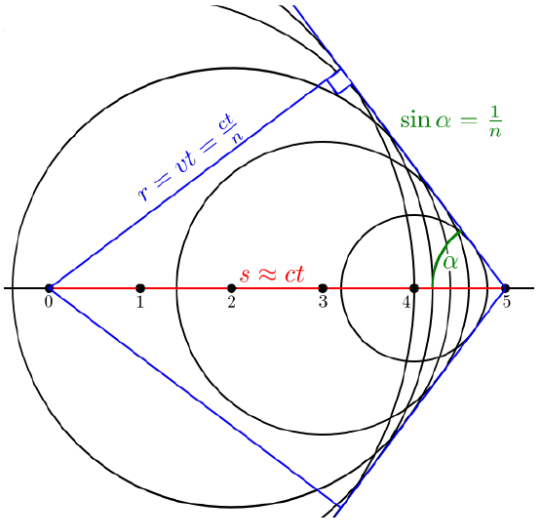

Figure 1.10: Sketch of Čerenkov light emission by a charged relativistic particle travelling through a medium with refractive index n¿1. The particle emits spherical light waves along its track. A light cone forms through constructive interference. The opening angle is given by the material and the particles velocity. [61]

Chapter 2

Borexino

The Borexino detector was proposed in 1986 [62] to perform a real time solar neutrino measurement in the sub MeV regime. In its predecessor the Counting Test Facility (CTF) [63] it was shown that the necessary purities to measure the rare neutrino interactions are reachable with the liquid scintillator technique.
Construction of the main detector started in 1996 at the Laboratori Nationali del Gran Sasso (LNGS). Data taking started in 2007 and is still ongoing at the time of writing. The main goal of a ^{7}Be neutrino measurement [64] could be achieved only a few months after the start of data taking. In the following years all neutrinos of the pp chain, besides the hep neutrinos, could be detected [11, 12, 31]. For the CNO chain the world leading limit was achieved [32].
In section 2.1 a description of the detector design of Borexino is given and in section 2.2 a summary of the physics program is given.

2.1 Detector Design

The Borexino detector is located in Hall C in the LNGS, which is an underground laboratory below the Gran Sasso mountain massive in Abruzzo, Italy. It is reachable via a highway tunnel. The laboratory is at a depth that corresponds to 3800 m we. The Borexino detector consists of two subdetecotors, namely the Inner Detector (ID) and the Outer Detector(OD). They are optically separated by the Stainless Steel Sphere (SSS) and filled with liquid scintillator and ultra pure water, respectively. A scheme of the setup is given in figure 2.1. in the next two sections a description of the subdectors is given.

2.1.1 Inner Detector

At the center of the ID there is ∼280 t of active volume. It consists of ultra pure liquid scintillator with a density of $\rho = 0.88\,\mathrm{t/m^3}$. The base of the scintillator is pseudocomene (PC, 1,2,4-trimethylbenzene $C_6H_3\,(CH_3)_3$), which is doped with the wavelength shifter PPO(2,5-diphenyloxazole, $C_{13}h_{11}NO$) at a concentration of 1.5 g/l. Charged particles excite the PC molecules ,which afterwards transfer their excitation energy to PPO. Eventually, PPO emits photons with a fluorescence time of $\simeq 3$ ns and a peak wavelength of $\simeq 360$ nm. A detailed description of this process is given in [65]. The mixture grants a high light yield of $\simeq 10^4$ photons per MeV deposited energy and a attenuation length of $\simeq 8$ m at the peak wave length.
The achieve the required radiopurity levels the scintillator was cleaned onsite before filling it into the detector. Contaminants from dust (^{238}U, ^{232}Th, ^{40}K), from air (^{39}Ar, ^{85}Kr) and cosmogenically produced ^{7}Be were removed. Thus, the design goal for Uranium/Thorium contamination of ¡10^{-16}g/g could be surpassed with values of $(5.3 \pm 0.5) \cdot 10^{-18}$g/g and $(3.8 \pm 0.8) \cdot 10^{-18}$g/g, respectively. After purification campaigns in 2010 and 2011 the levels could be reduced even further to $< 9.4 \cdot 10^{-20}$g/g of ^{238}U and $< 5.7 \cdot 10^{-19}$g/g for ^{232}Th [30].
The active volume is contained in a 125 μm thin nylon membrane with a radius of 4.25 m, the so called Inner Vessel (IV). To preserve the detector's radiopurity it was constructed off site under clean room conditions. The IV is hold in place by nylon strings to counteract small buoyancy forces, caused by small density differences of the buffer and the active volume. As nylon is transparent and carries a similar refractive index as PC, the IV does not affect the optical properties of the detector. Besides centring the active volume, the IV also serves as a ^{222}Rn barrier, which is emanated by the SSS.
The IV is surrounded by 1024 t of buffer liquid consisting of PC and DMP (dimethylphytalate) at concentration of 5 g/l. In 2009 a small leak in the IV was discovered. To adjust the densities of the buffer and scintillator and thus hindering the scintillator from flowing out of the IV, the DMP concentration was changed to 2 g/l [66]. The main purpose of the buffer is to shield the fiducial volume from external gammas and fast neutrons. The DMP quenches the yield in this region by a factor of ≃20, and thus strongly suppresses signals in the buffer. The buffer region is further divided by the Outer Vessel with a radius of 5.5 m. It is made of the same material as the IV with the same optical properties. It serves as an extra barrier against radon diffusion from the pmt and SSS to the active volume. The SSS with a radius of 6.82 marks the border between the ID and OD. It separates the two in terms of light propagation, creating two subdetectors for muon identification. 2212

PMT inward facing 8" ETL 9351 PMTs are mounted on the SSS. To increase the optical coverage to 30% 1812 of these are equipped with aluminium light concentrators. These Winston cones are focused on the IV, therefore 384 PMTs do not posses cones to grant them a larger field of view. This allows the study of the buffer region and the backgrounds originating there.

2.1.2 Outer Detector

The OD consists of a steel dome of 16.9 m height and a diameter of 16.9 m. It is filled with 2.4 kt deionised water. It serves as a passive shielding against external gammas and fast neutrons, created by muons in the surrounding rock. Furthermore it is an active muon veto. Muons crossing the OD will create Čerenkov light, which is detected by 208 PMTs. It is the same model as in the ID, however these are equipped with an encapsulation to withstand the pressure. 154 are mounted in eight circles in the upper three quarters of the detector, while the remaining 54 are mounted in five concentric rings on the water tank's floor. Monte simulations identified this distribution to be the most effective one for muon identification. To increase the light yield the walls are covered with highly reflective tyvek foil. Furthermore the material is used create two subregions in the OD, with the border at the equator. However the separation is not perfect, just two thirds of the light path is covered. While the tyvek increases the muon detection efficiency, it disturbs the Čerenkov cones and thus the muon tracking[59].
It is assumed that the IV is contaminated with ^{210}Pb, that decays with a half life of 22.3 a to $^(210)$Po. Convection will transport this $^(210)$Po to the detector center. In 2015 detector was wrapped in a double layer of mineral wool with 20 thickness and a reflective aluminium cover to stabilise its temperature. Additionally, to create a stable positive temperature gradient from the bottom to the top, an active temperature control system was installed. The system consists of independent water loops on the outside of the water tank. The temperature development is closely monitored by several sensors in and on the detector [67].

2.2 Physics Programm

Borexino is mainly designed for a measurement of the ^{7}Be solar neutrino flux. The world leading radiopurity and an energy resolution that surpassed the design goal enable a broader physics program. Borexino performed the first real time measurement of the ^{7}Be solar neutrino flux [64] and even surpassed it by a precision measurement of this flux [68]. Also a ^{8}B neutrino

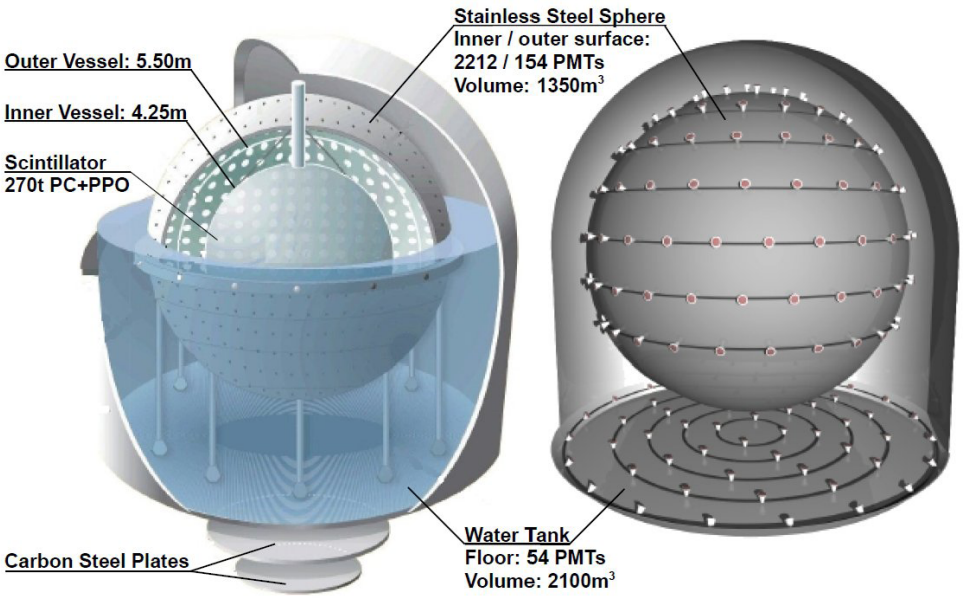

Figure 2.1: Sketch of the Borexino detector. *Left*: Cross section of the water tank and the Stainless Steel Sphere. The 2212 photomultiplier, that collect the light created by in scintillator are represented by the white dots. The innermost sphere depicts the inner vessel which encloses the sensitive volume of $\simeq 300\,\mathrm{t}$. *Right* The distribution of the photomultiplier in Outer Detector is shown. Of the 208 pmts 154 are mounted on the sphere and 54 on the dome's floor. The outer detector is filled with ultrapure water and serves as muon veto.

measurement with an unmatched threshold of 3 MeV [31] and the first detection of solar pep neutrinos together with an upper limit on the CNO flux was achieved [12]. After a careful purification campaign in 2010 and 2011, to reduce intrinsic backgrounds, the second phase of the experiment started. Here, the first real time measurement of the solar pp neutrinos could be achieved [11]. Besides the solar program, Borexino was the first detector to measure geo-neutrinos at the 3 σ level and later on performed a spectroscopic measurement [69, 70, 13]. In the following the main a brief summary of the physics will be given.

2.2.1 Solar Neutrinos

^{7}Be Neutrinos

The mono energetic 862 keV ^{7}Be neutrinos create a Compton-like recoil spectrum with the Compton edge at around 660 keV. A precise measurement allows to test the Standard Solar Model (SSM) and the vacuum regime of the MSW-LMA solution, as the energy is too low to be affected by the MSW effect. The examination of a day-night-asymmetry, induced by regeneration of solar neutrinos in the terrestrial matter, allows to constrain the neutrino oscillation parameters without the usage of reactor anti neutrinos, i.e. without the assumption of CPT symmetry. In 2008 Borexino reported the first real time measurement of solar ^{7}Be solar neutrinos [64] , afterwards, in September 2011, Borexino released a precision measurement of the flux using an exposure of 178 t yr exposure. In the analysis a fit based on monte carlo simulations and a fit based on analytic description of the spectra are averaged. In both cases the ^{7}Be neutrino rate and background components ^{85}Kr, ^{210}Po, ^{210}Bi and ^{11}C are free parameters whereas the pp, pep, CNO and ^{8}B neutrino rates are fixed to the values given by the SSM. The analytical fit is shown in figure 2.2 on the left. The analysis yields an interaction rate of $\left(46 \pm 1.5(\text{stat})^{+1.5}_{-1.6}(\text{syst.})\right)\,(\text{d100t})^{-1}$. Assuming the MSW-LMA solution the corresponding ^{7}Be solar neutrino flux is:

$$\phi\left(^{7}\text{Be}\right) = (4.48 \pm 0.24) \cdot 10^{9}\text{cm}^{-2}\text{s}^{-1} \tag{2.1}$$

confirming the SSM in case that neutrinos do oscillate. Fixing the ^{7}Be flux to the SSM prediction a survival probability of $P_{ee} = 0.51 \pm 0.07$ was found. In November 2011 the absence of a day night asymmetry in the interaction of ^{7}Be neutrinos was reported [71]. The stated value for the asymmetry was:

$$A_{DN} = 2\frac{R_N - R_D}{R_N + R_D} = 0.001 \pm 0.012_{\text{stat}} \pm 0.007_{\text{syst}} \tag{2.2}$$

where R_N and R_D are the ^{7}Be interaction rate at nigh and day, respectively. This value consistent with zero excludes the LOW solar neutrino solution at 8.5σ as shown in figure 2.2 on the right.

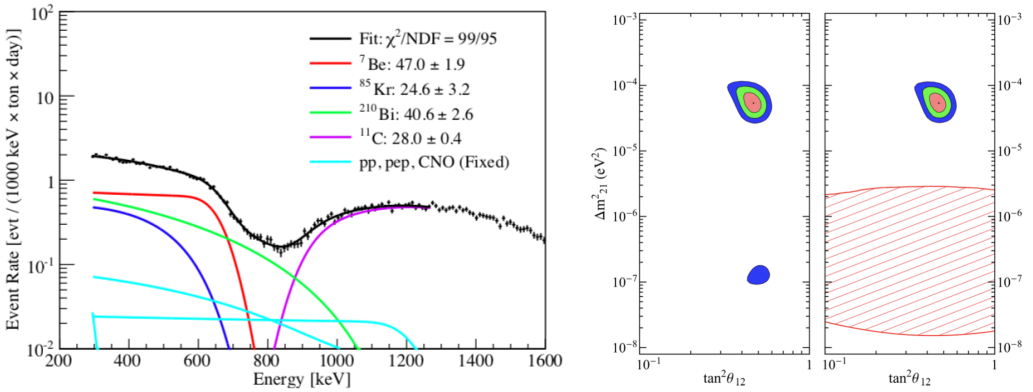

Figure 2.2: Solar ^{7}Be neutrino results. *Left*: Analytical spectral fit of the clearly visible ^{7}Be neutrino compton edge based on 178 t yr exposure. Numbers in given are in [counts/(d100 t)]. *Right*: Allowed neutrino oscillation parameter space before and after the inclusion of Borexino data. The hatched area is excluded by the Borexino ^{7}Be day-night data, excluding the LOW solution at 8.5σ.

Using data after the purification campaign between 2011 and 2015 Borexino measured an annual modulation of the ^{7}Be neutrino flux and excluded an absence at 99.99% confidence level. The best fit values of an amplitude of (7.1±1.9)%, a period of (367±10)d and a phase of (-18±24)d are consistent with a solar origin of the neutrinos.

pep and CNO neutrinos

The pep reaction is the rare alternate starting process of the pp chain. The emitted neutrinos are monoenergetic with an energy of 1.44 MeV. The ratio between the pep flux and the pp flux depends just weakly on the used model and furthermore posses a theoretical uncertainty of just about 1%.There a measurement of the pep neutrino flux is also an indirect measurement of the pp neutrino flux. As 98% of the solar energy is produced via the pp cycle, a measurement of the pep flux is directly connected to the solar luminosity. The remaining energy is created via the CNO cycle as described in section 1.4. As the CNO neutrino flux is highly dependant on the solar metallicity, a measurement could solve the solar metallicity problem. The problem consists of contradicting SSMs, where the high metallicity one GS98 predicts a 40%

higher CNO neutrino flux than the low metallicity model AGSS09 [72]. The β^+ decay of ^{11}C (τ = 29.4 min,Q=1.96 MeV) is the dominant background. It is produced via spallation processes from muons on ^{12}C. As can be seen in figure 2.3 exceeds the neutrino by an order of magnitude. However in about 95% of the cases there is also a free neutron in the final state. This allows to apply a Threefold Coincidence technique (TFC) and suppress the background by a factor of $\simeq$10 at the cost of a lifetime loss of 51.5%. Additionally a pulse shape technique to differentiate between electrons and positrons has been developed to further reduce the ^{11}C background. The effect can be seen in figure 2.3 where the blue dotted line represents ^{11}C before cuts and the black dotted line afterwards. The red line is the Compton like recoil edge at 1.22 MeV caused by the pep neutrinos.

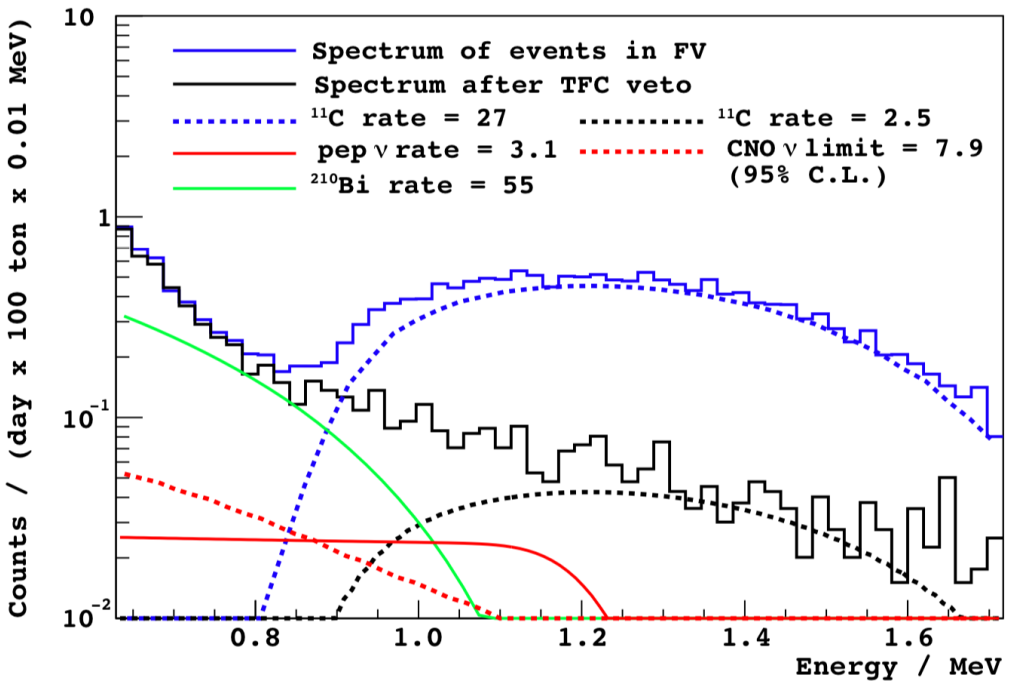

Figure 2.3: Borexino energy spectrum including fit to the signal and background components in the pep solar neutrino region. The ^{11}C spectrum before suppression is marked blue, after the Three-fold Coincidence black.

In 2012 Borexino reported an interaction rate of $(3.1\pm0.6_{\text{stat}}\pm0.3_{\text{syst}})(\text{d100t})^{-1}$ based on a multivariate fit that considers the energy and radial distribution of the events. The measurement translates to a flux of:

$$\Phi_{\text{pep}} = (1.6 \pm 0.3) \cdot 10^8 \text{cm}^{-2}\text{s}^{-1} \tag{2.3}$$

Fixing the pep flux to the one predicted by the SSM a survival probability of $P_{ee} = 0.62 \pm 0.17$ at 1.44 was found.

^{8}B neutrinos

^{8}B solar neutrinos feature a continuous spectrum that goes up to 14.6 MeV. Therefore, they cover the matter and the vacuum dominated regime of the MSW-LMA solution. Especially a measurement in the transition region between these region would be of great interest, as new physics could change the survival probability there. A precision measurement of the ^{8}B rate could help solve the solar metallicity problem as the models differ almost by 20% in the ^{8}B neutrino rate[72]. A major background arises due to spallation processes of muons on carbon that create radioactive isotopes. The short lived ones (up to $\tau \simeq 1\,\mathrm{s}$) can be suppressed by applying a veto of 6.5 s after each muon crossing the IV. If the muon produces also a neutron the TFC can be applied to veto ^{10}C with a lifetime of 27.8 s. ^{11}Be with a lifetime of 19.9 s cannot be vetoed by an event on event basis and has to be subtracted statistically. A further background is formed by 2.6 MeV gammas produced in ^{208}Tl decays. ^{208}Tl is located on the SSS and the PMTs, so a fiducial volume reduces this background. ^{208}Tl forms also an intrinsic background. It decays via beta decay with a Q=5 MeV. Its rate is measured independently via an ^{212}Bi-^{212}Po coincidence and subtracted statistically.
Based on 488 live days of data in 2010 Borexino reported a neutrino electron interaction rate of $(0.22 \pm 0.04_{\mathrm{stat}} \pm 0.01_{\mathrm{syst}})(\mathrm{d100t})^{-1}$ with a threshold of 3 MeV. Beforehand only measurements with a threshold of 3.5 and 5 MeV could be achieved[73, 74]. The interaction rate corresponds to a flux of:

$$\Phi_{^8\mathrm{B}} = (2.4 \pm 0.4_{\mathrm{stat}} \pm 0.1_{\mathrm{sys}}) \cdot 10^6 \mathrm{cm}^{-2}\mathrm{s}^{-1} \tag{2.4}$$

A convolution of the differential neutrino rate, considering energy and flavor dependant neutrino cross sections and the detector's energy response gives a survival probability of $P_{ee} = 0.29 \pm 0.10$ at a mean energy of 8.9 MeV. In 2016 Borexino released an update based on 1.5 kt x yr exposure collected between 2008 and 2016. Intrinsic backgrounds were reduced in the purification campaigns in 2010 and 2011. An independent measurement of ^{11}Be was performed that differs by 3σ from the previous result. Additionally radial information was used to disentangle intrinsic events from external ones. The analysis is split in two energy regimes. The lower one is dominated by external background and uses a stringent fiducial volume, while the high energy one uses the whole volume. Both combined give a rate of:

$$\mathrm{R_{LE+HE}} = \left(0.220^{+0.015}_{-0.016}(\mathrm{stat.})^{0.008}_{-0.008}(\mathrm{syst.})\right) \mathrm{cpd}/100\,\mathrm{t}, \tag{2.5}$$

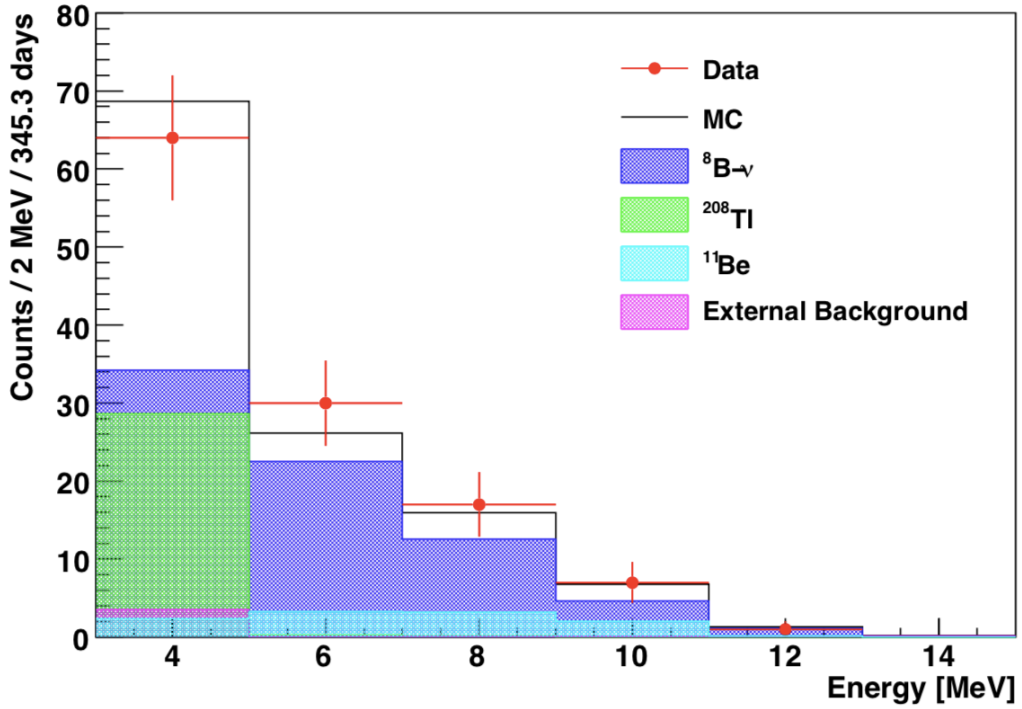

Figure 2.4: Solar ^{8}B neutrino measurement based on 488 days of exposure. Red dots marks the remaining data after all cuts. The neutrino contribution is marked in blue, intrinsic ^{208}Tl background in green, cosmogenic ^{11}Be in cyan and external background in violett.

resulting in a flux of:

$$\Phi_{\mathrm{LE+HE}} = \left(2.55^{+0.017}_{-0.019}(\mathrm{stat.})^{0.007}_{-0.007}(\mathrm{syst.})\right) \cdot 10^{6}\mathrm{cm}^{-2}\mathrm{s}^{-1}. \qquad (2.6)$$

pp neutrinos

The pp neutrinos are generated in the first fusion process of the dominant pp chain and thus are directly connected with the solar luminosity. Photons created in the core travel $\simeq 10^{5}$ years to the solar surface. So a measurement of pp neutrinos together with optical observation can prove that the sun is in thermal equilibrium for this time scale. After the intense purification campaigns in 2010 and 2011 that reduced backgrounds, especially ^{85}Kr and ^{210}Bi, Borexino was able to present the first measurement of the solar pp neutrino flux. The used data from time window from January 2012 to May 2013 is presented in figure 2.5 together with a fit including signal and contributing backgrounds [75]. ^{14}C accounts for the main part of the background. It is a β^{-} decay with a half life of 5.730 a and Q-value of 156 keV.

Neutrino species	Rate [cpd/100 t]	Flux [$cm^{-2}s^{-1}$]
pp	$1.34 \pm 10^{+6}_{-10}$	$\left(6.1 \pm 0.5^{+0.3}_{-0.5}\right) \cdot 10^{10}$
^{7}Be	$48.3 \pm ^{+0.4}_{-0.7}$	$\left(4.99 \pm 0.13^{+0.07}_{-0.1}\right) \cdot 10^{9}$
pep(HZ)	$2.43 \pm ^{+0.15}_{-0.22}$	$\left(1.27 \pm 0.19^{+0.08}_{-0.12}\right) \cdot 10^{8}$
pep(LZ)	$2.65 \pm 0.36 + 0.15_{-0.24}$	$\left(1.39 \pm 0.19^{+0.08}_{-0.13}\right) \cdot 10^{8}$
CNO	< 8.1(95%C.L.)	$< 7.9 \cdot 10^{8}$(95%C.L.)

Table 2.1: Solar neutrino rates given by the first simultaneous fit of Borexino data

The mineral oil on which the Borexino scintillator bases on was chosen on its small fraction of ^{14}C of $^{14}C/^{12}C \simeq 2.7 \cdot 10^{18}$. Nevertheless, it accounts almost for the whole trigger rate of 30 Hz of the experiment. The decay rate was determined by looking for events with two clusters in the same trigger gate, as the second one is not affected by the trigger. The ^{14}C rate is high enough that pile up events can occur. The spectral shape of these was generated by overlaying triggered events with random data samples. The CNO and pep neutrino rates were fixed to the SSM prediction, whereas for the ^{7}Be neutrinos the value was taken from [68]. The other contribution were left as free parameters. The fit returns an interaction rate of $(144 \pm 13_{\mathrm{stat}} \pm 10_{\mathrm{syst}})$. The absence of a pp neutrino signal could be excluded with 10σ. If one applies the latest neutrino oscillation parameters the resulting pp neutrino flux is:

$$\Phi_{\mathrm{pp}} = (6.6 \pm 0.7) \cdot 10^{10} \mathrm{cm}^{-2}\mathrm{s}^{-1} \tag{2.7}$$

which is in good agreement with the SSM prediction of $(5.98 \cdot (1 \pm 0.006)) \cdot 10^{10} \mathrm{cm}^{-2}\mathrm{s}^{-1}$. The unoscillated predicted flux compared to the measured flux results in a survival probability of $P_{ee} = 0.64 \pm 0.12$, constraining the MSW-LMA solution at the very low energies. Further on Borexino performed the first simultaneous fit of solar pp, pep and ^{7}Be neutrino fluxes [30] based on 1292 days of data taken between December 2011 and May 2016.The fit is based on a binned likelihood function that uses the spectral shape and as well the radial distribution of the events. Table 2.1 shows the results obtained by the analysis. For the pp neutrinos the uncertainty was reduced by 20%. The uncertainty for the ^{7}Be neutrinos could be reduced to 2.7%, which is below the theoretical uncertainty. To break the degeneracy between the ^{210}Bi background and the CNO signal, the CNO interaction rate is limited to the prediction by the high metallicity (HZ) SSM. The analysis is repeated with values given by the low metallicity(LZ) SSM. Therefore there are are two

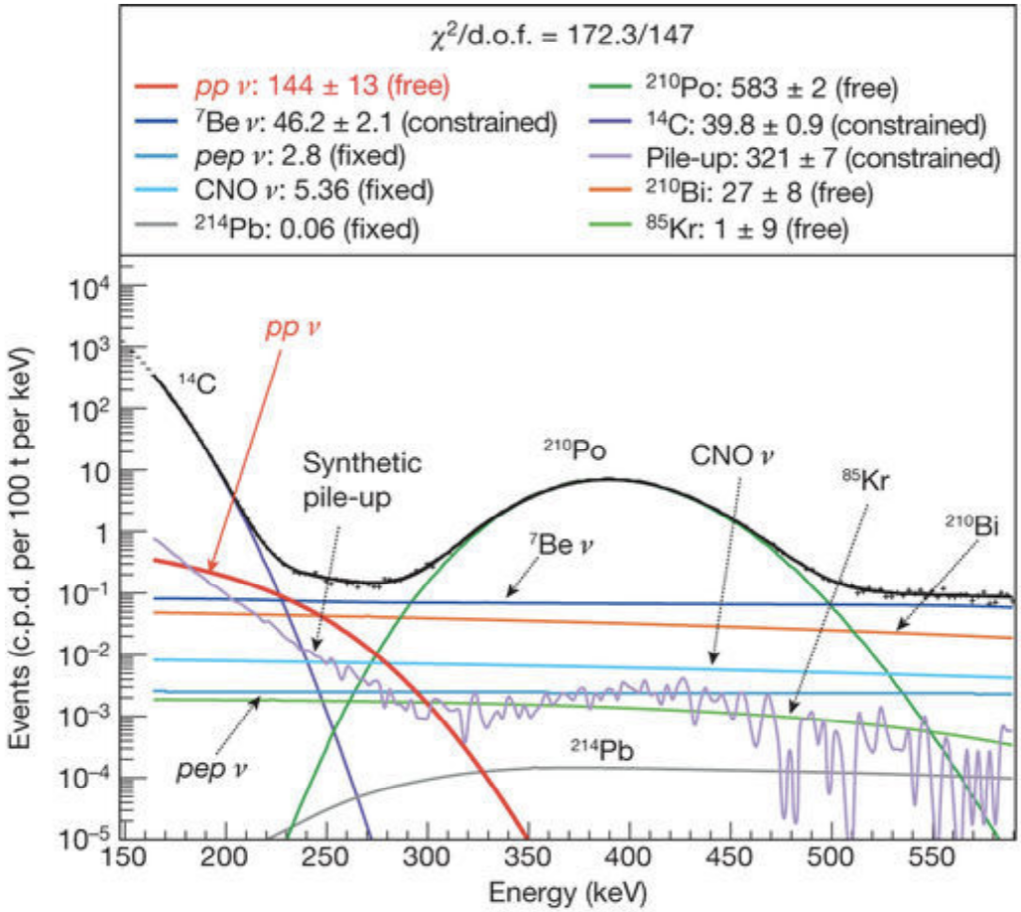

Figure 2.5: Borexino data in the pp energy region collected between January 2012 and May 2013. The fit includes the pp neutrino signal (red) as well as free and constrained background components, as marked in the legend.

values given for the pep neutrino rate. However an absence of a pep neutrino signal is excluded at 5σ. For the CNO neutrino rate just an upper limit was achieved, as the ^{210}Bi rate could not be determined independently. However the inclusion of the pp neutrinos allows to constrain the pep signal via their well known theoretical connection. Therefore a weaker assumption has to be made than in [12].

2.2.2 Geoneutrinos

Geo neutrinos are emitted by naturally abundant radioactive isotopes in the terrestrial matter. The dominant ones are the ^{238}U and ^{232}Th chains and ^{40}K. In their beta decay they emit anti neutrinos. The detection of these

allows to study the distribution of the isotopes in the earth crust and to test the Bulk Silicate Earth(BSE) models that describe this distribution[76]. Furthermore, a measurement would give the radiogenic share of the total earth heat flow of (47±2)TW [77]. Borexino detects these neutrinos via the inverse beta decay (IBD). As the threshold for this reaction is 1.8 MeV, Borexino is not sensitive to ^{40}K neutrinos with and endpoint of 1.4 MeV and relies on the ^{238}U and ^{232}Th chains. In 2010 the Borexino collaboration released the first hint for geo neutrinos at the 3σ level[69]. In 2015 a spectroscopic measurement could be achieved[13]. Finally in 2019 a comprehensive analysis of geo neutrinos based on 3263 days of Borexino data was released[78]. A major background are the cosmogenic radioisotopes ^{9}Li and ^{8}He. They are created via spallation processes on ^{12}C by cosmic muons. They are handled by different vetos after cosmogenic muons which consider the muons energy, which subdetector fired and if a neutron was created. The dominant background arises due to anti neutrinos created in nuclear power plants. However the LNGS benefits from a general shutdown of nuclear power plants in Italy in 1990 so that the mean weighted distance from the LNGS to a power plant is $\simeq 1200$ km [70]. The result of an unbinned likelihood fit with the ratio of ^{238}U to ^{232}Th is shown in figure 2.6. The fit gives a geo neutrino signal of

$$\mathrm{S_{geo}} = (46.3^{+9.1}_{-7}(\mathrm{stat.})^{+2.4}_{-1.9}(\mathrm{syst.}))\mathrm{TNU} \tag{2.8}$$

and a reactor signal of

$$\mathrm{S_{rea}} = (79.7^{+11,3}_{8,5}(\mathrm{stat.})^{+4.1}_{-4.4}(\mathrm{syst.}))\mathrm{TNU} \tag{2.9}$$

with 1 Terrestrial Neutrino Unit(TNU) being one event per year and 10^{32} protons. Assuming the contribution from ^{40}K to be 18% the total radiogenic heat was determined to be:

$$\mathrm{H_{rad}(U+K+K)} = 38.2^{+13.6}_{-12.7}\ \mathrm{TW} \tag{2.10}$$

The precision is not sufficient to exclude any BSE model at 3σ. However, it favors models with high radiogenic power, corresponding to a cool temperature at earth's formation. If one restricts the reactor antineutrinos to the expected values and assumes a chondritic mass ratio of U/Th=3.9, Borexino can exclude a georeactor at the earth's core with a 95% confidence level. By constraining the contribution of the bulk lithosphere to expectation of 28.8±5.6 events, the signal from the mantle could be determined to be:

$$\mathrm{S_{mantle}} = 20.6^{+10.2}_{-8.4} \tag{2.11}$$

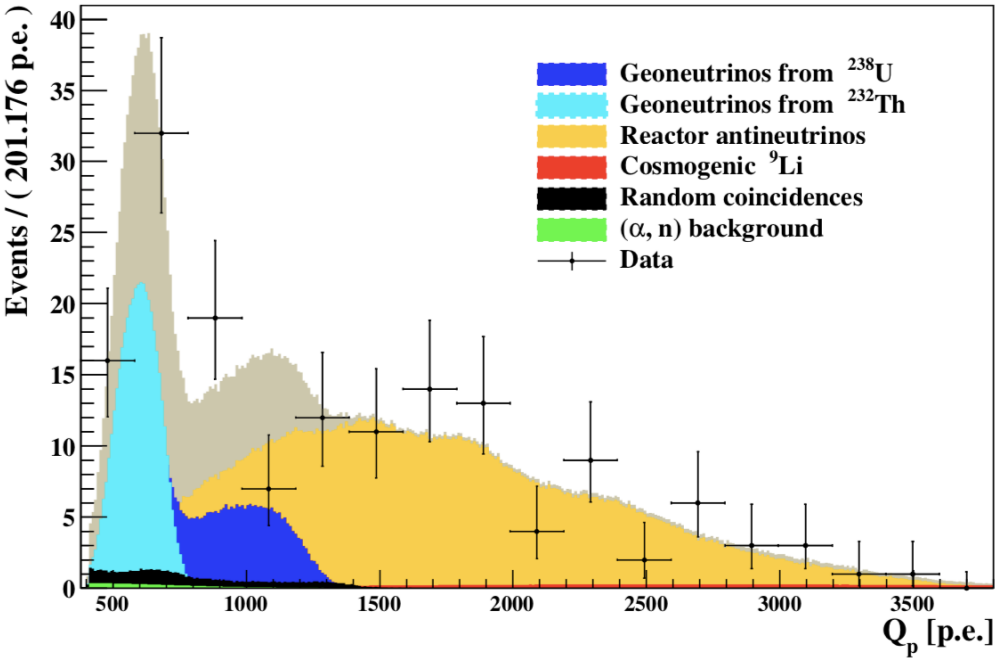

Figure 2.6: 154 geoeneutrino candidates based on 3263 days of Borexino data. The contribution from ^{238}U (dark blue) and ^{232}Th (cyan) are free parameters. The reactor anti neutrinos are show in yellow. The total fit function is depicted in beige.[78]

Supernova Neutrinos

As described in section 1.5 supernovae are one of the brightest neutrino sources. About 99% of their energy is released via neutrinos, translating to $\simeq 10^{58}$ emitted neutrinos in a typical supernova [79]. The Borexino detector allows to detect supernova neutrinos via various channels, namely elastic scattering on electrons and protons, inverse beta decay and inelastic scattering on carbon. This would yield in $\simeq$ 190 in a 10 s burst for a typical supernova at 10 kpc distance with a released gravitational energy of $\simeq 3 \cdot 10^{53}$erg. Such an event would allow to test several supernova models, give neutrino mass limits and possibly give a hint on the neutrino mass hierarchy. In 2009 Borexino joined the Supernova Early Warning System (SNEWS) collaboration. The collaboration is formed by neutrino detectors that are sensitive to galactic core collapse supernova. Current members are Super-Kamiokande[80], LVD[81], Ice Cube[82] and Borexino. The neutrino burst will arrive several hours before the optical signal at earth. It will trigger several of the detectors in coincidence. Based on the timing difference

SNEWS can give astronomers a direction where the light signal is expected.

Chapter 3

Detection Channel & Data Selection

3.1 Elastic Neutrino Scattering

Borexino detects solar neutrinos via elastic scattering (ES) of neutrinos on electrons:

$$\nu_{\mathrm{x}} + \mathrm{e}^{-} \rightarrow \nu_{\mathrm{x}} + \mathrm{e}^{-} \tag{3.1}$$

The ES channel features no intrinsic energy threshold. Therefore it is given solely by detector performance and background levels. Figure 3.1 presents

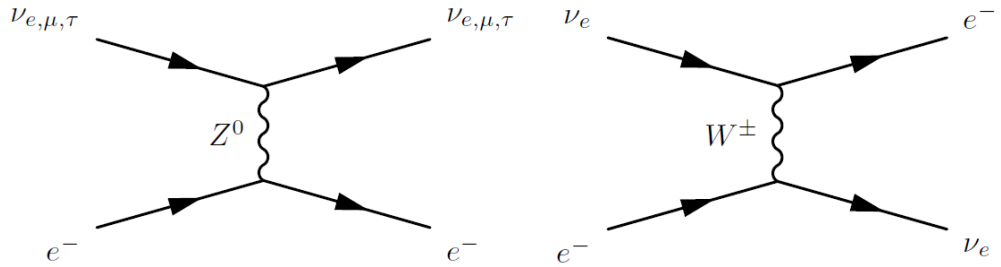

Figure 3.1: First order Feynman diagrams for neutrino-electron scattering. *Left*: Neutral current reaction through z^0 exchange, possible for all neutrino flavours. *Right*: Charged-current reaction through $\mathrm{W}^{\pm}$ exchange. For solar neutrinos only electron neutrinos can interact in this way.

the two possible reactions. All neutrino flavours can scatter via the neutral current channel, as there is no change in the flavour eigenstate. For solar neutrinos only electron neutrinos can scatter via charge current. The solar neutrino energy is well below the muon and tauon rest mass, so a charged

current reaction is not possible for these flavours. Hence, the cross section for electron neutrinos is increased by a factor of about six.
The differential cross section for producing a recoil electron with the kinetic energy T and a neutrino energy of E_ν is [83] is given by:

$$\frac{d\sigma}{dT}(T, E_\nu) = \frac{\sigma_0}{m_e c^2}\left(g_L^2 + g_R^2\left(1 - \frac{T}{E_\nu}\right) - g_L g_R \frac{m_e c^2 T}{E_\nu^2}\right) \tag{3.2}$$

with

$$\sigma_0 = \frac{2G_f^2 m_e^2}{\pi \hbar^4} \tag{3.3}$$

$$g_L = \sin^2(\Theta_W) + \frac{1}{2}(\nu_e - e \text{ scattering}) \tag{3.4}$$

$$g_L = \sin^2(\Theta_W) - \frac{1}{2}(\nu_\mu - e \text{ scattering}) \tag{3.5}$$

$$g_R = \sin^2(\Theta_W) \tag{3.6}$$

with the electron mass m_e, the Weinberg angle Θ_W and the Fermi constant G_F. For $E_\nu \gg m_e$ the cross section is can be approximated by:

$$\sigma_{\nu_e} = 9.2 \cdot 10^{-45} \frac{E_\nu}{\text{MeV}} \text{cm}^2 \tag{3.7}$$

$$\sigma_{\nu_{\mu/\tau}} = 1.5 \cdot 10^{-45} \frac{E_\nu}{\text{MeV}} \text{cm}^2 \tag{3.8}$$

Figure 3.2 depicts the cross section for elastic (anti) neutrino electron scattering and shows the slight difference of a factor 2-3. The inverse beta decay cross section (introduced in chapter 10) is larger by two orders of magnitudes. However, it features an energy threshold of 1.8 MeV, where for the elastic scattering there is no threshold.
In Borexino, the scattered neutrino leaves the detector undetected and the electron's kinetic energy is measured. As the electron's energy depends on the scattering angle, it is not possible to measure the neutrino's energy on an event by event basis. With the approximation $m_\nu = 0$ the electron's recoil energy is restricted to:

$$E_{e,max} \leq \frac{2E_\nu^2}{m_e + 2E_\nu}, \tag{3.9}$$

with the electron restmass m_e and the neutrino energy E_ν. Hence, mono energetic neutrinos, like the solar ^{7}Be neutrinos, form a compton like recoil spectrum. Continuous spectra, like the ^{8}B neutrino spectra, are shifted to lower energies and smeared.

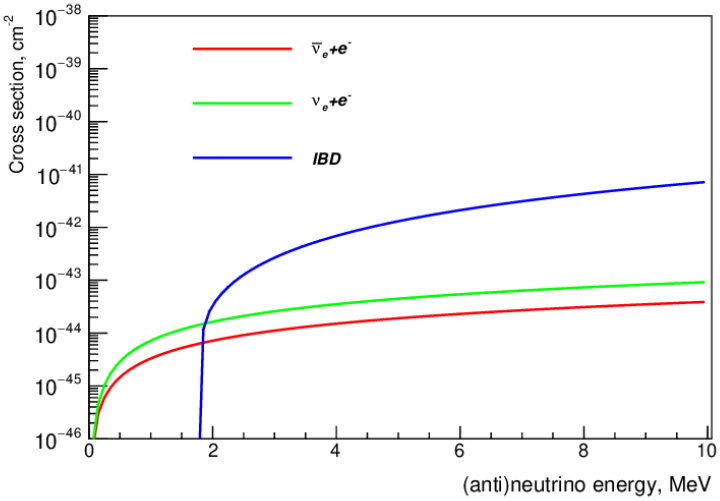

Figure 3.2: Cross section for elastic (anti) neutrino-electron scattering together with the roughly two magnitudes larger cross section for the inverse beta decay introduced in chapter 10 [84]

3.2 Stable Neutron Detection

A large energy deposition by cosmogenic muons in the scintillator is usually accompanied by neutron production. In this process also various cosmogenic radioisotopes can be produced, see section 5.4 for further details. Hence, a stable and efficient neutron detection is crucial for low rate analyses. In Borexino this is given from January 2008. When a muon crosses the detector it prompts the standard trigger gate with a length of 16 μs. With a mean capture time of 256 μs for neutrons produced by spallation, 6% of them fall into the standard trigger gate [85] including the muon. To capture the remaining neutron a new trigger was introduced. After the Inner Detector (ID) or Outer Detector (OD) identifies an event as muon, second trigger gate with a length of 1.6 is issued. This second trigger called trigger type 128 collects the remaining neutrons.

3.3 Water Extraction

The various solar neutrino analyses in the Borexino experiment depend on an ultra pure scintillator. Therefore the scintillator was purified on site, before filling, with the help of distillation, nitrogen stripping and water extraction [86]. The design goal for contaminations originating from the Uranium/Thorium decay chains of $< 10^{-16}$ g/g was surpassed by more than one order of magnitude after filling the detector. However in 2010 the collaboration decided to clean the scintillator even further and to remove further contaminations from dust i.e. ^{238}U, ^{232}Th and ^{40}K and air i.e ^{39}Ar and ^{85}Kr. For this purpose there are connections at the top and bottom of the buffer and active volume to the cleaning plants next to the detector, so that it is possible to loop the scintillator through the cleaning plants. For this purification only the water extraction method was used. In the plant the scintillator is mixed with ultra pure water which makes Impurities that are water soluble move to the water. Additionally water has strong dipole moment, that increases this effect. A detailed description of the procedure is given in [87]. The water extraction was carried in a test cycle in 2010 and six additional cycles during 2010 and 2011. The operation was successful and decreased the impurities by another order of magnitude. The success is clearly visible in the ^{212}Bi- ^{212}Po coincidence (see section 4.1.1 for details) rate, that lies within the thorium chain, shown in figure 3.3. After the extraction there are hardly any events. Despite careful checking for air tightness, radon

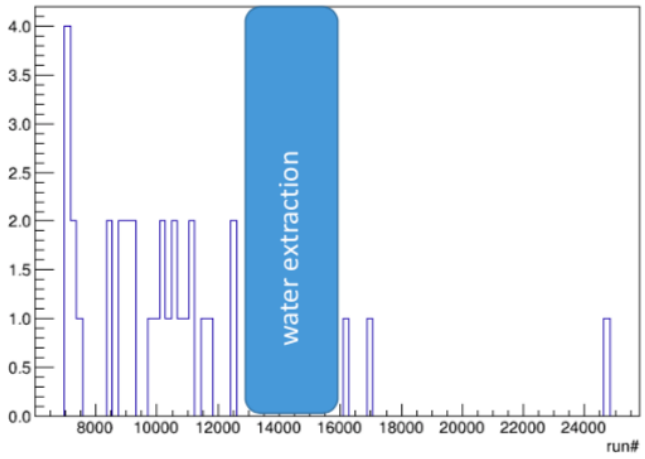

Figure 3.3: Number of ^{212}Bi- ^{212}Po per run. The blue box marks the time of water extraction operations. Afterwards the ^{212}Bi- ^{212}Po rate is significantly reduced.

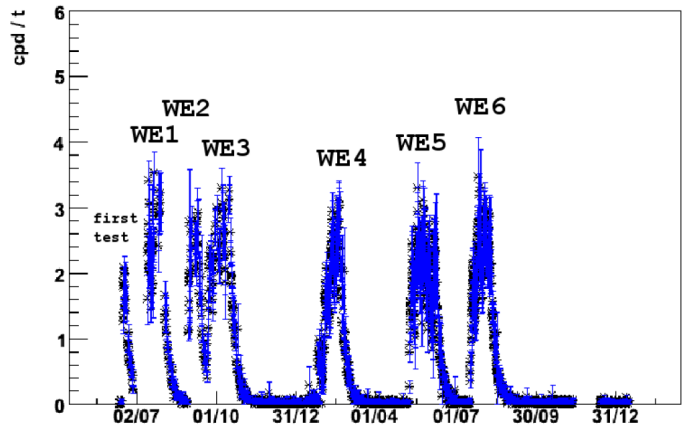

Figure 3.4: Radon counts during the water extraction period. During each water extraction a spike in the radon count rate is visible with a subsequent decay.

,i.e. ^{222}Rn, was introduces to the scintillator during operations and therefore distributed in the whole Inner Vessel (IV). The Borexino background monitor shown in figure 3.4 shows a clear peak during each water extraction cycle and during the test run in the ^{222}Rn rate. ^{222}Rn undergoes an alpha decay with Q=5.6 MeV and a half life of $t_{1/2}$ = 3.8 d with several decays afterwards with half lifes in the order of minutes, especially the ^{214}Bi- ^{214}Po coincidence described in section 4.1.2. To remove ^{222}Rn and its daughters all runs during which water extraction was performed plus runs tens days after the end of operations are removed from the dataset.

3.4 Total Exposure

The detection volume is given by the volume of the IV. Despite great efforts on low radioactivity for the IV compared to the scintillator the rates of decays in the Uranium and Thorium chains on the IV is rather high. This is used to monitor the shape of the IV via fast coincidences, especially the ^{212}Bi- ^{212}Po coincidence (see section 4.1.1 for details). The beta decays are point like events and follow the shape of the IV. The IV shape is fitted to these events on a weekly basis. The result is shown in figure 3.5. The nominal shape of

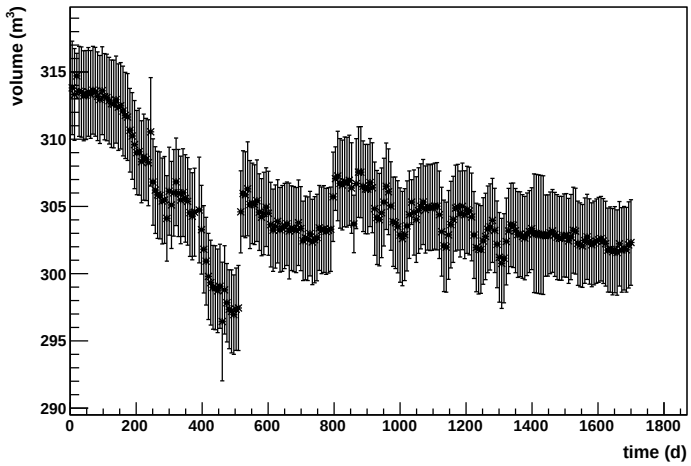

Figure 3.5: Volume inside the inner vessel, monitored via coincidence events

the IV is sphere, however there are deviations visible. The dip is caused by a leak in the IV that started to appear in 2008 that is located in the upper part of the IV. In 2009 the IV was refilled, indicated by the step in figure 3.5. Also in 2009 the DMP concentration in the buffer region was adjusted to align the density inside the IV to the buffer liquid. This operation lead to a minimal leak rate and a stable detector configuration. This lead to an exposure for this analysis of 3075.7 live days of data taking corresponding to an exposure of 2.54 kt years.

Chapter 4

Backgrounds

The detector materials were carefully selected for their radiopureness [9]. The onion like structure of Borexino with cleaner materials towards the centre of the detector provides self shielding. However the materials still constitute a background for the neutrino analyses. The one relevant for the ^{8}B neutrinos will be presented in this chapter.

4.1 Internal Backgrounds

Internal backgrounds are due to impurities in the scintillator. In section 3.3 the successful cleaning campaign that reduced them is presented. The relevant decays that contribute are presented in the following.

4.1.1 ^{208}Tl Rate Determination

In the ^{232}Th decay chain ^{208}Tl (β^-decay, $\tau = 4.47\,\mathrm{min}, \mathrm{Q} = 5.001\,\mathrm{MeV}$) is the only one contributing to the background above 3 MeV. Since ^{208}Tl is a β^- emitter an event by event identification is not possible and it has to be subtracted statistically. ^{208}Tl is a daughter nuclide of ^{212}Bi with a branching ratio of 36%. The decay possibilities for ^{212}Bi are shown in figure 4.1. Its decay rate can be determined via the ^{212}Bi-^{212}Po coincidence, since it is tagable. Events with 20-1200 photo electrons and 500-600 photo electrons are considered ^{212}Bi and ^{212}Po events, respectively, corresponding to detection efficiencies of $\epsilon_{\mathrm{Bi}} = 1$ and $\epsilon_{\mathrm{Po}} = 0.911$. The chosen timegate is $400\mathrm{ns} < \delta\mathrm{t} < 1200\mathrm{ns}$ corresponding to an efficiency of $\epsilon_{\Delta\mathrm{t}} = 0.346$. Within the detector resolution the events are in the same place. If the delayed signal signal is in a sphere of 1 m radius with the prompt signal in the center, it fulfills the coincidence conditions. This results in a spacial efficiency of nearly $\epsilon_{\vec{\mathrm{r}}} = 1$.

These efficiencies combined result in an detection efficiency of:

$$\epsilon_{\text{detection}} = \epsilon_{\text{Bi}} \cdot \epsilon_{\text{Po}} \cdot \epsilon_{\Delta t} \cdot \epsilon_{\vec{r}} = 0.315 \tag{4.1}$$

With this efficiency 30 ± 5.5 ^{212}Bi-^{212}Po-events are found within the data set. Given that 94.4% of the ^{208}Tl spectrum is above 3 MeV and considering the branching ratios in figure 4.1 this leads to 50.7 ± 7.1 ^{208}Tl-events within the data set.

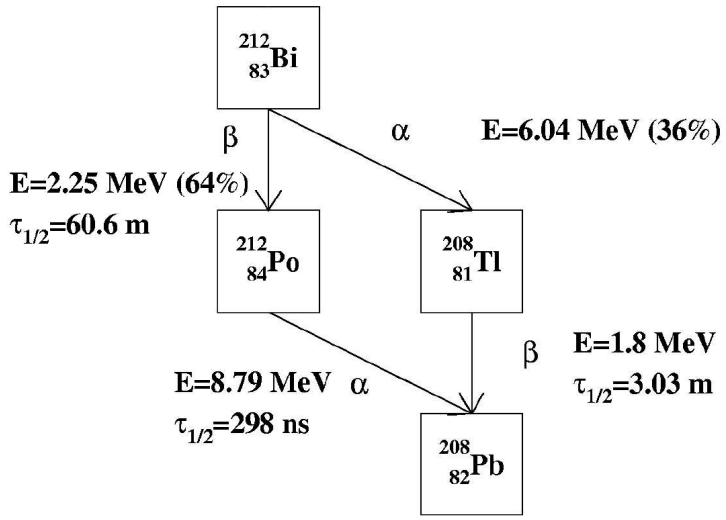

Figure 4.1: Decay possibilities of ^{212}Bi.

4.1.2 ^{214}Bi Discrimination

^{214}Bi ($\beta-$ decay,τ =19.9 min, Q=3.2 MeV) is an intrinsic background originating from the ^{238}U chain. It can be easily vetoed via the ^{214}Bi-^{214}Po coincidence. ^{214}Po α decays with a lifetime of $\tau = 237\mu$s and with Q=7.7 MeV. Events with an energy of 0.18-3.6 MeV are tagged as ^{214}Bi events and events with an energy of 0.4-1 MeV are considered as ^{214}Po events. Events in a time window of 20-1200μs after the first event and within a sphere of 1 m radius are tagged as coincident events. The efficiency of these coincidence conditions has been validate via Monte Carlo simulations to be $\epsilon_{^{214}\text{Bi}-^{214}\text{Po}} = 90\%$ [66]. The remaining ^{214}Bi rate is $(1.1 \pm 0.4) \cdot 10^{-4}$cpd/100t and can be neglected.

4.2 External Background

The origin of the external background is the material surrounding the scintillator, i.e. pmts, winston cones, vessel plus mounting and stainless steel sphere(SSS). The distance between these and the active volume is several meters, therefor only gamma rays can reach it. The vessel is slightly shifted upwards (see figure 7.2), therefore there are more external events in the top sphere. Isotopes contributing to the external background are ^{208}Tl (β^-decay, $\tau = 4.47\,\text{min}$, Q = 5.001 MeV) and ^{214}Bi (β^- decay , τ=19.9 min, Q=3.269 MeV). Their respective decay schemes are shown in figure 4.2. ^{208}Tl is emitting a 2.6 MeV gamma whereas ^{214}Bi emits several gammas up to 3.2 MeV. Throughout the here presented analysis a threshold of 3 MeV is used, however due to the detector's resolution part of the 2.6 MeV gammas are leaking above the threshold. Borexino offers the ability to put calibration sources inside the buffer volume via pipes [9]. A ^{228}Th/^{208} gamma source was put in place. These sources allow to compare the radial distribution of simulated external events with real ones. Figure 4.3 shows the comparison of the 2.6 MeV gammas with the source gammas. The distributions match very well with a χ^2/NDF slightly below one. The same was done with a spectral comparison with similar results [66].

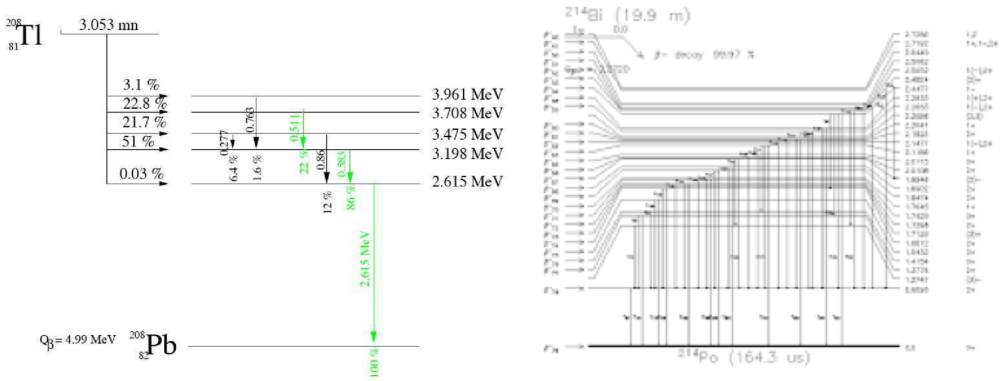

Figure 4.2: Decay schemes of ^{208}Tl and ^{214}Bi especially including the created gamma rays.[88]

Figure 4.4 shows the radial distribution of events above 6 MeV, where the blue line shows a r^2 distribution. It is clearly visible that there is a non r^2 distributed component. As ^{208}Tl is the internal with the highest Q-value, none of these can cause this distribution. This excess can be explained by high energetic gamma rays created by the capture of a radiogenic neutron produced via (α,n) reactions[89]. The Stainless Steel Sphere (SSS) ~45 t

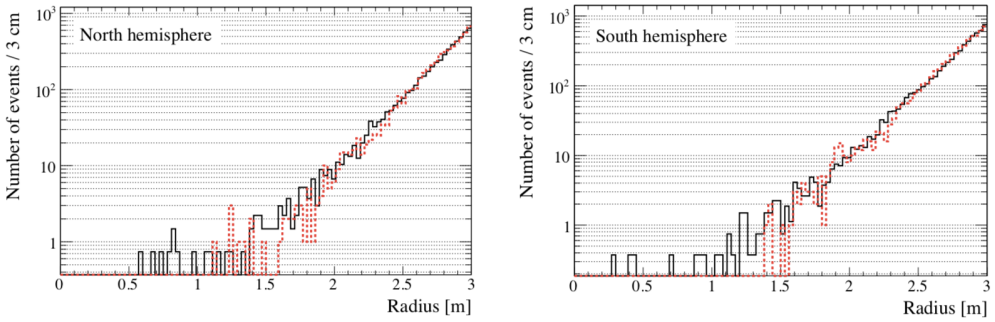

Figure 4.3: Cross check of the radial monte carlo response using an external thorium source[66]

and the PMT Glas ∼0.8 kg x 2212≈1.7 t are the two massive detector structures with non neglectable ^{238}U, ^{235}U and ^{232}Th contamination, that provide the alpha particles. The corresponding neutron flux was introduced to the Borexino simulation. It showed that the main contribution to the excess is neutron capture on carbon in the buffer with 5MeV and neutron capture on iron in the SSS with energies up to 10 MeV. The total rate is calculated to be 0.545±0.05 cpd/100 t [89].

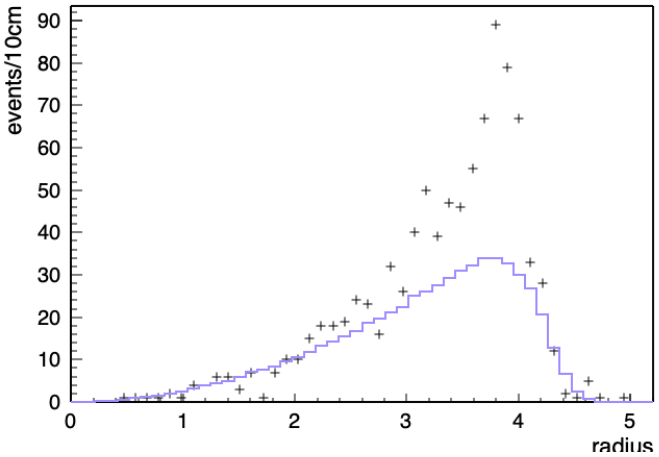

Figure 4.4: Radial distribution after cuts and above 6 MeV. Only homogenous distributed events (blue line) were expected, the excess created by high energy gammas is clearly visible.

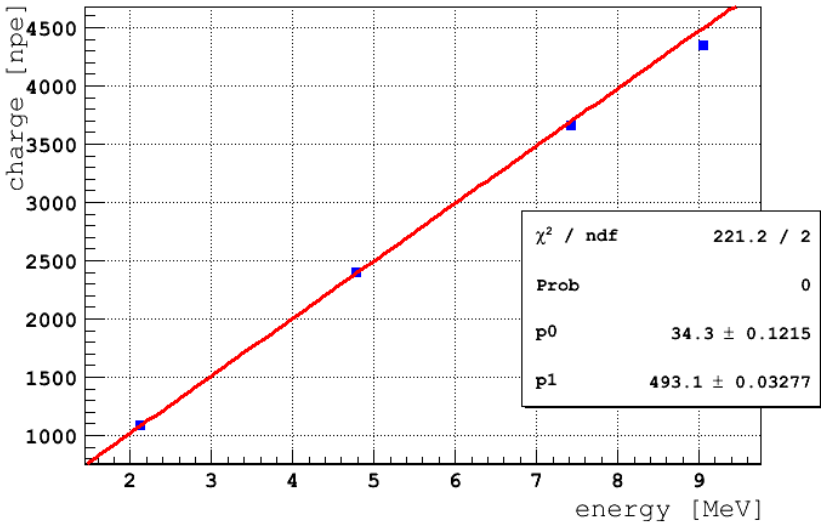

Figure 4.5: Blue dots mark measured peak position induced by neutron capture on ^{1}H (2.2 MeV), ^{12}C (4.9 MeV) , ^{56}Fe (7.6 MeV) and ^{54}Fe (9.9 MeV) in the detector center. The red line marks a linear fit through the data points.

4.3 Energy Cut

The 2.6 MeV ^{208}Tl gammas and most of the ^{214}Bi gammas are below 3 MeV. However, due to the high rate and the detectors energy response [66] the events can be reconstructed at higher energies. Furthermore Borexino's self shielding is limited, due to its small size. Therefore, the here presented analysis is limited to a lower energy threshold of 3 MeV.
To calibrate the detectors energy response, there is the possibility to position a ^{241}Am^{9}Be source at the center of Borexino [90]. This source is a strong neutron source. The neutrons get captured on ^{1}H and ^{12}C from the scintillator and on ^{56}Fe and ^{54}Fe from the insertion system producing characteristic gammas with energies of 2.2 MeV, 4.9 MeV, 7.6 MeV and 9.9 MeV, respectively. The peaks are used to calibrate the charge output described in section 2.1.1. The detector's response can be parameterised with:

$$N = a \cdot E + b \tag{4.2}$$

with N being the detected photo electrons (pe), a=493 pe/MeV and b=34 pe The 3 MeV energy threshold corresponds to 1513 pe. The result is shown in figure 4.5.

Chapter 5

Cosmogenic Muons

The solar neutrino interaction rate is rather low. Therefore, Borexino is build in the Laboratori Nationali del Gran Sasso (LNGS) which features a rock overburden of roughly 1400 m equalling to 3800 m.w.e. This reduces the cosmic muon flux at the surface of $(180 \pm 20) \mathrm{m}^{-2}\mathrm{s}^{-1}$ [91] by roughly six orders of magnitude to $1.2\,\mathrm{m}^{-2}\mathrm{h}^{-1}$, resulting in 4300 muons crossing the Stainless Steel Sphere (SSS) per day. As low energetic muons are stopped in the rock, in underground labs the mean muon energy is higher compared to surface level. For the LNGS the mean muon energy is $(270 \pm 21)\,\mathrm{GeV}$[92]. Muons reaching the Borexino detector are minimal ionising particles and hence loose 2 MeV/cm in the scintillator. The ones crossing the Inner Vessel (IV) therefore deposit 50 MeV to 2 GeV, which is well above solar neutrino energies. However in the buffer region the light output is quenched and muons crossing it pose direct background for solar neutrino analysis. Furthermore, high energetic muons can create electromagnetic and hadronic showers and in doing so create secondary particles. Neutrons and radioisotopes with lifetimes up to $\tau \sim 1\,\mathrm{s}$ are vetoed by a veto with the parent muon. However for the long lived $^{10}\mathrm{C}(\tau = 27.8\mathrm{s})$ and $^{11}\mathrm{Be}(\tau = 19.9\,\mathrm{s})$ it is not possible as it would result in a 100% dead-time. See also chapter 5.4. This chapter focuses on the muon detection of the two Borexino sub-detectors, the inner detector (ID) and the outer detector (OD). As there is no light propagation possible between the two sub-detectors, they represent two independent means of muon detection. Their working principle and efficiencies will be described in the following.

5.1 Muon Detection

Borexino consists of the Inner Detector (ID) and Outer Detector (OD). The two are separated by the Stainless Steel Sphere (SSS), through which there is

no light propagation possible. Therefore Borexino provides two subdetectors for muon identification. A muon crossing the scintillation volume has to cross both detectors, which improves the muon identification in the sensitive volume considerably. In the following both subdetectors and their combined efficiency will be presented.

5.1.1 Outer Detector Muon Detection

The outer detector (OD) with 18 diameter and 16,9 m height is filled with 2400 t of ultrapure water. Muons crossing the detector will emit Čherenkov light. The light is detected by 208 PMTs, where 154 are mounted on the Stainless Steel Sphere (SSS) and 54 on the water tank's floor. The Muon Trigger Board (MTB) issues a trigger if within a time window of 150 ns 6 PMTs fire. The trigger threshold is tuned to avoid dark noise, however light entering the detector, especially caused by cable feed throughs at the detector's top, may trigger the MTB. The MTB constitutes a hardware trigger made of a custom built 6U VME unit for the Borexino experiment. The OD provides another option to identify muons, the Muon Clustering algorithm. It is a software based trigger, that searches the OD data neighbouring PMTs that fired. Furthermore the PMTs are divided in the ones mounted on the SSS and the ones on the floor. An event is classified as muon if at least 4 PMTs in one subset fire within a time window of 150 ns [93]. The MCR is not sensitive to light leaks as the MTB. However due to the light leaks and dark noise there is a small over efficiency in the OD, yet neglect able as the probability to veto an event in the Inner Detector (ID) is $\leq 10^{-5}$ [85].

5.1.2 Inner Detector Muon Detection

Most physics events in the ID are point like, especially neutrino events, whereas a muon traverses the whole detector and deposits energy along its way. Hence, muons create longer pulses than point like events. Therefore a muon identification via pulse shape discrimination is possible.
Figure 5.1 shows the two variables that are used for muon identification. The mean time of a pulse is here defined as the average time difference of a pmt hit to the onset of a pulse while the peak time is the duration from the pulse's onset to its maximum. For higher energies muons are clearly separated in both variables. For lower energies just the peak time is used as discrimination parameter. The exact values are summarised in table 5.1.

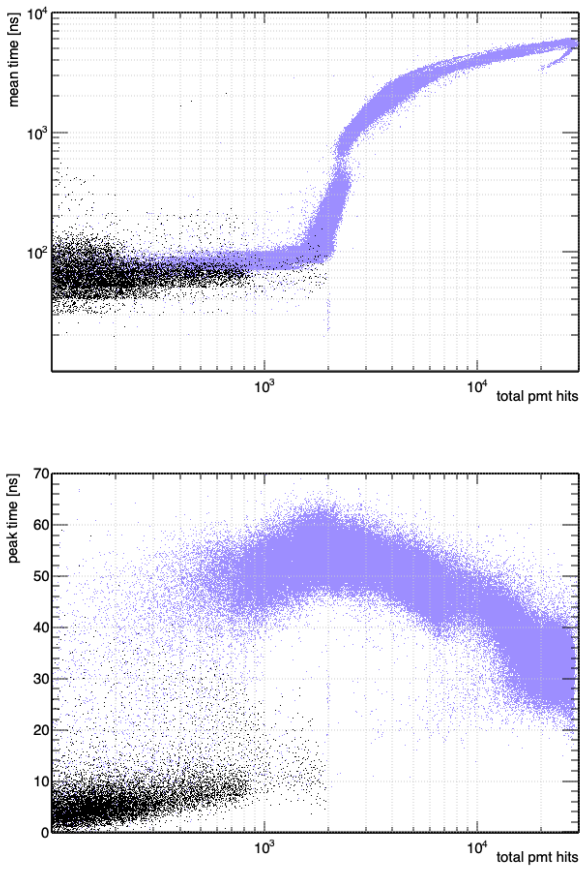

Figure 5.1: Pulse shape variables used for muon identification in the Inner Detector. As muons travel through the whole detector they produce longer pulses. Point like events are marked black, muon like events blue. *Left:* The average time difference of a pmt hit to the onset of a pulse versus the total hits of the event. *Right:*Time difference of the pulses onset to its peak versus total energy.

number of pmt hits	peak time	mean time
100 - 900	> 40 ns	-
900 - 2100	> 30 ns	-
>2100	-	> 100 ns

Table 5.1: Values of the pulse shape parameters that are used to identify muons in Borexino's inner detector dependant on the deposited energy.

5.2 Muon detection efficiency

The different paths that muons can take through the Borexino detector are depicted in figure 5.2. For this work two subsamples are of interest, namely muons crossing just the OD, from now on called OD muons, and muons crossing the inner vessel or the buffer region, from now on called ID muons. An event is identified as an OD muon if the MCR or the MTB triggers but there is no light in the ID. An event is classified as an ID muon if one of the following is fulfilled, the MCR or MTB triggers and there is light in the ID if an ID event is identified as a muon by the IDF. To study the muon

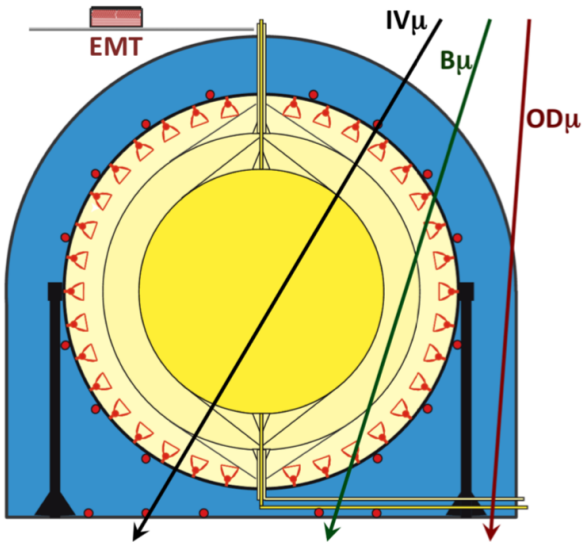

Figure 5.2: Definition of the muon subsamples. Muons crossing just the OD are named OD muons, the ones crossing the buffer or inner vessel ID muons. [93]

detection efficiencies of the Borexino subdetectors a pure muon sample is needed. In the study of the OD a sample based solely based on the ID is used

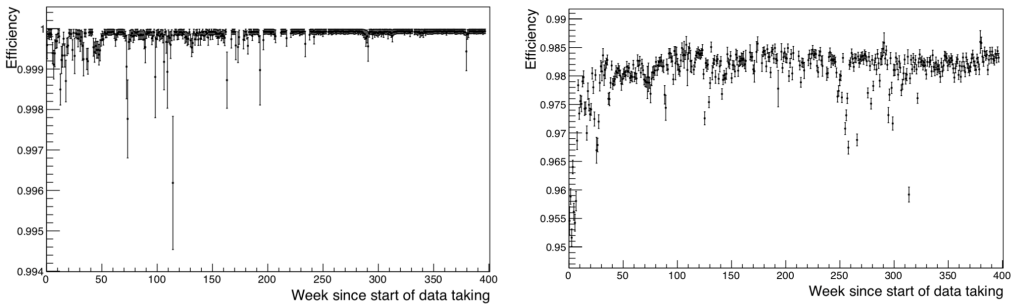

Figure 5.3: Muon detection efficiencies of the Borexino Outer Detector (OD) on the left and Inner Detector (ID) on the right. [94]

as the MTB and MCR are highly correlated. Furthermore, in means of light propagation the ID and OD are completely detached from each other. The muon sample consists of events tagged by the IDF. It would also be possible to just use very high energetic events (∼above 30 MeV). However, there would be more contaminations expected as the IDF is tuned to have a minimal over efficiency. It is nonetheless unavoidable to have a small contamination of fast neutrons and CC and NC interactions of atmospheric neutrinos in the muon sample [94]. Therefore, the calculated numbers represent a lower limit of the muon detection efficiency. Independent of the muon's track, if it reaches the ID, it has to cross several meters of water within the OD. Therefore, it is assumed that for all muon tracks crossing the ID, the muon sample based on the IDF is suitable [93]. However, the OD is tuned to detect muons coming from above, since most muons are expected from this direction as for flatter angles the shielding gets larger. Since the ID is spherical there is no systematics expected in the muon sample provided by the IDF.
The spikes to lower efficiencies in figure 5.3 in the OD muon detection efficiency originates from run where the MCR was not active. Nevertheless, even without the MCR the MTB provides a muon detection efficiency greater tan 99.6%, so no runs have to be discarded. For the IDF tag in figure 5.3 the whole ID volume is used i.e. also the buffer region where the light output is suppressed by roughly a factor of twenty compared to the IV. Hence, for muon tracks in the buffer region there is less light to perform the pulse shape analysis. Furthermore, at the buffer's edge the muon tracks get shorter, which shortens the pulse. This implies that deviations from one in the muon detection efficiency in the ID are mainly caused by buffer muons. Muons crossing the IV, especially muons crossing the fiducial volume generate an abundance of light. They also have the longest tracks through the detector, which generates long pulses and eases it to differentiate them from point like

events. This results in an efficiency close to one for the most critical muons going through the active volume.

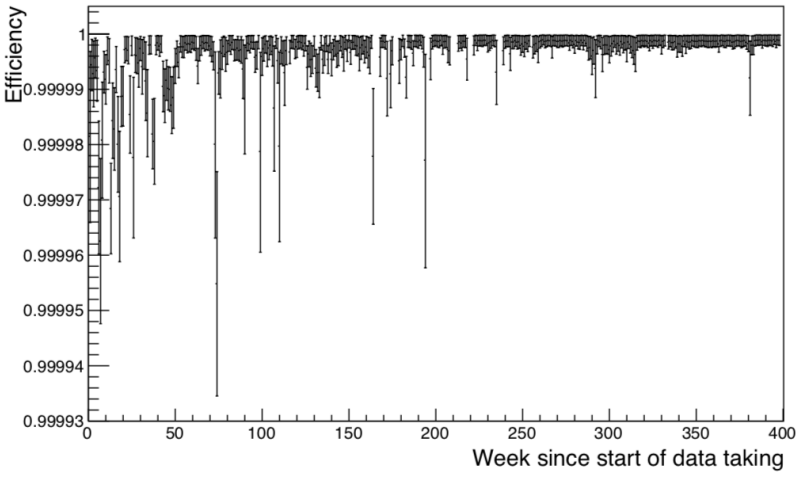

Figure 5.4: Combined muon detection efficiencies of the Borexnio subdectors over time which lies permanently above the design goal of 99.992% [94].

5.3 Cosmogenic Neutrons

Cosmogenic muons crossing the ID can produce neutron through spallation on ^{12}C. These spallation processes can be accompanied by radioisotope production, mainly ^{10}C and ^{11}C. As a free neutron is a sign for ^{10}C and ^{11}C production, it is crucial to detect the free neutrons.
The standard Borexino trigger gate of 16μs is not long enough to detect all neutrons due to the mean capture time of $\simeq$ 260μs. Therefore after each muon crossing the ID the so called neutron trigger gate with a length of 1.6ms is opened, corresponding to the maximum the Borexino electronics can provide. The neutrons are produced by a muon and eventually captured ,on ^{1}H and ^{12}C with a lifetime of $\tau = 260\mu$s, emitting characteristic gammas with an energy of 2.23 MeV and 4.95 MeV, respectively. Due to the cross sections for thermal neutron capture of $\sigma\left(^{1}\mathrm{H}\right) = (332 \pm 07)$ mb and $\sigma\left(^{12}\mathrm{C}\right) = (3.89 \pm 0.06)$ mb and the scintillator's chemical composition ($C_6H_3(CH_3)_3$), 99% percent of the neutron captures are located on hydrogen. Figure 5.6 shows a typical muon event with several neutron captures afterwards. The high noise level at the beginning is caused by muons illuminating all pmts with scintillation and Cherenkov light. This high light yield causes ionic after pulses in the pmts. The noise baseline in the neutron trigger gate

is caused by accidental coincidences, mostly ^{14}C. To identify all the neutron captures despite the noise caused by muons, in [85] and advanced algorithm was developed. The result is a detection efficiency of $\epsilon_{\mathrm{det}} = (92.0 \pm 1.7)\%$ and a neutron rate of $\mathrm{R(n)} = (90.1 \pm 2.0_{\mathrm{stat}} \pm 2.4_{\mathrm{syst}})(\mathrm{d100t})^{-1}$.
As the Borexino electronics is designed for low energetic events, muon plus neutron events can be challenging for it. The light yield of such events can be so high that the buffer in the readout can saturate, making it unavailable for the DAQ system. This leads to a loss in the visible energy in the neutron gate. The corresponding number of boards at the start of the neutron gate is stored in the Echidna files and as they don't deliver any data are called empty boards. This effect is shown in figure 5.5.

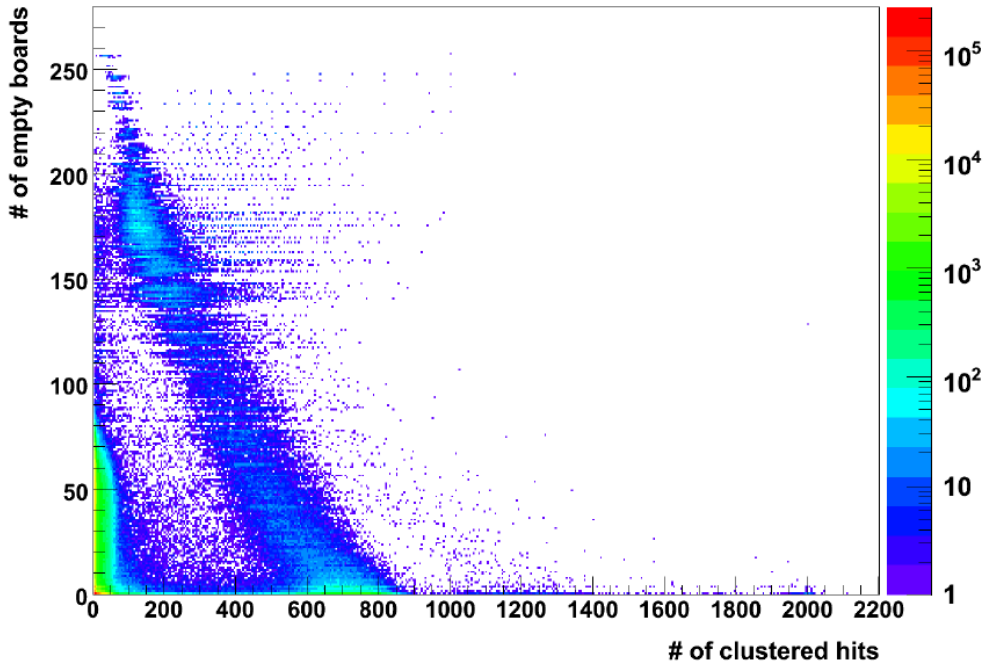

Figure 5.5: Number of empty boards in the Borexino daq i.e. the buffer of the respective board is full versus the number of clustered hits in the neutron trigger gate. With increasing number of empty boards the neutron peak is clearly shifted.

With all boards working the full 700 hits corresponding 2.2 MeV can be detected. The loss in visible energy with rising number of empty boards is clearly visible. The events in the bottom left corner are accidental ^{14}C coincidences. To select only neutron captures, an empty board dependant energy cut (shown in the plot) is introduced. It equals about 1.3 MeV. Neu-

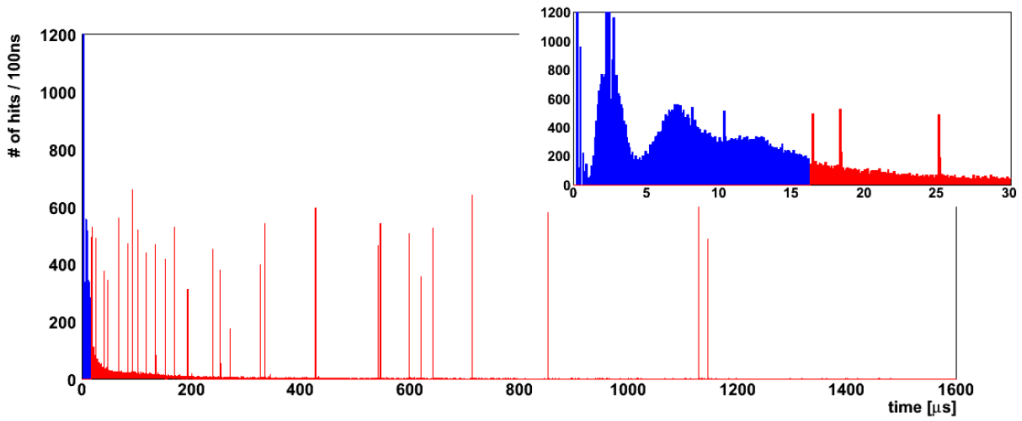

Figure 5.6: Hit time distribution of a muon trigger (blue) and neutron trigger (red). The inset graphic is a closer look at the first 30μs. The peaks are neutron captures [85].

trons thermalise with t with $\tau \simeq 260\mu$s, so to veto them there is a veto after each muon of 2 ms, meaning also after muons crossing just the OD that could create fast neutrons.

5.4 Cosmogenic Radioisotopes

Muons not constitute not only a direct source of background. They also produce cosmogenic radio isotopes via spallation processes on the scintillator's carbon nuclei inside the IV. Subsequently, the Isotopes decay via beta plus/minus decay, generating a background for the various neutrino analyses of Borexino. The isotope's lifetimes vary between tens of milliseconds and go up to about twenty seconds. ^{11}C exceeds this even with a lifetime of 29.3 min but with a Q value of roughly two MeV is just relevant for lower energies. The isotopes can be grouped via their respective lifetime. The different veto strategies for the groups will be presented in the following sections.

Cosmogenic Isotope	τ	Q [MeV]	Decay	Fraction >3 MeV	Measured Rate >3 MeV[cpd/100 t]
^{12}B	0.03 s	13.4	β^-	0.886	$1.62 \pm 0.07_{\text{stat}} \pm 0.06_{\text{syst}}$
^{8}He	0.17 s	10.6	β^-	0.898	$(1.7 \pm 0.5)\times10^{-1}$
^{9}C	0.19 s	16.5	β^+	0.965	
^{9}Li	0.26 s	13.6	β^-	0.932	
^{8}B	1.11 s	18.0	β^+	0.938	$(5.1 \pm 0.7)\times10^{-1}$
^{6}He	1.17 s	3.5	β^-	0.009	
^{8}Li	1.21 s	16.0	β^-	0.875	
^{10}C	27.8 s	3.6	β^+	0.012	$0.52 \pm 0.07(\text{stat})^{0.11}_{0.06}(\text{syst})$
^{11}Be	19.9 s	11.5	β^-	0.902	$(3.6\pm3.5)\times10^{-2}$

Table 5.2: Muon induced background in Borexino with Q value and rate above 3 MeV [95, 31].

5.4.1 Fast Isotopes

Most of the cosmogenic radio isotopes are short-lived with live times shorter than $\sim$1 s. The dominant isotope, as can be seen in table 5.2, is 12B with a lifetime of only $\tau = 0.03$ s. These fast lived isotopes are easily vetoed by looking for a coincidence with a muon. After each internal muon, i.e. mtb, mcr ord idf plus the ID triggered, a veto window of 6.5 s is issued. The spectra of the vetoed events is shown in figure 5.7. The plot shows the rate above 3 MeV after a parenting muon. For a lifetime fit ^{8}He, ^{9}C and ^{9}L are grouped together as the lifetime for these three isotopes is very close to 0.2 s. The same is done for ^{8}B, ^{6}He and ^{8}Li with a lifetime close to 1 s. Three exponentials with a free life time are fitted to the data. The found lifetimes

matches the expected values. The rates are compatible with the ones found in [85]. This shows that the veto is working and that it catches the correct events.
The residual cosmogenic rate after the cut is $\simeq (3.1 \pm 1.5) \cdot 10^{-3}/(\mathrm{d100t})$.

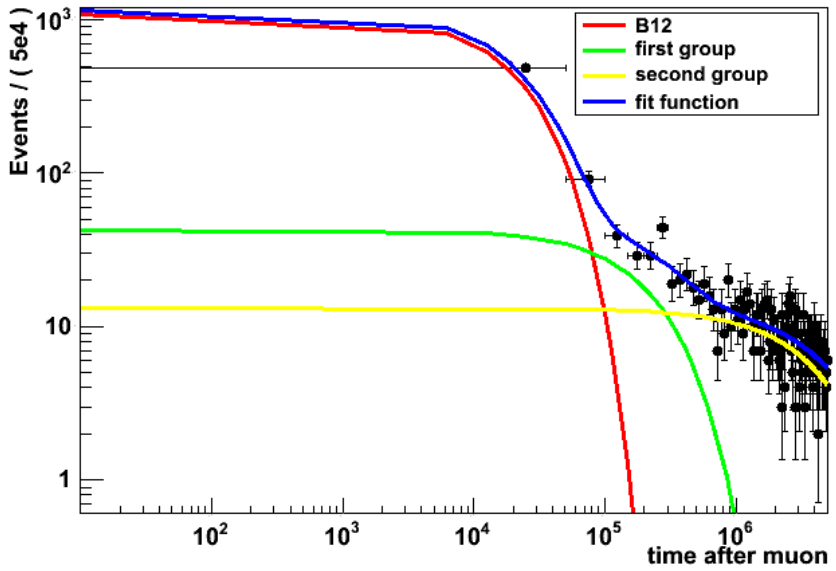

Figure 5.7: Events after a muon trigger. Three exponentials, representing ^{12}B , isotopes with $\tau \approx 0.2\,\mathrm{s}$ and isotopes with $\tau \approx 1\,\mathrm{s}$. The rates match the ones found in citequirin

5.4.2 ^{10}Carbon Veto

The long lived isotpes survive the 6.5 s cut. One of them is ^{10}C (β^+decay, $\tau = 27.8\mathrm{s}, \mathrm{Q} = 3.65\,\mathrm{MeV}$ see figure 5.9), which is usually accompanied by at least one free neutron. The net production is shown in equation (5.1)

$$\mu^{\pm} + ^{12}\mathrm{C} \rightarrow ^{10}\mathrm{C} + 2\mathrm{n} + \mu^{\pm} \tag{5.1}$$

A sufficient veto after each muon would cause a too large dead time. Therefore also the spallation neutrons are used. The ^{10}C decay is expected to be at the same position as the neutron capture, since dispersion is neglect able while the neutron thermalises. So a veto based on a cylinder around the muon track and a sphere around the neutron capture as shown in 5.8 is feasible [59]. However, muons are high energetic events causing lots of

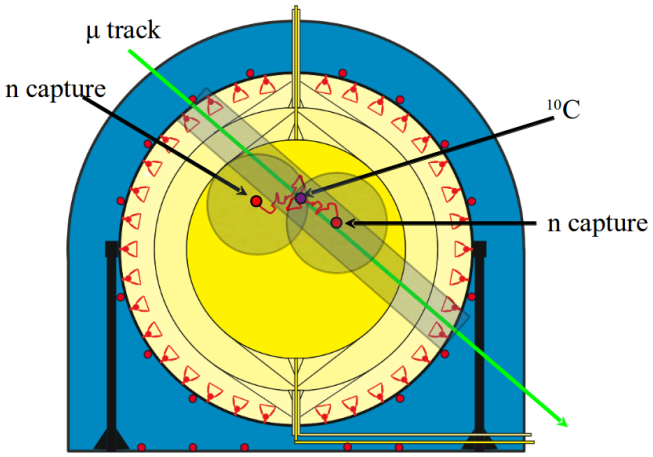

Figure 5.8: Muon in Borexino generating two neutrons plus a ^{10}C isotope.

scintillation light, which can overfill the readout electronics buffer (see section 5.3). Hence, the event reconstruction shortly after a muon can suffer, i.e. also the spatial reconstruction. Therefore, the so called threefold coincidence veto (TFC)[59] between muon, neutron and ^{10}C decay is not used in this analysis. However, the veto in this analysis is still looking for an internal muon with an accompanying neutron, which happens with a rate of $\sim 68\mathrm{d}^{-1}$. After such a coincidence the hole detector is vetoed for 120 to not be reliant on the spatial position of the neutron. Figure 5.10 shows the events after a muon+neutron coincidence. An exponential with free decay time plus a constant is fitted to the data. The decay time converges to the live time of ^{10}C. That shows that the veto catches the desired isotope. Everytime a muon together with a cosmic neutron is detected, the whole detector is vetoed for 120 s, even though the ^{10}C is expected at the same position as the neutron capture, since dispersion is neglect able while the neutron thermalises. However the spatial reconstruction of the neutron capture is very imprecise, since the the previous neutron causes too much noise. With the muon, neutron and ^{10}C decay there are three events, so this technique is called the threefold coincidence [85, 59].

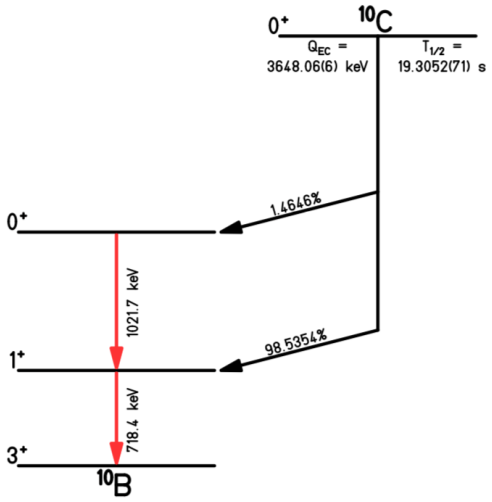

Figure 5.9: ^{10}C decay scheme acoording to [96]

5.4.3 ^{11}Beryllium Veto

Beryllium-11 undergoes a beta decay with a lifetime of $\tau = 19.9\,\mathrm{s}$ and Q=11 MeV . It is created by spallation via the following reaction:

$$^{12}\mathrm{C} + \mathrm{n} \rightarrow ^{11}\mathrm{Be} + 2\mathrm{p} \tag{5.2}$$

It causes a crucial background as the spectral shape and energy regime are very similar to the ^{8}B neutrinos. As it is shown in equation 5.2 there is no free neutron created during the production of ^{11}Be. The mean energy deposited by muons crossing the detector is $\approx$2 MeV/cm [85] as they are close to be minimal ionising. This results in an energy deposit within the IV for a central muon track of $\approx$1.7 GeV. However, muons can also produce showers inside the detector volume. These events lead to a huge energy deposition and can create several new particles. Besides several other there are neutrons and cosmogenic radioisotopes among the created particles. Figure 5.12 shows the neutron created per muon as recorded by the main Borexino daq and the so called Princeton Analog System (PAS). The PAS records the analog sum of all pmt signals which constitutes a reliable and stable secondary system used for cross checks. It is well suited for high energy events, as it is not saturating as the main daq. Further information to the system can be found in [97]. Most of the muons namely $65.9 \pm 0.5\,\%$ are creating only one muon. However half of the neutrons are created in high multiplicity events with multiplicities up to a few hundred neutrons[85].

High multiplicity events are an indicator for shower events and hence for

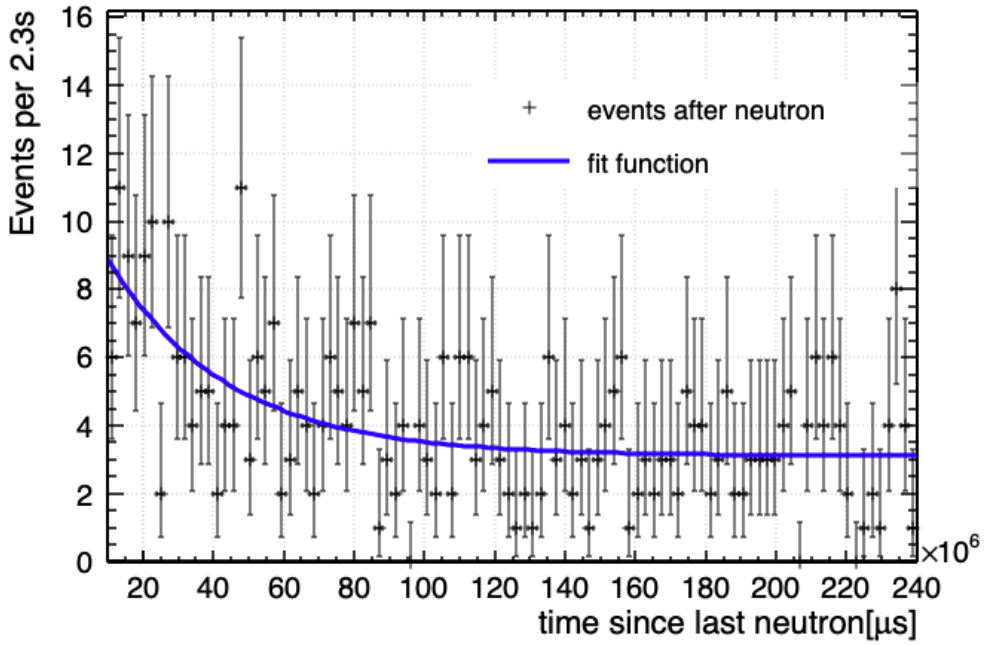

Figure 5.10: Events after muon with accompanying neutron. An exponential fit finds the lifetime of ^{10}C and a rate matching [85]

huge energy deposition in the detector which is accompanied by the formation of radio isotopes. There is a high chance that ^{11}Be is amongst these isotopes. So a neutron created in the detector, despite not directly participating in the production reaction of ^{11}Be, might indicate the presence of a ^{11}Be isotope, as neutrons indicate a high energy deposit. The veto method presented in section 5.4.1 eliminates all shower events as it is issued if already one neutron is detected. Thus parts of the ^{11}Be decays already are eliminated from the data set. The remaining event rate in the data will be calculated in the following.

To analyse the connection of ^{11}Be decays and neutron production, a data set with all internal muon events and all events inside the IV in a time window 150 s after the muon is created. Internal muons are defined as presented in section 5.1. The period where water extraction (described in section 3.3) was performed is excluded. The events after the muon include neutron capture, cosmogenic radioisotopes und uncorrelated events i.e. neutrino events, beta decays etc. For each muon the time difference to the following events is calculated. This implies that events can be factored in more than once which has to be considered when calculating a rate. To remove uncorrelated events

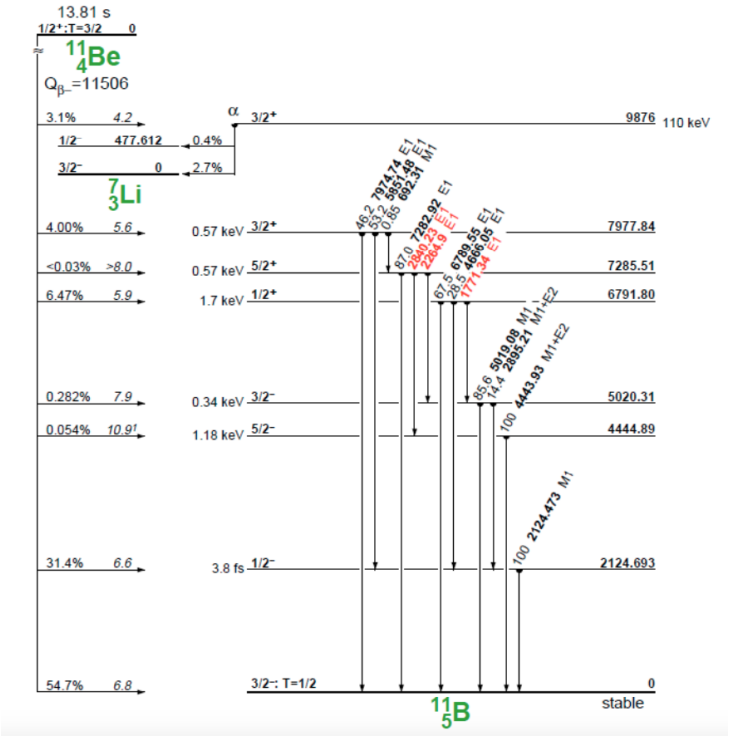

Figure 5.11: ^{11}Be decay sheme from [98]

with ^{208}Tl which decays via beta decay and a q value of Q=5 MeV an energy cut 6 MeV is applied to the data set, with an upper limit of 12 MeV. This also excludes ^{10}C (Q=3.6 MeV) decays where a neutron capture is expected. The event rate after a muon is dominated by the fast lived ^{12}B that undergoes a beta decay with $\tau = 0.003$ s and Q=13.4 MeV. To remove it from the dataset only a time window of 10 s to 150 s after a muon is analysed. That also removes two groups of isotopes, one with a lifetime of around $\tau \approx 0.2$ s, namely ^{8}He, ^{6}C and ^{8}Li, the second one with a lifetime of $\tau \approx 1$ s, namely ^{9}He and ^{8}Li. In the remaining dataset ^{11}Be is the sole cosmogenic radio isotope with a correlation to the muon.

Figure 5.13 shows the time difference of an event to the parent muon, on the left there was no neutron detected after the muon on the right at least one neutron was detected. In the case that at least one neutron was detected, an exponential decay is clearly visible. If no neutron was detected, the distribution is flat and no time dependance is visible.
Figure 5.14 presents the accompanying spectra to figure 5.13. Both spectra show no sign of an unforeseen contribution. The statistics unfortunately is

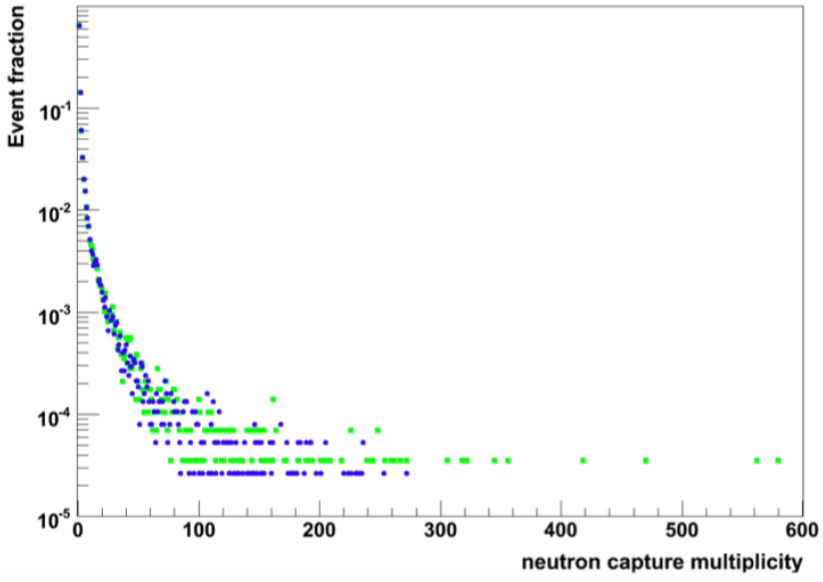

Figure 5.12: Neutrons produced per muon as detected by the main borexino daq (blue markers) and the Princeton Analog System(green markers)[85]

not high enough to perform a spectral fit.
Both distributions shown in figure 5.13 were fitted with equation 5.3. In a first step τ was left as a free parameter. For the case a neutron was present $\tau = (14.8 \pm 6.6)\,\mathrm{s}$ is found, which is compatible with the lifetime $\tau = 19.9\,\mathrm{s}$ of ^{11}Be. On the other hand, for the case where no neutron is present there is no exponential decay found and τ is compatible with zero. To test this statement toy Monte Carlo study was performed to determine how many ^{11}Be events can be hidden in the data until τ differs from zero. Random events from an exponential with the decay time of ^{11}Be plus random events from a flat distribution were fitted with equation 5.3. The number of events taken from the exponential was increased until the fit found a decay time diverging from zero. The sum of events was kept constant to match the number in figure 5.14. Unfortunately, just above 1000 events the fit found a lifetime different from zero. That number exceeds by far the expected rate of $\mathrm{R}\left(^{11}\mathrm{Be}\right) < 0.20\,(\mathrm{d100\,t})^{-1}$ [85]. Hence, the statement that there is no exponential decay for the case that there was no neutron cannot be trusted. That implies that just with Borexino data it is not possible to specify the ^{11}Be decay rate.

$$\mathrm{a} * \mathrm{e}^{\frac{-\mathrm{x}}{\tau}+\mathrm{b}}. \tag{5.3}$$

To check if the exponential decay in the neutron case is created by accidental events, the time window after the muon is shifted by 150 s. So events

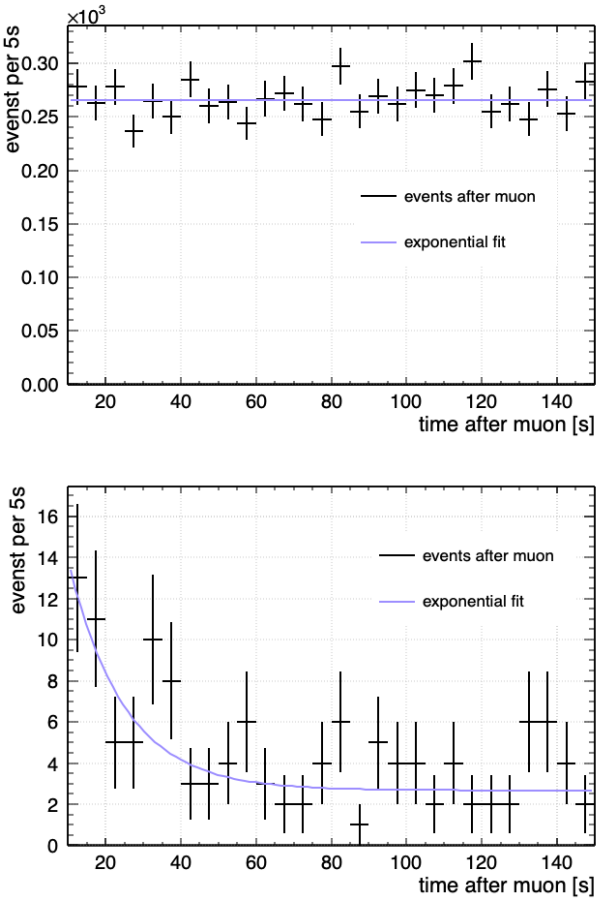

Figure 5.13: Time distribution of events after a muon crossing Borexino. *top*: with a neutron accompanying the muon *bottom*: without accompanying neutron. An exponential fir finds the lifetime of ^{11}Be.

150 s to 300 s after the muon are recorded. In that time window all cosmogenic radioisotopes created by muons are decayed, as the lifetimes in table 5.2 suggest. Hence, there are no events in that time window caused by a parenting muon, meaning a flat spectrum is expected. Figure 5.15 shows the spectra for the muon with and without neutron case. Both spectra are flat as expected and show no correlation to the parenting muon. For both cases the rate is consistent with flat parts of the previous spectra. To extract an ^{11}Be rate the lifetime in equation 5.3 is fixed to the ^{11}Be lifetime and fitted to the data. The result is shown in figure 5.16. For the case with no accompanying neutron, there is again no exponential component found. On the other hand for the muon plus neutron case 22 events are found. That number has to be adjusted, as it is possible that events are counted twice. If

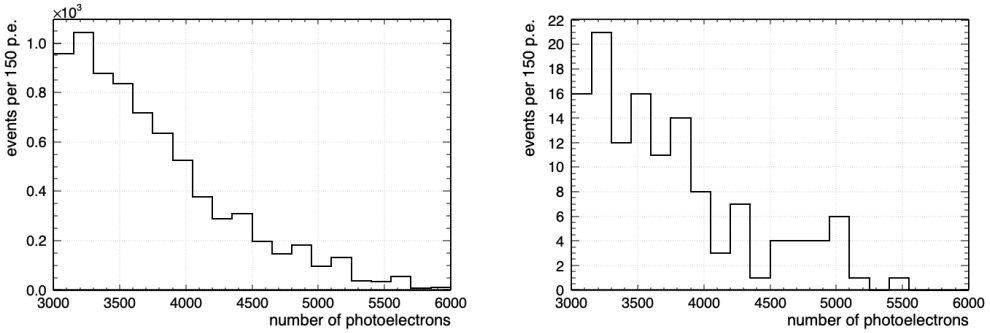

Figure 5.14: Spectrum of ^{11}Be candidates after muon events *left:* no coincident neutron *right:* at least one coincident neutron.

two muons occur in the time window of 150 s before the event, it will appear twice. That occurred six times for 123 muons creating an event and thus 129 events fulfilling all criteria.
However in [95] it is shown that it is possible to extrapolate radioisotope rates from the KAMLAND experiment with the following formula:

$$\mathrm{R}_{\mathrm{Borexino}}(^{11}\mathrm{Be}) = \mathrm{R}_{\mathrm{Kamland}}(^{11}\mathrm{Be}) \left(\frac{\langle \mathrm{E}_{\mu\text{–Borexino}} \rangle}{\langle \mathrm{E}_{\mu\text{–Kamland}} \rangle} \right)^{\alpha} \frac{\phi_{\mathrm{Borexino}}}{\phi_{\mathrm{Kamland}}} \qquad (5.4)$$

with the mean muon energy and flux of Borexino $\langle \mathrm{E}_{\mu\text{–Borexino}} \rangle = 283 \pm 19\,\mathrm{GeV}$ and $\phi_{\mathrm{Borexino}} = (3.432 \pm 0.001) \cdot 10^{-4}\mathrm{m}^{-2}\mathrm{s}^{-1}$[94], the mean muon energy and flux of Kamland $\langle \mathrm{E}_{\mu\text{–Kamland}} \rangle = (260 \pm 4)$ GeV and $\phi_{\mathrm{Kamland}} = (1.49 \pm 0.11) \cdot 10^{-3}\mathrm{m}^{-2}\mathrm{s}^{-1}$ [99] and a scaling factor α that relates isotope production for different muon energies which was measured in [100]. That results in a total expected ^{11}Be rate in Borexino of $(3.2 \pm 0.6) \cdot 10^{-3}$ cpd/100 t. Part of this rate now is contained within the 120 s time window. If one subtracts that rate, a remaining rate of $(3.2 \pm 0.6) \cdot 10^{-3}$ cpd/100 t of ^{11}Be decays after cuts is expected.

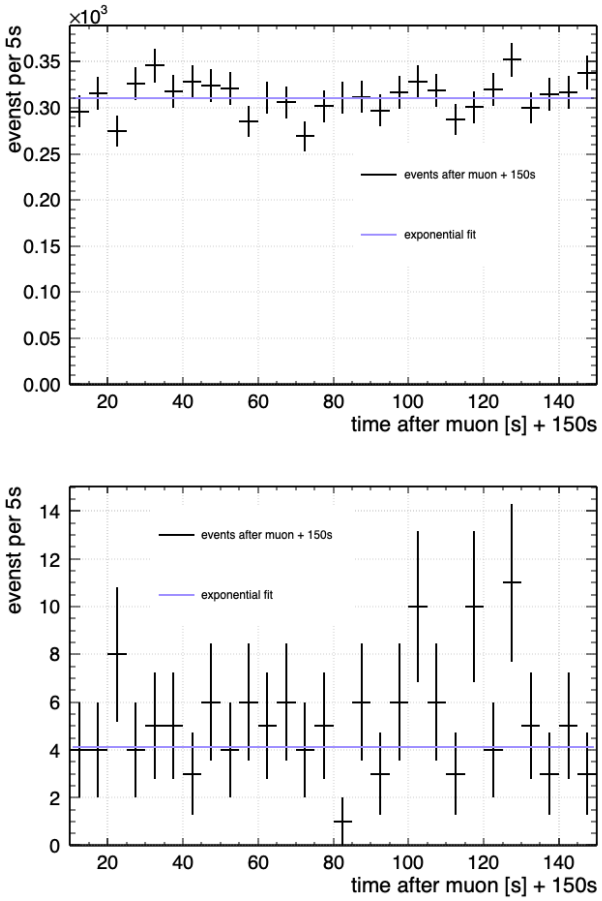

Figure 5.15: Time window shifted to 150 s after a muon event. No correlation to the muon is expected. Exponential fit to muon with *top*: no coincident neutron *bottom*: at least one coincident neutron.

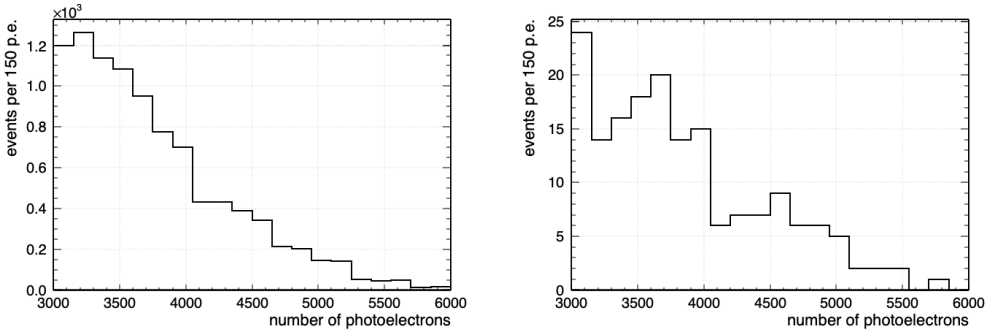

Figure 5.16: Spectrum of events 150 s after a muon with *left:* no coincident neutron *right:* at least one coincident neutron.

Chapter 6

Counting Analysis above 3MeV

In this chapter a counting analysis of the solar ^{8}B neutrino above 3 MeV is presented is presented. In Borexino these neutrinos are detected via elastic scattering described in section 3. Combined with the ^{7}Be measurement, the vacuum and the matter dominated regime of the MSW-LMA solution are measured with the same detector setup.

6.1 Fiducial Volume Cut

As shown in section 4.2 the outer components of the detector constitute a source for gamma background. Despite the buffer's shielding capabilities the gammas penetrate the IV. As the gamma rate decreases exponentially a radial cut of 3 m resulting in a fiducial volume (FV) of 99.5 t is very effective against this background. To define the FV it is possible to place the ^{241}Am^{9}Be at x$\pm$3, y$\pm$3 and z$\pm$3. The position is checked via a CCD system [90]. The neutron-proton-scattering permits to calibrate the reconstructed position as function of the collected energy up to about 10 MeV.

Figure (6.1) shows the calibration result with R_{rec} the reconstructed radius and R_{nom} the nominal radius determined by the CCD system. A non spherical distribution of live pmts, especially a lack of live pmts in the lower part of the ID, is responsible for the asymmetric FV.
Despite the 3 MeV threshold and the FV there is still an external gamma contamination. Figure 6.2 shows the radial distribution of events above 3 MeV. There are three types of events events in this data: uniformly distributed events i.e. neutrinos, cosmics and internal background, external events i.e. gammas that decrease exponentially and surface events caused by the inner vessel approximated with a gaussian. All three distributions are convoluted

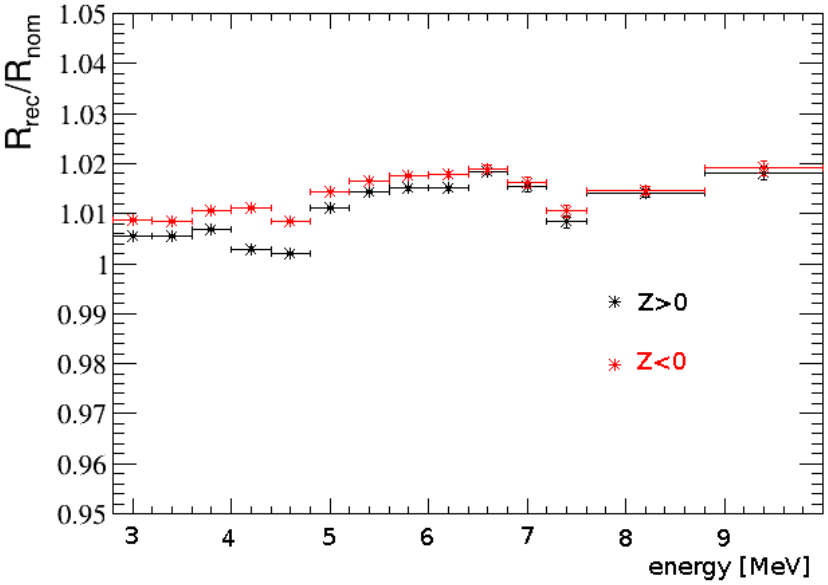

Figure 6.1: Ratio of the reconstructed radius R_{rec} and the nominal radius R_{nom} against collected charge.

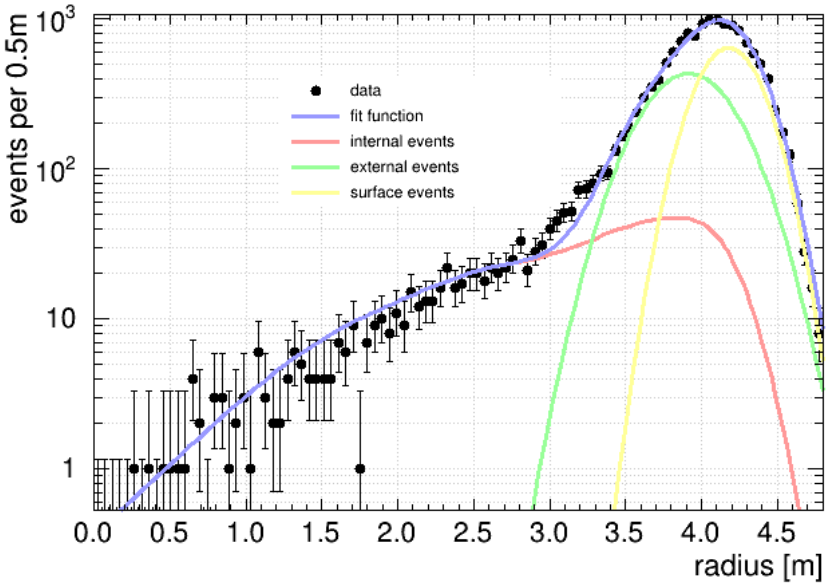

Figure 6.2: Fit of radial distribution of events >3 MeV. The red line represents uniformly distributed events within the active Volume, the green line external background and the yellow line surface contamination of the IV.

	events	rate [cpd/100 t]
all events	548±23	0.29±0.01
^{208}Tl	50.7±7.1	0.016±0.002
^{11}Be	8.1±10.8	0.006±0.008
other cosmogenics	6.3±3.1	0.003±0.002
external	6.8±0.6	0.005
^{8}B-neutrinos	484±24	0.24±0.01

Table 6.1: Event rates within a fiducial volume of 3m

with the detector response function and fit to the data set. The fit results in a remaining gamma rate of $(4.3 \pm 0.3) \cdot 10^{-3}$/(d100t).

6.2 ^{8}B Spectrum within 3 m

Table 6.1 lists the remaining events within 3 m. From the cosmogenic background the long lived ^{11}Be remains (section 5), from the internal background the untagable ^{208}Tl beta decays (section 4.1.1) and a small amount of external events (section 4.2). If one subtracts the background events, the remaining events are the ^{8}B neutrino events. This results in 484±24 neutrino events corresponding to a rate of 0.24±0.01. The rate matches the solar standard model MSW-LMA solution [101, 25].
The spectral distribution of table 6.1 is shown in figure 6.3. All background events except some ^{11}Be events are located in the first energy bin. Figure 6.3 shows the spectral distribution. Most of the background is low energetic with the high energetic ^{11}Be being the exception. Figure 6.3 Most of the background is located in the first energy bins, so the uncertainties there are higher compared to the high energy bins.

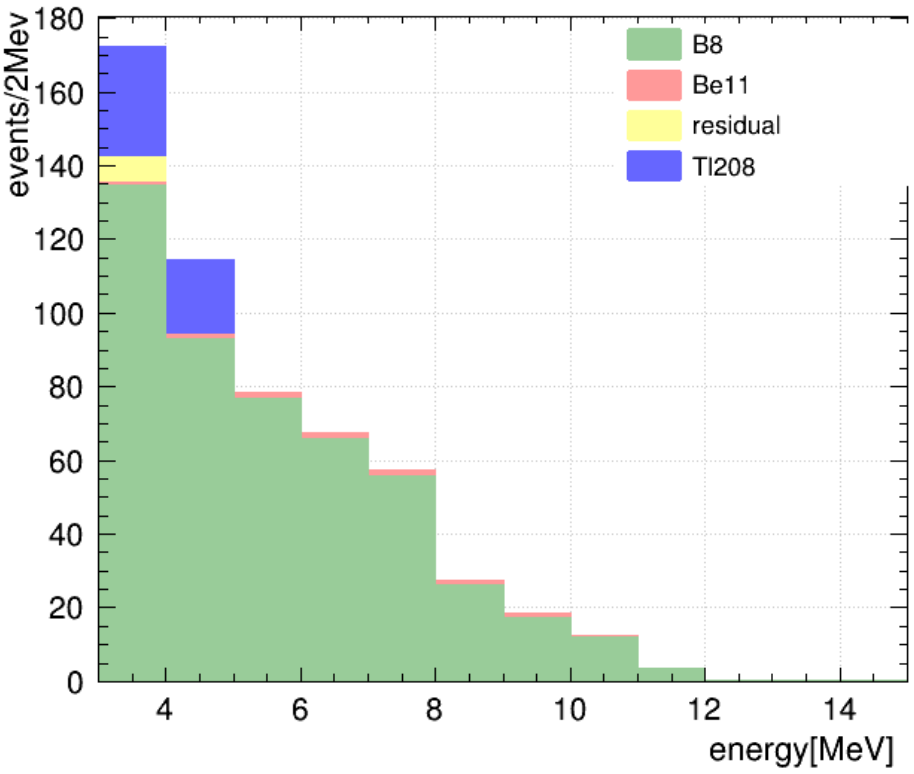

Figure 6.3: The black dots represent the final events after all cuts, internal ^{208}Tl is marked blue, cosmogenic ^{11}Be teal and external background red shaded. Results are also shown in table 6.1.

Chapter 7

Analysis with the full Detector Mass

Within a fiducial volume of 3 m the ^{8}B-neutrino spectrum is can be extracted by subtracting the backgrounds statistically. If one expands the fiducial volume, there are new background sources like the IV and buffer. It is possible to disentangle the different contributions to the final spectrum via a two dimensional fit, utilising the radial and spectral distribution at the same time. This technique is described in the following sections.

7.1 Spectra Simulation

To study the detector the Borexino Collaboration developed a detailed Monte Carlo simulation based on Geant4 [102]. With the help of several laboratory measurements and calibration campaigns as input [90] it reached a high accuracy in reproducing physics events.
The user can choose between several spatial and spectral distribution for the particle generation. Also, it is possible to choose the detector geometry as it is not constant over time. In 2009 a leak occurred in the inner vessel (IV) (see section 2.1.1), which allowed scintillator to flow in buffer region. That causes a deviation from the spherical shape of the IV. The density of the two volumes was adjusted and scintillator was added. Therefore, the IV shape varies over time. The shape is monitored with a weekly update which can be imported to the monte carlo. Also, the photomultiplier tubes (pmts) are slowly dying over time. The number of life channels is monitored for each 6 h run, which can also be imported to the monte carlo. The physics processes are then handled by the G4Bx package[102], which contains the detector

geometry and material properties. Within the material properties, there is also the light emission mechanism of the different media. A particle that deposits energy in one of the detector volumes creates the proper amount of scintillation and Čherenkov light. The monte carlo tracks each of these photons considering optical interactions i.e. refraction, reflection, absorption, reemission and scattering. The photons are tracked until they a pmt cathode or are absorbed without reemission. After the cathode the electronics simulation takes over. It simulates each pmt with its own properties e.g. time spread, dark noise, after pulses, resolution etc. Afterwards the whole electronic chain is modelled i.e. trigger, charge integration etc. The output is identical two the detectors real taken raw data. This output is handled by the offline reconstruction software. In addition to the reconstructed values, the true input parameters are saved. Besides this the simulation output is the same as the real detector's output.
The Monte Carlo is used to generate radial and spectral probability density functions (pdfs) for the signal and background components. For each run the detector conditions i.e. live channels, IV shape, noise etc are loaded. The simulated events under this conditions are then scaled to the real run time, so that each run is percental correct represented in the monte carlo data set. The simulated radial and spectral distributions are converted to pdfs using the roofit toolkit [103] . An example for ^{8}B neutrinos is shown in figure 7.1

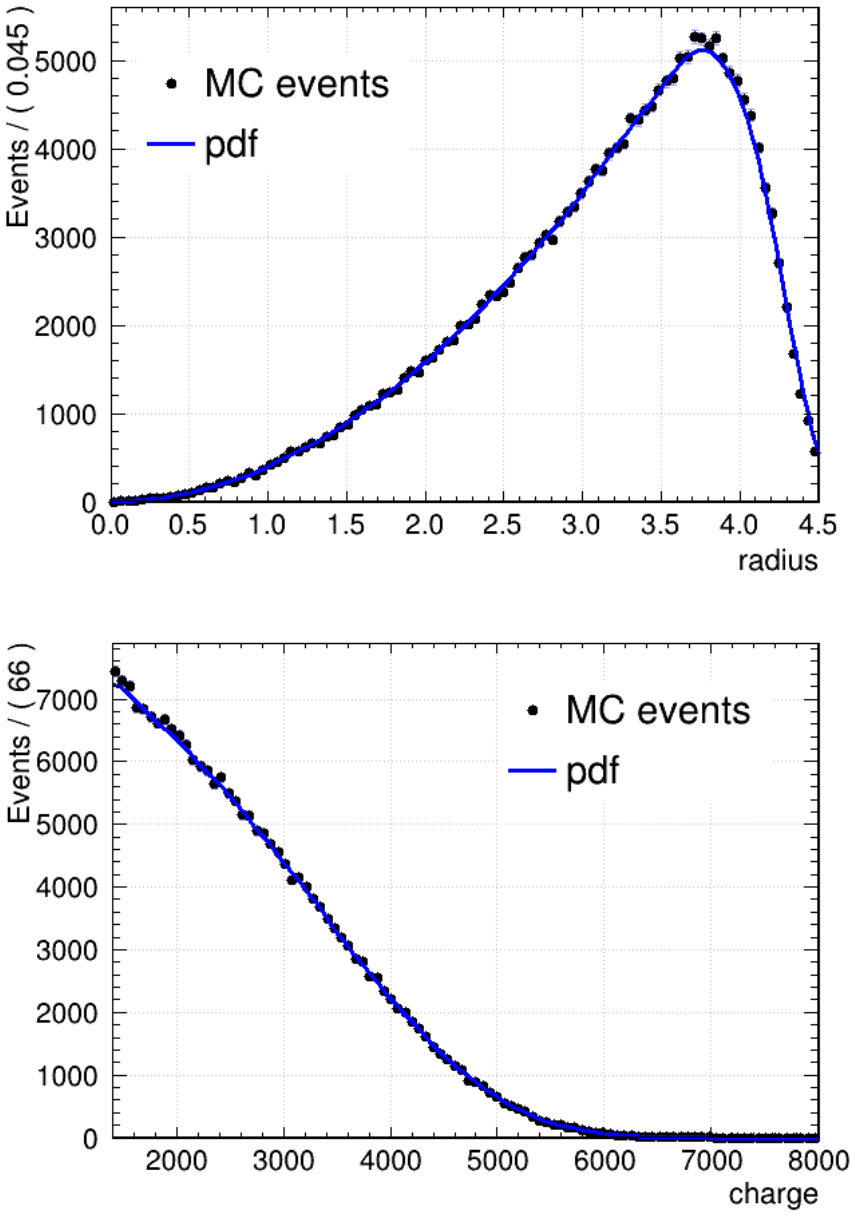

Figure 7.1: *Top*: simulated radial ^{8}B-neutrino distribution plus probability density function (pdf) created from the data *Right*: spectral ^{8}B-neutrino distribution plus probability density function (pdf) created from the data, energy observable is detected charge with 500 charge $\simeq$1MeV.

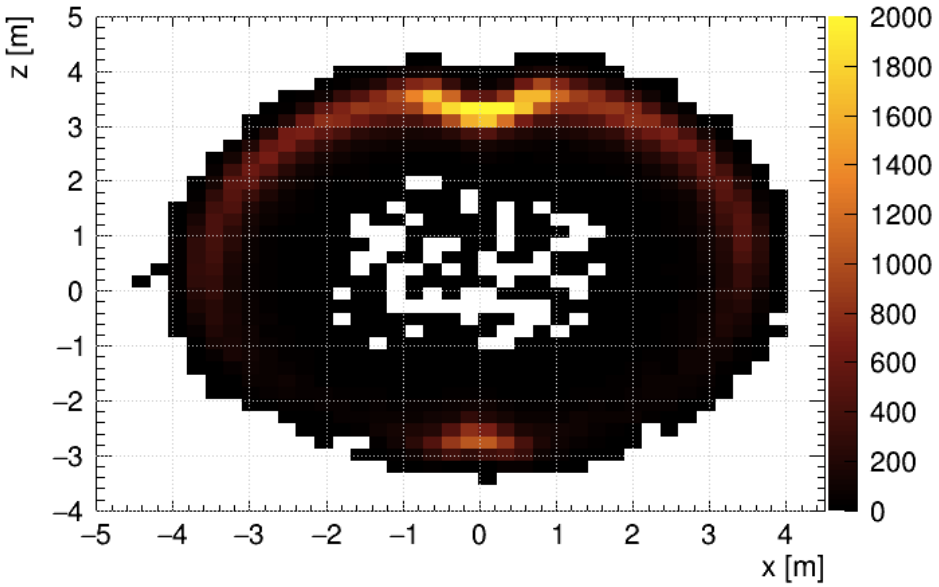

Figure 7.2: poles

7.2 Pole Background

Figure 7.3 shows a picture taken by the CCD system. It shows the two vessels surrounded by the pmts. In the pictures center and top the mounting structure ,that holds the vessels in place and enforces their spherical shape, is visible. The mountings represents the closest solid material to the sensitive volume. It is made out of metal and therefore contains isotopes from the ^{238}U and ^{232}Th decay chains and therefore emits the gamma radiation described in section 4.2. Figure 7.2 shows a slice of the x-z-plane with 20cm thickness of all events after cuts. The hotspots at the top and bottom are clearly visible. It was not possible to match this distribution around the mounting structure with monte carlo data. Therefore a sphere with 1 m radius around the mounting structure is excluded from the analysis.

7.3 Background Sources

Using the hole IV volume introduces new background sources. Before integration the IV contamination was tested to be < 1.7 ppt for the ^{238}U chain[104]. Compared to the liquids a purification after the completion of the detector is not possible. Hence, close to the IV there is the highest rate within the detector. Above 3 MeV the ^{208}Tl beta decay decay presents the

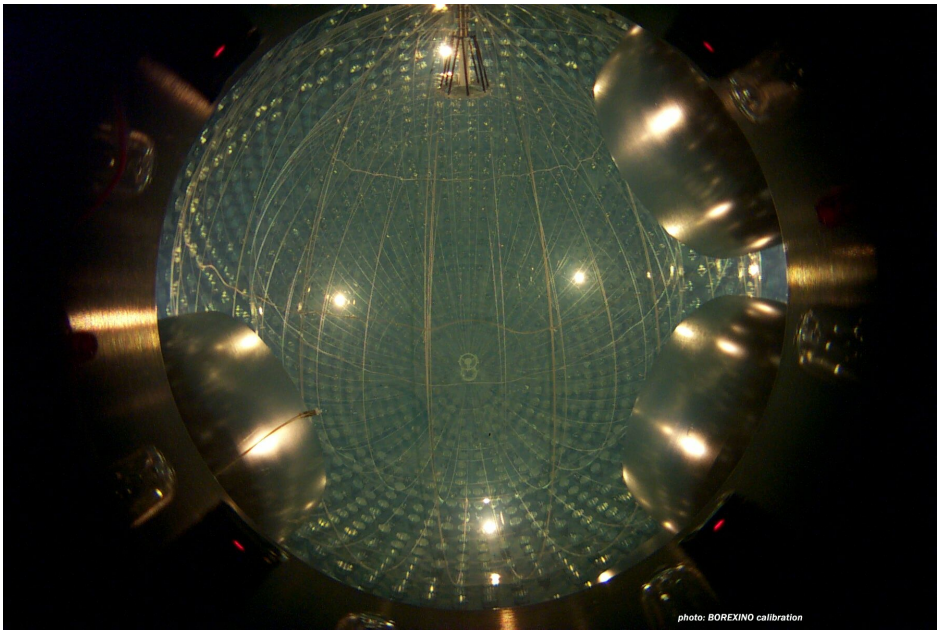

Figure 7.3: picture vessel

biggest source of background. Electrons from that decay deposit their energy within centimeters, hence the vessel should almost look pointlike. However, the vessel shape is not constant over time, due to the leak. This broadens also the background distribution. Alpha decays that occur on the vessel are quenched below 3 MeV. Beyond the vessel comes the buffer. Compared to the scintillator inside the IV the liquids here were not purified after filling. Hence, the radiopurity levels are lower. The buffer liquid outside the 5.5 m vessel is also in contact with the SSS and the pmts which emanate radon. Therefore the radiopurity is further decreased. Within the buffer ^{208}Tl decays and emits 2.6 MeV gammas which can reach the inside of the IV. Also the gammas created on the SSS and pmts reach are very relevant close to the IV. They consist of gammas from ^{208}Tl decay, ^{214}Bi decay and neutron capture(see section4.2).

7.4 Results for IV

The following contributions are still in the data:

- solar ^{8}B neutrinos
- internal ^{208}Tl decay
- cosmogenic ^{11}Be decay
- ^{208}Tl decay on the IV
- External gammas produced by^{208}Tl decay & ^{214}Bi decay
- external gammas produced by alpha-n-reactions

For each a pdf as described beforehand is created. The pdfs are fitted to the raw data using the extended likelihood fit provided by the roofit package [103]. The internal ^{208}Tl, cosmogenic ^{11}Be and external gammas caused by α-n reactions rate are constrained with a gaussian pull term with mean and width as presented in section 4 and 5, respectively. Figure 7.4,7.5 and 7.6. The individual contributions are listed in table 7.1. The ^{8}B rate matches the prediction by the MSW LMA solution. The external gamma rays constitute the largest background. This is due to Borexino's rather small size and therefore limited self shielding capabilities. Despite the careful material selection [104], the IV is second largest source of background. This is due that for nylon there are not as effective purification methods as for scintillators [66]. Besides the internal ^{208}Tl and cosmogenic ^{11}Be the backgrounds are dominantly located at larger radii. This shows the great prospects of future larger detector, where these backgrounds can be neglected due to the enhanced self shielding.

	events
^{208}Tl gammas	2816 ± 216
^{214}Bi gammas	7408 ± 506
^{209}Tl IV	1433 ± 35
neutron capture	550 ± 70
^{11}Be	18.9 ± 27.8
internal ^{208}Tl	154 ± 10
^{8}B-neutrino	1376 ± 70
^{8}B-neutrino [cpd/100t]	0.24 ± 0.01

Table 7.1: Results from a two dimensional extended likelihood fit within the IV.

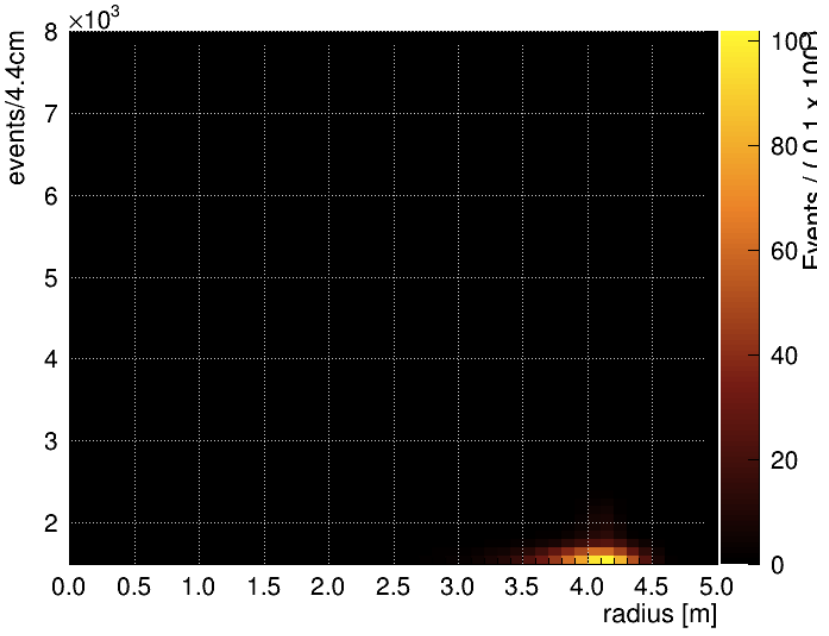

Figure 7.4: Radial and spectral distribution in the dataset

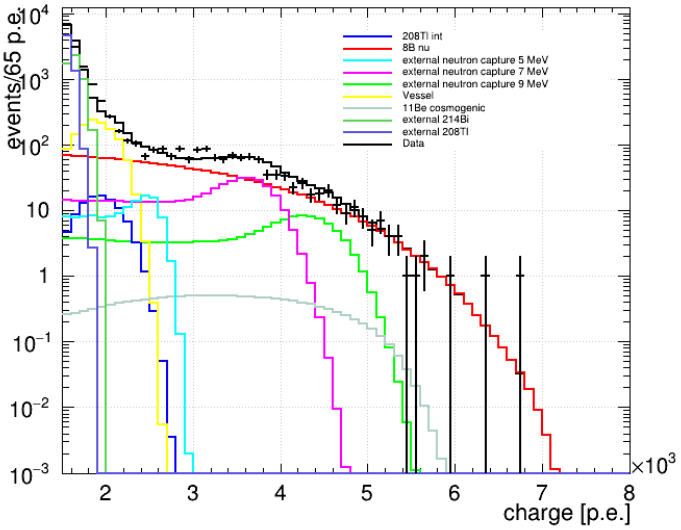

Figure 7.5: spectral distribution of ^{8}B neutrino events within the IV obtained by an extended likelihood fit described in section 7.4.

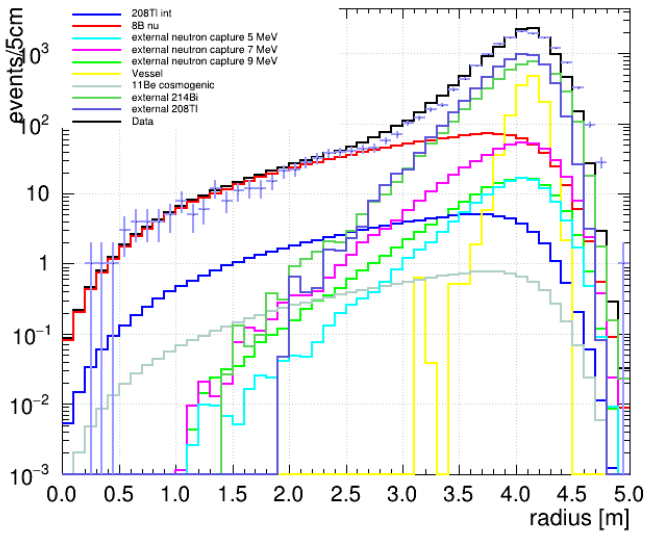

Figure 7.6: spectral distribution of ^{8}B neutrino events within the IV obtained by an extended likelihood fit described in section 7.4.

Chapter 8

Searching for Sterile Neutrinos using the ^{8}B Spectrum

8.1 Simulation of Sterile Spectra

The solar neutrino generator was developed to simulate elastic scattering interactions of all different solar neutrino components such as pp, ^{7}Be, ^{8}B, pep and CNO neutrinos. The neutrino spectra are based on [105, 106] . The kinetic energy of the electrons is randomly extracted according to the differential cross-section which includes first order radiative corrections[107]. The oscillation probability of the electron neutrinos is calculated according to the LMA-MSW prediction[26]. Sterile neutrinos, as introduced in section 1.7 would change the oscillation. They can move the so called "up-turn" to lower energies. A derivation of the survival probability is given in [108]. Figure 8.2 shows an example for a modified survival probability. The calculation assumes the (3+1) model with neutrino flavors $\nu_{\mathrm{f}} = (\nu_{\mathrm{s}}, \nu_{\mathrm{e}}, \nu_{\mu}, \nu_{\tau})$ mixed in the mass eigenstes ν_{i}, i $= 0, 1, 2, 3$. The mixing angle α denotes the mixing between 0 and 1 and the ratio of the mass squared differences $\Delta\mathrm{R} = \Delta\mathrm{m}^2_{01}/\Delta\mathrm{m}^2_{21}$. The generator was then modified to enable custom survival probabilities such as in [108] [109]. Figure 8.1 shows an example for the difference in the spectrum that is caused by a change in the survival probability. Various ^{8}B spectra with different survival have been simulated with the same method as shown in section 7.1, i.e. for each used run in the data its length and detector conditions are taken into account. Examples of survival probabilities that are used are shown in figure 8.2.

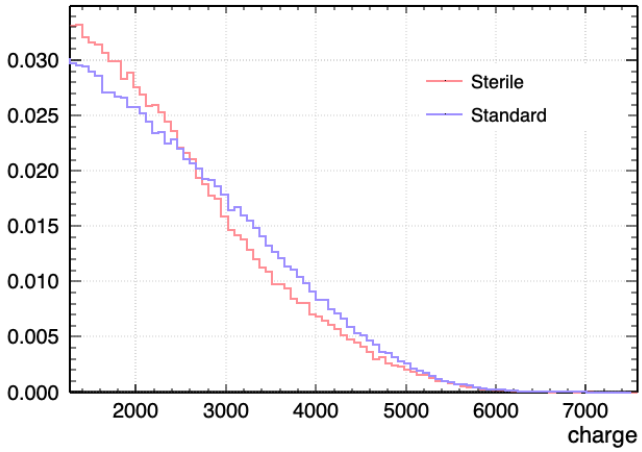

Figure 8.1: Comparison of simulated ^{8}B neutrino spectra, once with standard survival probability once a sterile neutrino with $\Delta R = 0.08$ and$\sin^2 2\alpha = 5 \cdot 10^{-3}$

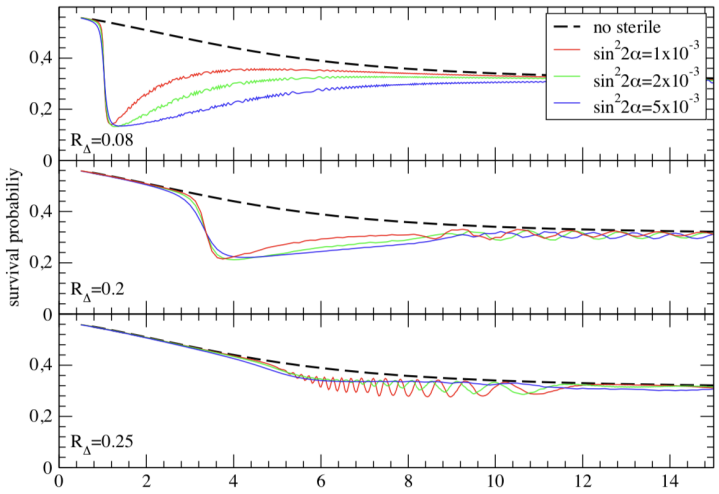

Figure 8.2: Survival probability including sterile neutrinos, with $\Delta R = \Delta m^2_{01}/\Delta m^2_{21}$. Sterile neutrinos move the so called "up-turn" to lower energies. [108]

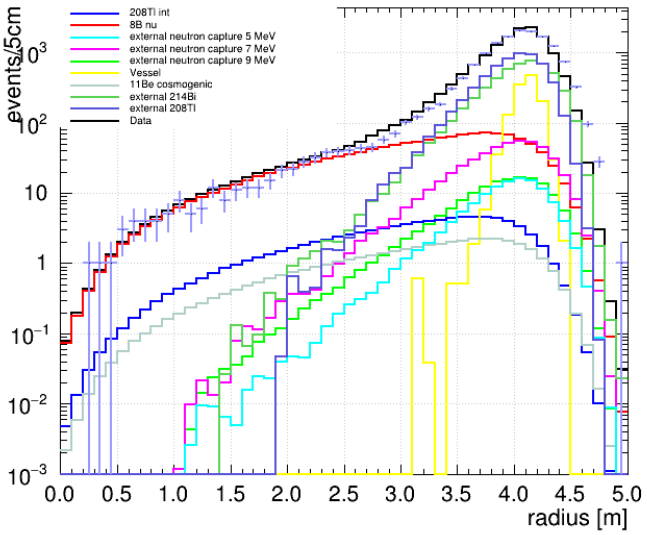

Figure 8.3: Radial distribution with modified survival probability according to [108] with with $\Delta R = 0.08$ and$\sin^2 2\alpha = 5 \cdot 10^{-3}$

8.2 Analysis Method & Results

The modified spectra are fitted to the data as shown in section 7.4. The models are compared via their fit's likelihood. One example for the radial and spectral distribution is shown in figure 8.3 and 8.4. table 8.1 sums up the results.

Δ R	$\sin^2 2\alpha$	excluded with c.l. in%
0.08	$5{\cdot}10^{-3}$	53
1.3	$5{\cdot}10^{-4}$	48
1.5	$5{\cdot}10^{-4}$	52

Table 8.1: Sterile neutrino parameter with respective exclusion power

The change in the survival probability causes the largest difference at lower energies. Therefore this analysis is limited the 3 MeV energy threshold. The threshold is given by the external gamma rays. Borexino's self shielding is not sufficient to suppress them. Borexino's size is not large enough to use a fiducial volume that enables a lower threshold.

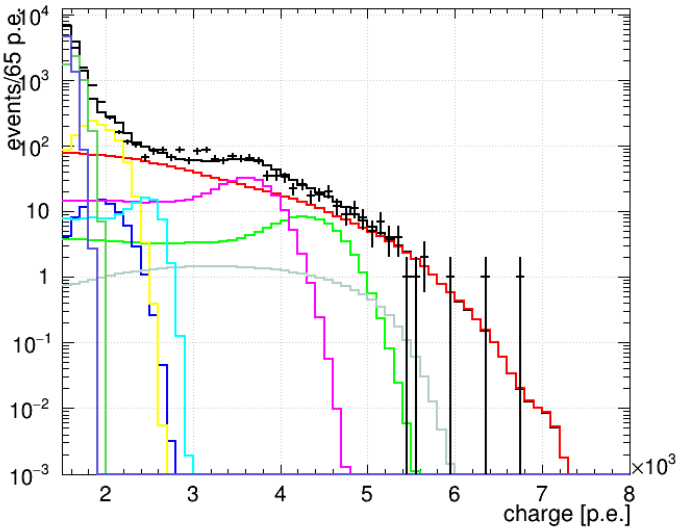

Figure 8.4: Spectral distribution with modified survival probability according to [108] with with $\Delta R = 0.08$ and$\sin^2 2\alpha = 5 \cdot 10^{-3}$

Chapter 9

Prospects

Several next generation neutrino detectors like Theia [110], Dune [111] and Juno [112] are planed or under construction. They will deepen the understanding of solar neutrinos. The capabilities of Juno will be presented in this chapter.

9.1 Juno Detector

subsectionThe Jiangmen Underground Neutrino Observatory The Jiangmen Underground Neutrino Observatory (JUNO) is a multi purpose liquid scintillator neutrino experiment, that is currently under construction [112]. Its main goal is to detect antineutrinos created in nearby nuclear power plants. Therefore a 20 kt fiducial mass and an unmatched energy resolution of 3%/MeV is planned.
The experiment is located in Jinji town in the Jiangmen province in China. In ∼53 km distance of the site there is the Yangjiang nuclear power plant (NPP) and the Taishan NPP. IN Yiangjiang there are six reactor cores with 2.9 GW each and in Taishan there are two cores with 4.59 GW each, resulting in a total power of 26.55 GW. Furthermore in ∼200 km are the Daya Bay and Huizhou reactor which contribute ∼3% to the anti neutrino flux. To shield the experiment from cosmic radiation a new underground laboratory is built. It is covered by 650 m of rock, corresponding to ∼1700 m.w.e., resulting in a muon rate in the central detector of 3.5 Hz with a mean energy of 215 GeV [113].
The central detector is submerged in a water pool to shield from natural radiation in the rock and fast neutrons. The tank is equipped with 2000 20" PMTs to detect Čerenkov light and act as an active muon veto and tracker. A segment of the pool is covered with the Opera muon tracker [114]

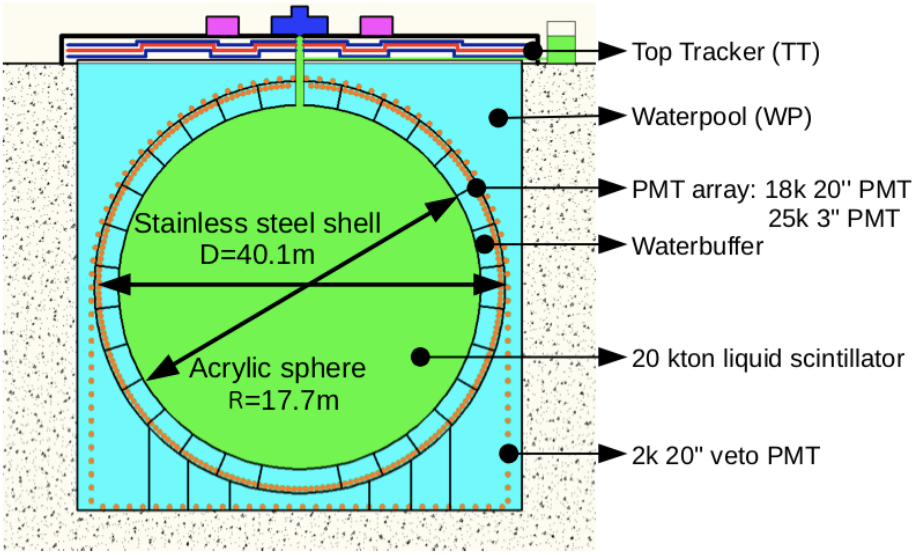

Figure 9.1: Schematic cross section of the Juno detector. The active volume is submerged in a water pool that is equipped with 2000 pmts to detect muons. The scintillator is encapsulated by an acrylic vessel with a radius of 17.7 m. The light is 18000 20änd 25000 3p̈mts that are mounted on a steel scaffolding.

to provide a high precision data set to calibrate muon tracks. The 20 kt liquid scintillator are contained in a spherical acrylic vessel with 17.7 m radius and a thickness of 12 cm. Linear alkylbenzene (LAB) serves as solvent in the LS.Furthermore, the LS consists of 3 g/l 2,5-diphenyloxazole (PPO) as the flour and 15 mg/l p-bis-(o-methylstyryl)-benzene (bis-MSB) as the wavelength shifter. The goal for the attenuation length is a value greater than 20 m and for the light yield 1200 photons/MeV. The light emitted by the LS is detected by 18.000 20" PMTs. For a better timing information they are complemented by 25.000 3" PMTs. The PMTs are mounted on a stainless steel scaffolding that surrounds the acrylics. The optical coverage is 77.5%. A scheme of the setup taken from [113] is shown in figure 9.1.
The main goal of the experiment is to figure out the mass hierarchy. Therefore it will detect the reactor $\bar{\nu}_e$ via the so called inverse beta decay:

$$\bar{\nu}_e + p \rightarrow e^+ + n \tag{9.1}$$

The positron will annihilate immediately with an electron and provide a prompt signal. The neutron thermalises within 250 μ s and gets captured on a hydrogen atom, releasing a 2.2 MeV gamma. This coincidence allows to greatly suppress the background rate. In the survival probability of the

detected $\bar{\nu}_e$ there is a phase term which is positive for normal hierarchy (NH) and negative for inverted hierarchy (IH). Due to its high light yield JUNO will be able to resolve this change in the oscillation phase. A more profound explanation is given in [112]. The JUNO detector will also be able to detect solar neutrinos via elastic scattering on electrons. For the low energetic part of the solar neutrino spectrum the internal background is crucial, while cosmogenic radioisotopes created by muons are neglect able. For the higher energetic ^{8}B neutrinos it is vice versa.[112]. For the minimal radiopurity requirements, similar as in the KamLAND solar phase [115], only a ^{7}Be neutrino measurement will be feasible, with a signal to background ratio of 1:3. However, it will be still challenging as a precise knowledge of the ^{210}Bi background is needed, which covers the full spectral range of the ^{7}Be neutrinos. Furthermore, the ^{210}Pb, ^{85}Kr, ^{238}U and ^{40}K have to be handled. If the ideal purity, corresponding Borexino Phase-I [10] levels, can be reached, also a measurement of CNO neutrinos maybe feasible. JUNO's energy resolution broadens the window between the endpoint of the ^{7}Be shoulder and the starting of the ^{11}C spectrum compared to Borexino [116, 68]. In this region the signal to background ratio is the most favorable for a CNO measurement, which may allow JUNO to determine the CNO rate. A pp neutrino measurement will be very challenging due to the overwhelming ^{14}C background. It creates pile up events that dominate the energy region of pp neutrinos [116]. Only a reduction of the pile up rate through a waveform analysis or a scintillator with a low ^{14}C rate would allow a pp neutrino measurement. The high ^{7}Be interaction rate enables a search for oscillations in its rate. So far two sources for a rate oscillation are known: the day night effect (caused by interactions of the neutrinos and the earth) and the seasonal modulation (caused by the earth's elliptical orbit) [66]. So called solar g-modes could be a further source. They cause density fluctuations in the solar which affects the solar neutrino rate. So far this oscillation has not been detected in the neutrino rate. Juno will be sensitive to up to 0.2% change in the amplitude of the solar neutrino rate, depending on the background model[116].

9.2 ^{8}B Neutrinos in Juno

Juno will also be able to measure solar ^{8}B neutrinos [117]. Its size is granting some benefits, while its shallow depth is a drawback. The acrylics, the steel scaffolding and the pmt cathodes will be a major source for external gamma ray background. It is created by ^{208}Tl and ^{214}Bi beta decays and α-n reactions. The gamma energies ranges up to $\sim 9\,\mathrm{MeV}$, with the lower

energies created by the beta decays, mainly 2.4 MeV and 2.6 MeV and the higher by neutron captures in the steel. The sheer size of the detector allows very stringent fiducial volume cuts to suppress this background. As the rate for the lower energies is higher a monte carlo study showed that an energy dependant fiducial volume is the most efficient [117]. The steps are:

- 2<E<3 MeV r<13m, 7.9 kt target mass
- 3<E<5MeV, r <15m, 12.2 kt target mass
- E>5MeV, r<16.5m, 7.9 kt target mass

Within these volumes the external background is negligible. There will be major efforts to reduce the internal background. Before the scintillator will be filled to the detector it will undergo three cleaning steps: distillation, water extraction and gas stripping[118]. The monitor the contamination of ^{238}U, ^{232}Th and Radon during the filling process the predector OSIRIS [119] is built. A feasible background scenario is 10 $^{-17}$g/g ^{238}U and ^{232}Th which is comparable to Borexino after filling[66]. The ^{214}Bi,^{212}Bi,^{214}Po and ^{212}Po can be tagged and removed by their respective fast Bi-Po coincidence as shown in chapter 4. The remaining internal background is ^{208}Tl (Q=5.0 MeV, $\tau_{1/2} = 3$ min). It is not distinguishable from a neutrino signal. However, its rate may be measured indirectly via the branching of ^{212}Bi as shown in chapter 4. After determining the rate, it can be subtracted statistically. The most critical background is cosmogenic background due to Juno's shallow overburden of 1700 m.w.e. This leads to a cosmic muon rate of 0.0037 Hz/m^2 with a mean energy of $\approx$ 290 GeV. This flux causes a rate of 3.6 Hz of muons crossing the scintillator. The muons create radio isotopes through spallation on the scintillator's carbon. The same isotopes as described in chapter 5 are created. The radio isotope rate is proportional to E$^{0.74}$ and can be scaled from Borexino results[95]. Table 9.1 shows the scaled rates. The massive ^{11}C rate dictates the 2 MeV threshold in the Juno ^{8}B neutrino analysis. Due to the long life time a veto strategy is not possible for this isotope. For the other isotopes a veto strategy is possible. A study was carried out that showed a possible veto strategy that reduces the radioisotope rate slightly below the neutrino [117]. The proposed veto strategy is:

- veto the whole detector for:

  2 ms if a muon crosses the water pool or scintillator

  1 after muons with failed track reconstruction

Cosmogenic Isotope	τ	Q[MeV]	Decay	Scaled Rate
^{12}B	0.03 s	13.4	β^-	2282
^{8}He	0.17 s	10.6	β^-	2185
^{9}C	0.19 s	16.5	β^+	160
^{9}Li	0.26 s	13.6	β^-	649
^{8}B	1.11 s	18.0	β^+	35
^{6}He	1.17 s	3.5	β^-	526
^{8}Li	1.21 s	16.0	β^-	725
^{10}C	27.8 s	3.6	β^+	816
^{11}Be	19.9 s	11.5	β^-	59
^{11}C	29.4 min	1.98	β^+	11811

Table 9.1: Muon induced background in Juno with decay mode, rates scaled from Borexino[95].

- cylindrical vetos with distance d around the muon track:

  d<1 for 5 s

  1 m<d<3 m for 4 s

  3 m<d<4 m for 2 s

  4 m<d<5 m for 0.2 s

- veto a 2 m sphere around a spallation neutron for 160 s.

This veto introduces a dead time of 48%. The spectral distribution of the scaled events is shown in figure 9.2. The ^{11}C decay rate dictates the threshold at 2 MeV. A toy monte carlo study based on chapter 7 and 8 was performed. It showed that Juno is still limited in search for sterile neutrinos by its shallow depth. The veto strategy against cosmogenic radio isotopes demands a huge deadtime, while still events remain after cuts. A more refined veto strategy based on a likelihood approach as demonstrated in [120] may improve the situation in the future.

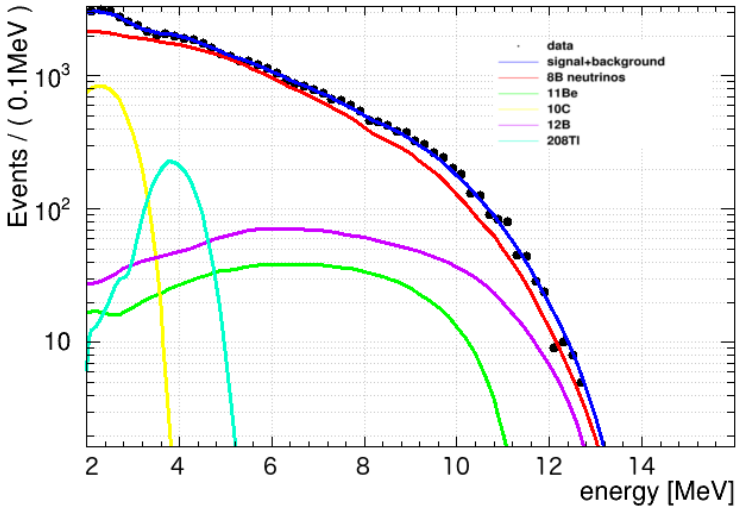

Figure 9.2: ^{8}B neutrino spectrum in the Juno detector, with background rates as shown in table 9.1

Chapter 10

The Double Chooz Experiment

The Double Chooz Experiment is a liquid scintillator based reactor anti neutrino experiment and the successor of the Chooz experiment [121]. Its main focus is the determination of the mixing angle θ_{13}. However a search for sterile neutrinos is also possible. For both analyses the proton number is crucial value to determine the expected rate. In this chapter a brief over of the set up, the latest physics result and the determination of the proton number will be given.

10.1 The Experimental Set Up

The Double Chooz experiment is located at the Chooz B nuclear power plant in the french Ardennes. The power plant consists of two pressurised water reactors of the N4 plant series with 4.25 GW thermal power each. The experiment is made of two identical detectors, the near (ND) and far (FD) detector, based on the liquid scintillator technique. The FD is built in a distance of 1050 m to the reactor, corresponding to the minimum in the oscillation. The ND has an average distance of 400 m to the cores, as its purpose is to measure the unoscillated spectrum. The relative locations are shown in figure 10.1. Both detectors are placed underground to shield cosmogenic background. The FD could use the experimental hall of the Chooz with an overburden of 300 m.w.e.. For the ND a new lab was constructed with a shallower depth of 120 m.w.e. The detectors are constructed in an onion like structure consisting of four interlaced cylindrical volumes. The three innermost volumes are optically separated from the fourth and make up the inner detector (ID). The outermost volume is the so called inner veto (IV). The detector is surrounded by 15 cm of steel to shield gamma rays. On top of the detector is the outer veto (OV) to close the gap caused by central chimney

which is needed to access the detector. In the following each detector part will be described briefly for more details see [122]

Outer Veto The Outer Veto consists of two orthogonal layers of plastic scintillator read out by PMTs. It is placed on of the IV overspreading an area of 13 m x 7 m. The chimney causes a gap of 1.1 m x 0.3 . To close this gap another pair of layers is placed $\simeq 4$ m above.

Inner Veto The Inner Veto consists of a hollow cylinder with 50 thickness and a volume of 90 m^3. The walls are made of stainless steel, therefore the IV is optically separated from the other detector parts. The IV acts as active veto for cosmic muons and fast neutrons created in the surrounding rock. It is equipped with 78 8 inch pmts with locations optimised for muon detection. In case of the ND the whole IV is covered in reflective foil (VM2000), for the FD for the inner wall reflective paint is used and for the outer wall reflective foil.

Buffer The Buffer consists of 100 m^3 transparent non-scintillating oil. With a thickness of 105 cm it acts as a passive shielding for the scintillating detector parts in the center from gammas and fast neutrons created in the rock and the outer detector parts. The buffer's outer wall is made of stainless steel with 390 10 inch PMTs mounted on it, that detect the scintillation light from the two inner detector parts.

Gamma Catcher The Gamma Catcher is a Volume with 55 m^3 and 55 thickness that surrounds the Neutrino Target. The two volumes are separated by a 12 mm thin acrylic vessel. The GC contains non-doped liquid scintillator with a light yield matched to the target scintillator to achieve a homogenous detector response. The GC is built to catch gammas created by inverse decays in the neutrino target, that escaped the target.

Neutrino Target The Neutrino Target is located in the very center of the Double Chooz detector. It contains 10.3 m^3 liquid scintillator loaded with Gd with a concentration of1 g/l. Gd is added as it features a high cross section for neutron capture and therefor is ideal for IBD detection. The scintillator is a mixture of PXE (phenyl xylyl ethane, $C_{16}H_{18}$) and dodecane($C_{12}H_{26}$)

The density of the liquids in the four subdetectors was matched to 0.804 g/cm^3 to avoid buoyancy forces. The radiopurity for the Target (GC) was found to be 0.4 (1.2)$\cdot 10^{-14}$ g/g u and 27.3 (1.8)$\cdot 10^{-14}$ g/g Th, which lies well within the specifications [123]. The PMTs are read are read out by a 8 bit flash ADC system. A trigger is issued when the energy in the ID exceeds 350 keV or

10 MeV in the IV. For each trigger, every PMT is read out. For Calibration the target is reachable via the Chimney. Various radioactive sources were deployed along the z axis. For the GC there is a guide tube system to insert sources. The PMTs and electrons is calibrated via an LED fiber system.

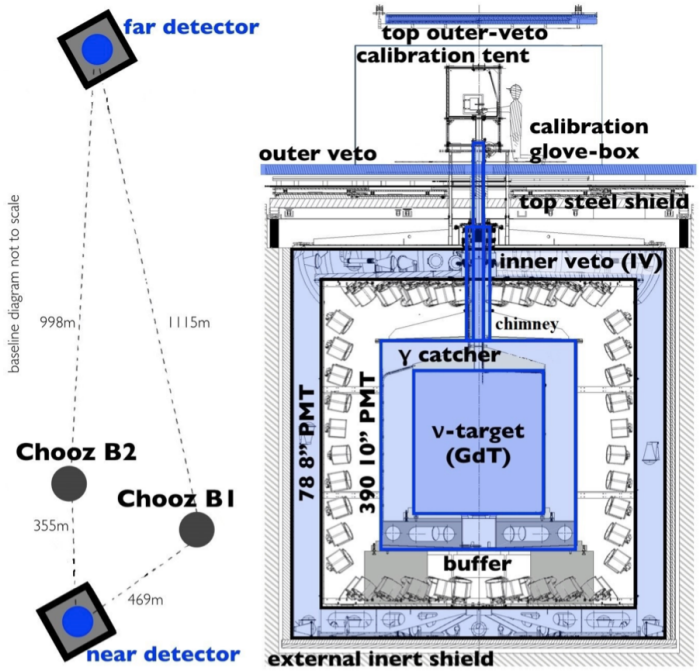

Figure 10.1: Cross section of the Double Chooz detectors. Also the respective distance to the reactor cores are shown, that result in an iso-flux configuration [124]

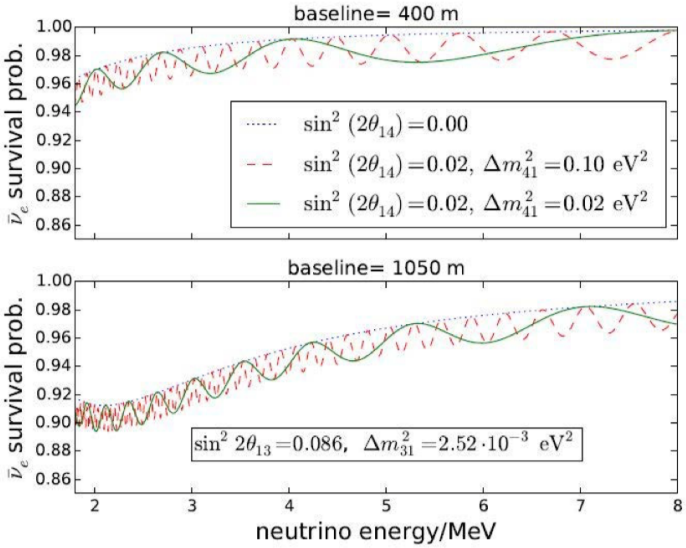

Figure 10.2: Survival probability of reactor $\bar{\nu}_\mathrm{e}$ for the ND (top) and FD(bottom). $\sin\theta_{14} = 0$ depicts the standard three neutrino case, the dashed lines show two examples for sterile neutrinos [125]

10.2 Neutrino Detection by Total Neutron Capture

For reactor neutrino experiments the inverse beta decay:

$$\bar{\nu}_\mathrm{e} + \mathrm{p} \rightarrow \mathrm{n} + \mathrm{e}^+ \tag{10.1}$$

is time-proven, as it delivers a significantly higher cross section than neutrino electron scattering. The cross section is deducted in [126] as:

$$\sigma_\nu(\mathrm{E}_\nu) \approx \mathrm{p_e E_e} \left(\frac{\mathrm{E}_\nu}{\mathrm{MeV}}\right)^{\mathrm{a(E}_\nu)} \cdot 10^{-43} \frac{\mathrm{cm}^2}{\mathrm{MeV}^2} \tag{10.2}$$

with the momentum of the electron $\mathrm{p_e}$ and

$$\mathrm{a(E}_\nu) = -0.07056 + 0.02018 \ln(\mathrm{E}_\nu/\mathrm{MeV}) - 0.001953 \ln^3(\mathrm{E}_\nu/\mathrm{MeV})$$

The detected signal is a convolution of the cross section and the reactor neutrino spectrum. Figure 10.3 depicts the three parts, where the detected signal ranges from 1.8 MeV up to $\sim$ 10 MeV with a maximum at 4 MeV. The coincidence of the inverse beta decay enables background suppression. The positron thereby forms the prompt signal and the neutron the delayed

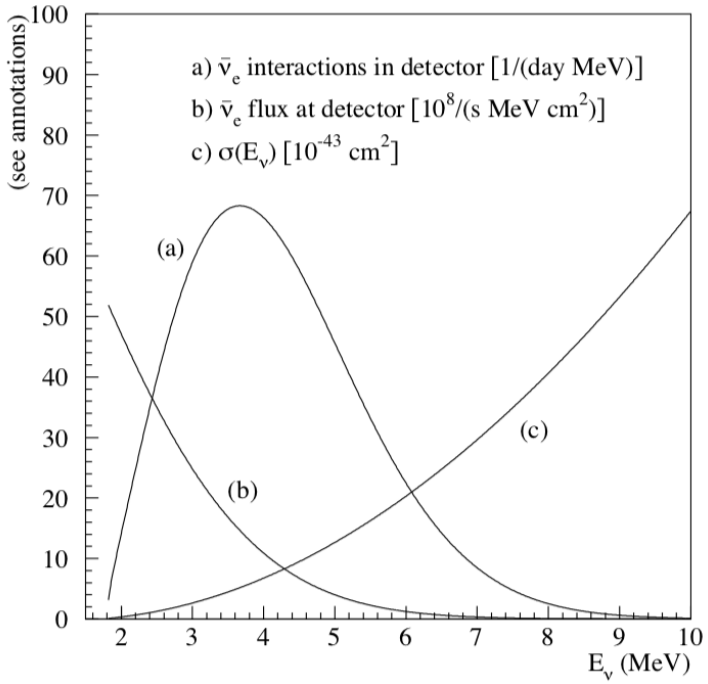

Figure 10.3: Detected reactor anti neutrino spectrum, which is a convolution of the inverse beta decay cross section and the reactor anti neutrino spectrum [127]

signal with a capture time of $\sim 200\,\mu$s for organic scintillators. In Double Chooz Gadolinium is added to the NT to increase the neutron capture cross section, which also drives down the capture time to $\sim 200\,\mu$s. Gd also shifts the capture gamma's energy from 2.2 MeV to $\sim$8 MeV. Double Chooz now is the first θ_{13} oscillation experiment that managed not only to use the Gd gammas but also the gammas generated by neutron capture on hydrogen. This allows to also use the GC as sensitive volume increasing the volume roughly by a factor of three.

Uncertainty (%)	SD	MD
Proton Number	0.65	0.39
IBD Selection	$0.33^{\mathrm{FD}}/0.12^{\mathrm{ND}}$	0.27
Boundary Effect	0.20	-
Vetoes Efficiency	$\leq$0.005	$\leq$0.005

Table 10.1: Systematics for the θ_{13} in Double Chooz [124].

The systematics are summarised in table 10.1, with SD being the phase where

just the FD took data and MD the phase where both detectors where running. The uncertainty on the proton number in the detection volume causes the largest contribution to the uncertainty on θ_{13}. The proton number uncertainty is dominated by the GC with an uncertainty of 1.1% compared to 0.3% for the NT. During filling it was not expected that the GC can be used as sensitive Volume, so just the scintillator going in the NT was weighed. For the GC the mass going in the GC was just monitored via a flow meter. During emptying the detector the scintillator could be weighed, with details given in the next chapter. Background events have to mimic the

Rate (d^{-1})	FD	SD
IBD Candidates	112	816
Breakdown		
Accidental	4.13±0.02	3.110±0.004
Fast-Neutron	2.50±0.05	20.85±0.31
^{9}Li	2.62±0.27	14.52±1.48
^{9}Li +μ tag	3.01±0.60	12.32±2.01
Stopped μ	<0.19 (98% CL)	<0.21 (98% CL)
Others (^{12}B, Bipo)	<0.01	0.04±0.01
Total		
$\sum$-Exclusive	9.3±0.3	38.5±1.5
Inclusive	9.8±0.9	39.6±2.5
Signal to BG	11.0	20.2

Table 10.2: Background rates for the θ_{13} measurement in Double Chooz [124].

IBD signal, so it can be events directly causing two events in the detector or a coincidence of two single events. Due to the low overburden cosmogenic background is dominating in Double Chooz, meaning fast neutrons and cosmogenic radioisotopes. Fast neutrons are recreating the IBD signal by first recoiling on a hydrogen atom followed by a neutron capture. ^{9}Li is created via spallation on ^{12}C and undergoes a β-n decay. After each tagged muon a veto of 1.25 ms is issued. This is mainly to reject fast neutrons and stopped muons. To veto ^{9}Li and ^{12}B events an artificial neural network was developed (ANN). The ANN uses information from the ID, IV and OV. The ANN is also used to suppress accidental coincidences. The remaining background rates after cuts are given in table 10.2. ^{9}Li was carefully studied in time windows when both reactors were not running totalling to 17 days. However, it still is the dominant background systematic. Other background models could also be checked during this time period, which is a unique characteristic of

the Double Chooz experiment.
The θ_{13} measurement is done comparing the detected rate+shape of the IBD signals to the model predictions given by

$$P(\bar{\nu_e} \rightarrow \bar{\nu_e}) \simeq 1 - \sin^2 2\theta_{13} \sin^2(1.267 \Delta m^2_{ee} L/E_{\bar{\nu_e}}) \tag{10.3}$$

where L is the baseline distance between each reactor detector pair, E_{ν_e}(MeV) is the neutrino energy obtained from the prompt energy deposition or visible energy ($E_{\nu_e} \simeq E_{e^+} + 0.78\,\text{MeV}$). Δm^2_{ee} is the pertinent ν_e-weighted average of Δm^2_{31} and Δm^2_{32}, where $|\Delta m^2_{ee}| = (2.484 \pm 0.036) \cdot 10^{-3} \text{eV}^2$ is used as input to the fit. Three single detector (SD) fits, namely FD-I, FD-II and ND, are performed simultaneously. The fit outputs are given to the final fit. The SD fits are constraint by inter detector correlations, like the background shape, detection rate and spectral shape. Therefore, the ND acts as an unoscillated rate+shape reference. Correlations to FD-I and FD-II cancel systematic uncertainties, where the iso-flux FD-II benefits more. Figure 10.4 (middle) shows an excess around 5 MeV with a still unknown origin. Figure 10.4 (bottom) shows the inter detector ratio fit, where the excess could successfully be suppressed. Finally, the best fit value is $\sin^2\theta_{13} = 0.105 \pm 0.014$, with a statistical portion of the uncertainty of 0.005. Hence, the systematics are clearly dominant. As FD-I still represents a large amount of the analysed data, the reactor flux uncertainty for this period are the largest contribution to the final result. However FD-II already improved the uncertainty compared to single detector operation. Once the full data set is released the impact of FD-I will be minimised. Figure 10.5 compares the DC value for θ_{13} to other experiments and shows that the DC value is up to $\sim 50\%$ higher. Although the significance of this deviation is below 2σ.

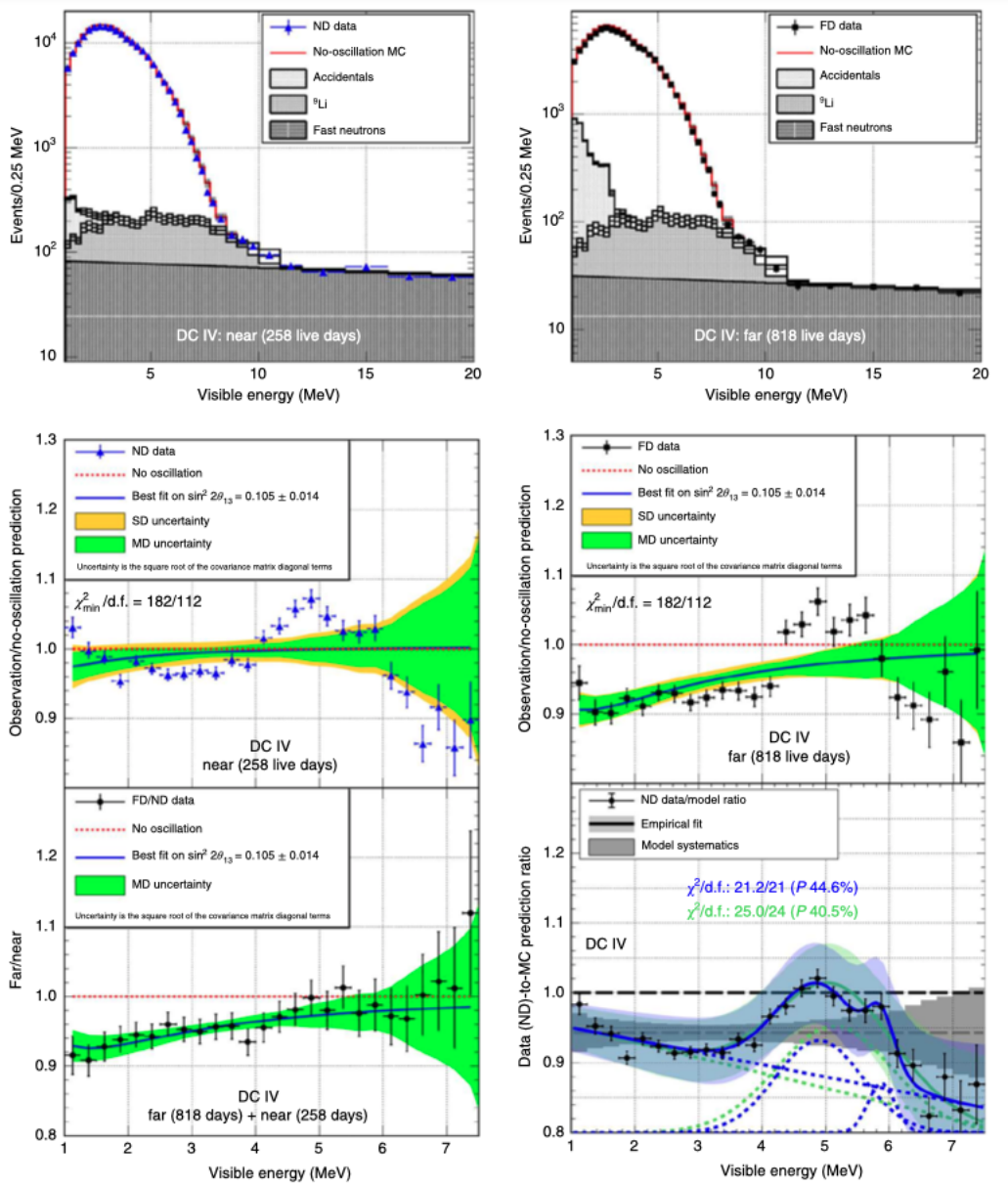

Figure 10.4: **ND and FD spectra and ratios**:*top:*Spectra of IBD candidates plus unoscillated MC spectrum and background model. *center:* The best fit solution (blue) and no-oscillation hypothesis in red are shown. The excess at 5 MeV is clearly visible. *bottom:* The data-to-data ratio on the left shows a clear disappearance with no remaining distortions. The data-to-MC ration on the right allows an extraction of the excess at 5 MeV [124].

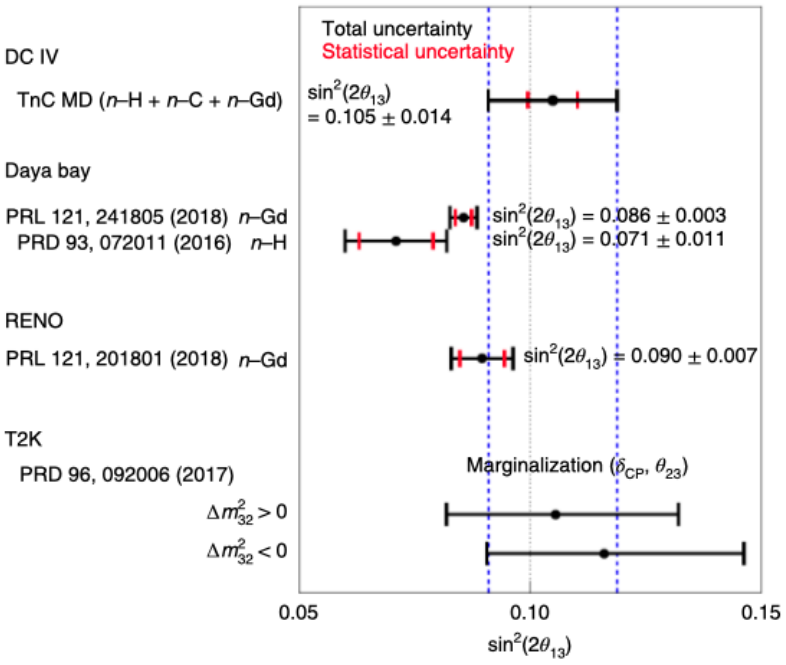

Figure 10.5: Comparison of the Double Chooz results with Daya Bay[128], RENO[129] and T2K [130]

10.3 Measurement of the Proton Number for the Gamma Catcher Liquid

The two detector phase began with the start of the data taking of the ND at the end of 2014 and lasted for three years until the end of 2017 where both detectors stopped taking physics data. It is agreed with EDF, the operator of the power plant, that the equipment in the lab has to be fully dismantled. During the dismantling of the ND the opportunity to measure the GC mass arises. How it was done will be described in the following.
For an accurate measurement the acrylic walls have to be intact also during emptying the detector, i.e. no cracks are allowed to form. Therefore the liquid levels have to be as precisely monitored as during the filling period described in [122] and controlled in a way that the maximal liquid level difference does not exceed 1 cm. The level measurement system described in [122] could be reactivated partly. The system is run by a RaspberryPie with several sensors connected to it. A web server is running on the RaspberryPie to grant access to the data. The hydrostatic pressure sensors (HPS) for each volume could be fixed and were fully operational again. The other sensors were not deemed necessary and were not fixed. A TruSense S310[131] infrared laser was installed at the chimney opening. In contrast to the former laser level measurement system, that laser does not need a reflective swimmer in the liquid. Therefore access through the chimney was sufficient to monitor the target level with that new laser with a precision of 1 mm. The XRS system [132] was also installed to provide an independent system. It is made of tubes that are submerged in all four liquids that are connected at the top. A common under pressure can be applied that rises the levels to the XRS panel above the detector. The system does not provide an absolute measurement but shows the difference of the four levels. An example measurement from the start of the unfilling is shown in figure 10.6
Part of the filling system could be reused for emptying the detector. The NT and GC filling pipes were suitable for emptying. For the BF and MV new connections had to be installed. For both ptfe tubes were inserted in the loris tubes, as the laser level measurement system was not in use and as they go all the way to the bottom of the volumes. The NT and GC were connected to the filling pumping stations. The stations are equipped with small membrane pumps[122] that run on nitrogen. As these two volumes are the smallest of the four, small pumps were sufficient to not be limited by them. The BF and MV tubes were connected to membrane pumps run by compressed air. During operation they showed to be not reliable probably caused by the high humidity in the lab. Therefore, they were replaced by

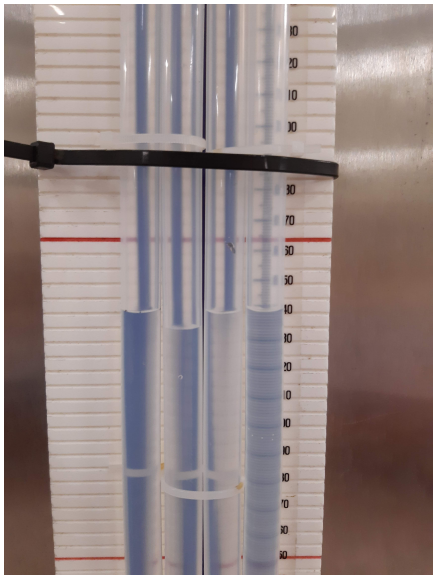

Figure 10.6: Croos reference system (XRS). It is connected to the four detector volumes. The liquids can be sucked up and the fill heights can be relatively compared.

the Mega 960 pumps [132] from the liquid storage area run by nitrogen. All the pump outlets were connected to intermediate bulk container (IBC) with a volume of $1m^3$ each. Ten IBC were solely used to store the target liquid, while for the other three volumes 48 IBCs were in use. The IBCs that were connected to the NT and GC were put on scales (see fig 10.9 for GC). For each the empty IBC was weighed, the scale tared and the weight after filling the IBC measured. Around 30 IBCs could be stored in the lab simultaneously and were arranged in rows of two as depicted partly in figure 10.7. Full IBCs were at all time stored in retention pits as shown in figure 10.7. Once full, the IBCs were brought up to the storage area[1] by a telescopic handler.(figure 10.8). The full IBCs in the storage were emptied by a tank truck. The trucks were equipped with their own pump and sucked the liquid from the IBC's manhole. In total seven trucks were needed to transport the liquid. Further disposal of the liquids was handled by the GVS [133] company.
Figure 10.10 shows the data aquired by the level measurement system. Fill height differences between the volumes could be held within the safety margin. No hint of the position of the leak from the NT to the GC[124] is visible in the data. Especially, during the time of no pumping were all levels are constant. Table 10.3 sums up the individual measurement of the GC IBCs.

[1] tarred area at the entrance of the tunnel

Figure 10.7: Overview of the emptying operation. XRS, IBCs and pumps are visible.

The total mass is (17845.6 ± 3.5)kg where the error is defined by the used scale. From geometric calculations of the volume 18200 kg are expected[123]. Upon further dismantling the bottom of the GC volume can be checked for leftover liquid and if necessary the liquid can be taken into account. The proton fraction in the GC liquid was measured to be $f_H = (14.53 \pm 0.15)\%$ using combustion analysis [123]. This gives a proton number of the extracted liquid of $(1.451 \pm 0.010) \cdot 10^{30}$.

Figure 10.8: *left:* Full IBCs in the storage area.*right:* Liquid transfer from the IBCs to a truck.

Figure 10.9: IBC on scale for the GC mass measurement.

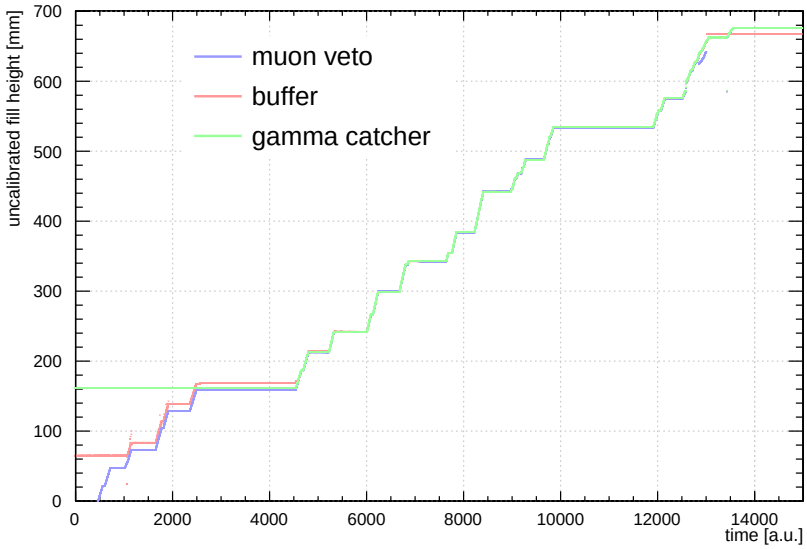

Figure 10.10: Fill heights during emptying. No hint for the position of the leak is visible, especially during times with no pumping all fill heights are constant.

IBC number	mass[kg]
IBC1	760.6
IBC2	768.1
IBC3	763.9
IBC4	761.5
IBC5	762.2
IBC6	760.6
IBC7	763.5
IBC8	761.9
IBC9	758.6
IBC10	761.6
IBC11	763.9
IBC12	746.2
IBC13	747.3
IBC14	747.4
IBC15	747.1
IBC16	747.1
IBC17	747.1
IBC18	742.6
IBC19	742.8
IBC20	741.7
IBC21	750.5
IBC22	749.8
IBC23	750.9
IBC24	498.7
total	17845.6
expected	18200

Table 10.3: Weight measurement of individual IBCs for the gamma catcher weight measurement

10.4 Sterile Neutrinos in Double Chooz

For the given baseline of the Double Chooz experiment and the energy of reactor neutrinos, the experiment should be sensitive for sterile neutrinos in the mass range of $5 \cdot 10^{-3}\mathrm{eV}^2 \leq \Delta\mathrm{m}^2_{41} \leq 3 \cdot 10^{-3}\mathrm{eV}^2$ and mixing angles of $\sin^2\theta_{14} \geq 0.02$. How the analysis is performed will shortly be described in the following with a deeper explanation in [125].
For the present analysis one sterile neutrino is introduced, i.e. the mixing matrix is extended to 4x4 with the new mixing angles $\theta_{14}, \theta_{24}, \theta_{34}$, the new mass state m_4 and an additional CP violating phase. For Double Chooz's baseline and small mixing, just the relevant parameters are $\theta_1 4$ and the difference of squared masses $\Delta\mathrm{m}^2_{41} = \mathrm{m}^2_4 – \mathrm{m}^2_1$. This leads to an approximation of the survival probability of:

$$\begin{aligned} \mathrm{P}_{\bar{\nu}_\mathrm{e}\to\bar{\nu}–\mathrm{e}}(\mathrm{E},\mathrm{L}) \simeq 1 – \sin^2(2\theta_{13})\sin^2\left(1.267\frac{\mathrm{MeV}}{\mathrm{eV}^2\mathrm{m}}\frac{\Delta\mathrm{m}^2_{\mathrm{ee}}\mathrm{L}}{\mathrm{E}}\right) \\ –\sin^2(2\theta_{14})\sin^2\left(1.267\frac{\mathrm{MeV}}{\mathrm{eV}^2\mathrm{m}}\frac{\Delta\mathrm{m}^2_{41}\mathrm{L}}{\mathrm{E}}\right) \end{aligned} \tag{10.4}$$

with the neutrino energy E and the baseline L and the first term being the standard mixing for the standard three neutrino case and the second describing the mixing due to the sterile neutrino. For Double Chooz this would lead to an additional disappearance superimposed to the three flavour mixing. The effect is shown in figure 10.2 with the for the θ_{13} measurement optimised baselines of 400 and 1050 m and reactor neutrino energies roughly between 1 and 8 MeV. That leads to a sensitive range of L/E, for the additional disappearance, of 50 m/MeV to 1000 m/MeV. The analysis is done via a profile likelihood ratio that uses the parameters $\sin^2 2\theta_{14}$ and $\Delta\mathrm{m}^2_{41}$. To test a oscillation signal, the best fit standard 3 flavor model i.e. $\sin^2 2\theta_{14} = \Delta\mathrm{m}^2_{41} = 0$(null hypothesis) is compared to the best fit 3+1 model that maximises the likelihood for the dataset using the test statistics:

$$\lambda(\vec{\mathrm{x}},\vec{\eta}) = –2 \cdot \ln\frac{\sup\mathcal{L}\left(\vec{\mathrm{x}}|\vec{\eta},\vec{\xi}\right)}{\sup\mathcal{L}\left(\vec{\mathrm{x}}|\widehat{\vec{\eta}},\widehat{\vec{\xi}}\right)} = –2\Delta\ln(\mathcal{L}) \tag{10.5}$$

with vecx being the dataset, $\vec{\eta}$ the model parameters $\sin^2 2\theta_{14}$ and $\Delta\mathrm{m}^2_{41}$ and $\vec{\xi}$ additional parameters i.e. background, reactor flux etc. described in the following. Data between 1 MeV to 20 MeV is used, where the region 1-8 MeV is dominated by the signal and the region 8-20 MeV dominated by

background. The higher energy region is used to constrain the backgrounds. The fit handles several systematic uncertainties. The normalisation of the reactor flux in each bin is a free fit parameter with constraints given by 3x41 reactor flux parameters. $\mathrm{Sin}^2\theta_{13}$ and $\Delta\mathrm{m}_{\mathrm{ee}}$ are free parameters, with $\Delta\mathrm{m}_{\mathrm{ee}}$ given the global best fit value as starting parameter. The shape of the radio cosmogenic ^{9}Li is assumed to be the same for the FD and ND while rate is different du to the different overburden. The shape was studied in [40] with the help of a high energy muon subsample and is modelled with 38 parameters. The total rate is not constrained. Accidental backgrounds are studied with randomised events and considered uncorrelated between data sets. Fast neutrons and stopping muons are described via:

$$\mathrm{R(E)} = \mathrm{R}_0\,(\mathrm{a}\cdot\mathrm{E} + \mathrm{b}\cdot\exp(-\lambda\cdot\mathrm{E})) \tag{10.6}$$

with the total rate R_0 and the three shape parameters λ,a and b. The shape is again the same for ND and FD with different rates for the detectors.
The expected reactor anti neutrino spectrum plus the backgrounds are compared to the data in figure 10.11. For $\theta_{14} = 0$ the fit has been thoroughly tested and compared to the DC standard analysis. A good agreement between the two has been found. To find the global minimal likelihood the phase space of $(\theta_{14}, \Delta\mathrm{m}^2_{41})$ is scanned, where at each point the signal parameters are fitted. Using the test statistics λ one can compare each point to the null hypothesis i.e. the standard three neutrino case.
Figure 10.12 shows the result of the scan, where the 95% percent curve equals $\lambda \geq 3.84$. The area on the right of the curve can be excluded. The best fit value is at $\sin^2 2\theta_{14} = 0.043$ and $\Delta^2_{41} = 0.028\,\mathrm{eV}^2$ with a p-value of (24.7±2.2)%. Therefore it is fully compatible with the standard three neutrino case and no sterile neutrino is found within the Double Chooz data.

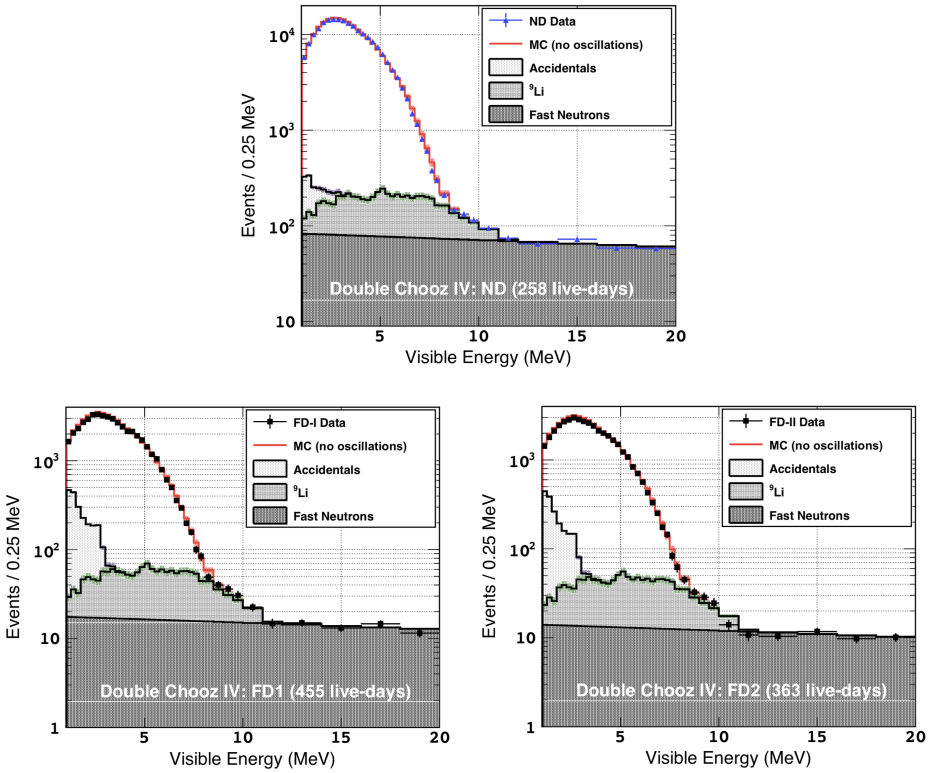

Figure 10.11: Prompt event spectra of the ND, FD I and FD II. The bon oscillated MC spectrum is shown in red. The background models are depicted grey [125].

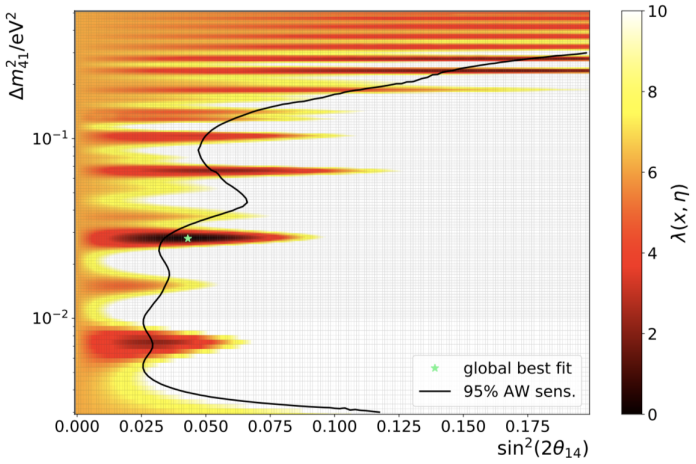

Figure 10.12: Example scan of pseudo data generated with the null hypothesis. The blue line represents the 95% exclusion limit [125].

Chapter 11

Current Situation of Sterile Neutrinos

Several experiments released data on sterile neutrinos. Some exclude part of the parameter space of the anomalies, while other favor a signal. So the situation is a bit diffuse. A brief overview will be given in the following. A combined analysis of the reactor experiments NEOS [134] and DANSS [135] gives a best fit value of $\sin^2(2\theta) = 0.049$ and $\Delta m^2 = 1.29 eV^2$ with a significance of $3.7\,\sigma$, which is dominated by the DANSS data [136]. This mixing is smaller than predicted by the reactor rate anomaly (RRA) and the Gallium anomaly, generating a tension of $\sim 2\sigma$ [137] The combined data of DANSS, NEOS, Bugey-3 [138] and PROSPECT [139] results in a best fit value of $\sin^2(2\theta) = 0.026$ and $\Delta m^2 = 1.29 eV^2$ with a significance of $1.8\,\sigma$ [140]. Figure 11.1 depicts the corresponding confidence zones.
Neutrino-4 also found a signal with a best fit value of $\sin^2(2\theta) \approx 0.26$ and $\Delta m^2 \approx 1.29 eV^2$ with a significance at the $3\,\sigma$ level [141]. This result is not seen favorably by the community as can be seen e.g. in [142]. The result is not consistent wit DANNS, PROSPECT and solar neutrino data [143]. Figure 11.1 depicts the tension with other experiments. MiniBooNE presented new results where the combination of neutrino and anti neutrino data leads to an increased excess of 4.8 σ with a best fit value of $\sin^2(2\theta) = 0.807$ and $\Delta m^2 = 0.043 eV^2$ [144]. IceCube released an analysis based on $\nu_\mu/\bar{\nu}_\mu$ disappearance which disfavors the three neutrino and (3+1) relative to the unstable neutrino neutrino model with p- values of 2.5% and 0.81%, respectively. This analysis excludes the by short baselines experiments preferred parameter space with 90% C.L. A new global analysis [152] reduced the allowed parameter space compared to the original anomalies and shifted the mixing angle to smaller values. The best fit values are $\sin^2(2\theta) = 0.0.053$ and $\Delta m^2 = 1.32 eV^2$ for

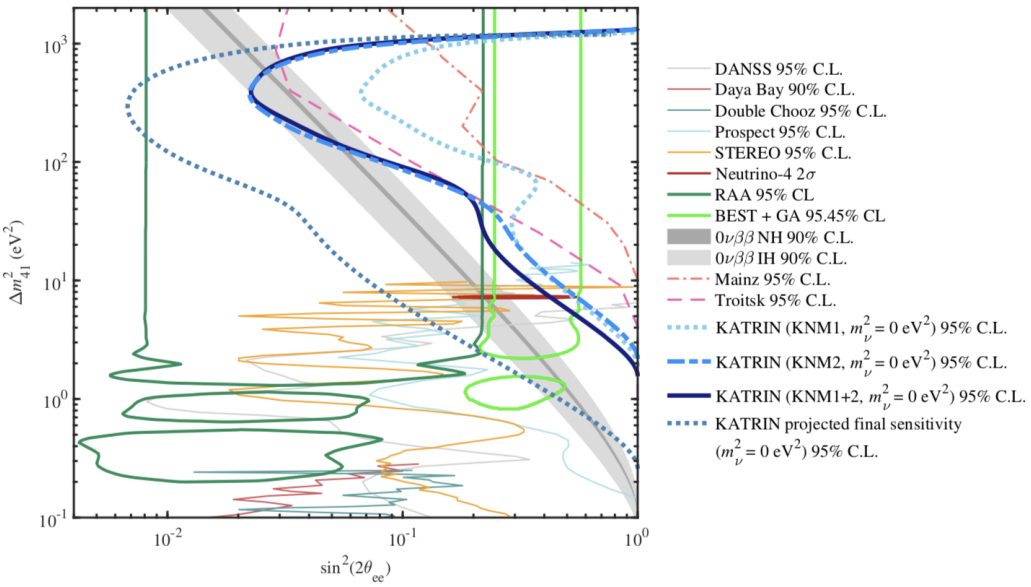

Figure 11.1: Summary of current sterile neutrino experiments. The green line depicts the RAA-Galium anomaly [145]. Included are short baseline experiments [146, 147, 148, 125, 149], constraints from $0\nu\beta\beta$ as grey band [150] and results based on the tritium spectrum [151]. Plot taken from [151]

the (3+1) model and favors the sterile hypothesis with more than $5\,\sigma$. The tension between the appearance and disappearance experiments still exists at a $4.5\,\sigma$ level. The tension is mainly created by Minos&Minos+ [153] and the IceCube[154] experiment. Several different models that could reduce this tension are studied. In the (3+2) model the tension still exists. The (3+1+decay) model where the fourth mass state is unstable reduces the tension to $3.2\,\sigma$[152]. Such a model is also more consistent with cosmological data which disfavors ev-scale sterile neutrinos. N_{eff} the number of relativistic neutrinos is consistent with three and the total mass of relativistic neutrinos is $m_\nu \lesssim 0.1\,\text{eV}$. The cosmological model assumes that that the sterile and active neutrinos are in thermal equilibrium during decoupling. Hence, models that avoid this reduce this tension [137, 152]. Alongside sterile neutrinos different models beyond the standard are investigated, see [155, 156, 157, 158, 159].
Besides that, also the anomalies are reassessed. The Gallium anomaly was recalculated with an updated cross sections, which decreased it to $2.3\,\sigma$ [160]. The excess at around 5 MeV in reactor experiments, mentioned in section 10.2 and also measured by RENO [161] and Daya Bay [162] rises doubts on the RAA as it deviates from the used Huber-Mueller[51] flux by $\sim$ 10 %.

Furthermore the burn up of the nuclear fuel was not considered in the RAA, which affects the neutrino rate. A reanalysis using an updated flux prediction [163, 164] results in a significance ranging from $0.9\,\sigma$ to $2.8\,\sigma$[165]. The MiniBooNE excess is also seen critically as it just shows up in the lowest energy bins and is not compatible with the (3+1) model [166]. Backgrounds that could mimic the excess are thoroughly studied by the collaboration. So far none could explain the excess [144].

Chapter 12

Conclusion

In the past decades several liquid scintillator based neutrino neutrino experiments were realised and increased our understanding of the neutrinos and their sources. Their target mass is usually enormous to counteract the small cross sections of the neutrino interactions. Most of the experiments are build in underground laboratories to shield the cosmic radiation.
The Borexino experiment is located in the Laboratori Nationali del Gran Sasso (LNGS) in Italy with a rock overburden of ~ 3800 meter water equivalent (m.w.e.). It started data taking in May 2007. Its main purpose is the spectroscopy of solar neutrinos. It reached an unprecedentedly high radiopurity and an energy resolution of $\sim 5\%$ at 1 MeV which enabled it to perform a wide-ranging physics program. One of the highlights that is the first experiment to measure each solar neutrino branch.
The first part of this work focuses on the detection of ^{8}B neutrinos of the pp chain with Borexino. As these are rare events, the detector and backgrounds have to be well understood. Borexino detects solar neutrinos through elastic scattering on electrons where the cross section for electron neutrinos is about a factor of six higher. The initial neutrino energy is lost in this channel, also there is no directionality information. To achieve its purity Borexino performed a severe purification campaign using the water extraction technique. During this operation Radon and its daughter nuclides were introduced to the scintillator. Therefore the data during the operation until five days after the end is excluded. However, the operation was successful and decreased the impurities by another order of magnitude. The success is visible in the internal background rate. The fast coincidences ^{214}Bi-^{214}Po and the ^{212}Bi-^{212}Po of a beta and alpha decay, respectively, are tagable on an event-to-event basis and show a huge decrease after purification. The ^{212}Bi-^{212}Po coincidence is also used to determine the ^{208}Tl rate as the branching of ^{212}Bi to ^{212}Po

and ^{212}Bi to ^{208}Tl is known. In this way it was determined that 50.7±7.1 ^{208}Tl are within a radius of 3 m. Another major background is made up of cosmic muons. They were identified with with muon trigger board (MTB), a hardware trigger and the muon clustering (MCR), a software trigger. Both use the outer detector (OD). The inner detector is optically separated from the ID and as the muons deposit energy on a track, identify them via pulse shape. It was shown that the muon identification efficiency is well above the design goal of 99.992%. The muons not only constitute direct background, but can via spallation processes on ^{12}C of the scintillator create cosmogenic radioisotopes. It was shown that a veto after a muon of 6.5 s after a muon is effective against the lived isotopes. The found rates are compatible with [95]. To veto the longer lived ^{10} a veto of 120 s after a muon with an accompanying neutron is issued. The production of ^{11}Be is not accompanied with a neutron. However, neutrons indicate a large energy deposition in the detector. Hence, it was determined that a large fraction of the ^{11}Be rate is covered by the 120 s window with a remaining rate of $(3.2 \pm 0.6) \cdot 10^{-3}$ cpd/100t. The stainless steel sphere (SSS) and the cathodes also contribute to the background, as they are contaminated with ^{208}Tl and ^{214}Bi. They both undergo beta decays where ^{208}Tl emits a 2.6 MeV gamma and ^{214}Bi several gammas with energies up to 3.2 MeV. It was shown that these gammas even reach a fiducial volume(fv) with a radius of 3 m with a rate of 0.005 cpd/100t. The threshold is defined with an AmBe source that can be lowered into the detector. it is a neutron emitter and through neutron capture it can emit gammas from 2.2 MeV up to ∼10MeV. Another source of external gamma background are neutron captures, where the neutron is produced through alpha-n reactions. The neutrons get captured on the SSS and produce gammas up to ∼10MeV. Their contribution is visible in the radial distribution of events above 6 where besides them just homogenous distributed events are expected.

Inside a fv of 3 m a counting analysis is possible. The known background rates are subtracted from the total event number. This results in 484±24 detected neutrino events. A second analysis was performed where to goal is to use the hole detector volume. This introduces the background caused by the inner vessel (IV). ^{208}Tl sits on it which undergoes a beta decay. Moreover, the external background gets more dominant closer to the IV. For each signal and background component events were simulated under the respective detector conditions for each run used in the dataset. The simulated numbers were scaled to the respective run length. From these events spectral and radial probability density functions are generated (pdf). These pdf's are fitted to the 2.54 kt years of accumulated data resulting in 1376±58 ^{8}B neutrino events in the data. This allows to study the spectral shape of the

^{8}B neutrinos, especially to look for sterile neutrinos. Sterile neutrinos are non interacting through the weak interaction, however can couple through oscillation to the standard neutrinos. Several experiments hint to their existence citeLSND:2001aii,Gariazzo:2015rra,PhysRevC.83.054615. They would also change the survival probability of solar neutrinos [108]. For several sterile neutrino parameters events were simulated in the same way as for the standard three neutrino case and pdfs were extracted. They were also fitted to the data. Through a comparison of the likelihoods no hints for a sterile neutrino could be found.
The Jiangmen Underground Neutrino Observatory (JUNO) is a multi purpose liquid scintillator neutrino experiment, that is currently under construction [112]. Its main goal is to detect antineutrinos created in nearby nuclear power plants. Therefore a 20 kt fiducial mass and an unmatched energy resolution of 3%/MeV is planned and a shielding of ∼1700 m.w.e.. The main physics goal is the determination of the mass hierarchy. Apart from this it is also sensitive to solar neutrinos. Especially to the lower energetic part of the solar as cosmic background is not crucial there. The high interaction rate of ^{7}Be even allows to study timely variations in the signal amplitude down to 0.2% of the amplitude [116]. It will also be sensitive to ^{8}B neutrinos. To combat the high radioisotope rate caused the 3.6 Hz muon rate a stringent veto proposed. A cylinder around a muon track is vetoed, with longer veto times closer to the track. This introduces a dead time of 48%. It is not possible to tag the cosmogenic ^{11}C decays which then define the 2 threshold of the analysis. External background can be handled with a stringent fv thanks to JUNOs sheer size and can be neglected inside the fv. A toy monte carlo was set up were the were the cosmogenic radioisotopes were scaled from Borexino. Again pdfs for radial and spectral distribution were constructed. It showed that JUNOs high muon rate limits its search for sterile neutrinos.
The Double Chooz Experiment is a liquid scintillator based reactor anti neutrino experiment and the successor of the Chooz experiment [121]. It's main focus is the determination of the mixing angle θ_{13}.The Double Chooz experiment is located at the Chooz B nuclear power plant, consisting of two 4.25 GW reactor cores, in the french Ardennes. It is made up of two similar detectors the near detector (400 m baseline and of 120 m.w.e. overburden) and the far detector (1050 m baseline and 300 m.w.e. overburden). The reactor neutrinos are detected via the inverse beta decays. The background is mainly caused by muons and their secondary particles, where ^{9}Li is dominant. The θ_{13} measurement is done comparing the detected rate+shape of the IBD signals to the model predictions. The data of the two detectors is fitted simultaneously. Double Chooz is the first experiment not use not only the neutron capture on Gadolinium for this analysis, but also the ones from

capture on hydrogen. The analysis revealed an excess around 5 MeV with a still unknown origin. The the best fit value is $\sin^2\theta_{13} = 0.105 \pm 0.014$. A large contribution is due to the uncertainty of the proton number in the Gamma Catcher. During decommissioning of the near detector the mass of the gamma catcher was carefully measured. This reduced the uncertainty of the proton number roughly a factor of two. The Double Chooz experiment is also sensitive to sterile neutrinos. The analysis is done via a profile likelihood ratio that uses the parameters $\sin^2 2\theta_{14}$ and Δm^2_{41}. The best fit standard 3 flavor model is compared to the best fit 3+1 model that maximises the likelihood for the dataset. To find the global minimal likelihood the phase space of $(\theta_{14}, \Delta m^2_{41})$ was scanned. The result is fully compatible with the standard three neutrino case and a large part of the parameter space for a sterile neutrino could be excluded.

List of Figures

List of Tables

Bibliography

[1] C. l. Cowan et al. Detection of the free neutrino: a confirmation. *Science*, 1956.

[2] B. T. Cleveland, Timothy Daily, Raymond Davis, Jr., James R. Distel, Kenneth Lande, C. K. Lee, Paul S. Wildenhain, and Jack Ullman. Measurement of the solar electron neutrino flux with the Homestake chlorine detector. *Astrophys. J.*, 496:505–526, 1998.

[3] Raymond Davis. A review of the homestake solar neutrino experiment. *Progress in Particle and Nuclear Physics*, 32:13 – 32, 1994.

[4] Q. R Ahmad et al. Direct evidence for neutrino flavor transformation from neutral-current interactions in the sudbury neutrino observatory. *Journal of Physics G: Nuclear and Particle Physics*, Jun 2010.

[5] K. Eguchi et al. First results from kamland: Evidence for reactorantineutrino disappearance. *Phys. Rev. Lett.*, Jan 2003.

[6] Y. Fukuda et al.(Super Kamiokande Collaboration). Evidence for oscillation of atmospheric neutrinos. *Phys. Rev. Lett.*, 1998.

[7] P. A. Zyla et al. Review of Particle Physics. *PTEP*, 2020(8):083C01, 2020.

[8] S. M. Bilenky. Majorana neutrino mixing. *J. Phys.*, G32:R127, 2006.

[9] G. Alimonti. The borexino detector at the laboratori nazionali del gran sasso. *Nuclear Instruments and Methods in Physics Research A*, 2009.

[10] G. et al. Bellini. Final results of borexino phase-i on low-energy solar neutrino spectroscopy. *Phys. Rev. D*, 89:112007, Jun 2014.

[11] G. et al. Bellini. Neutrinos from the primary proton proton fusion process in the Sun. *Nature*, 512(7515):383–386, 2014.

[12] G. et al. Bellini. First evidence of pep solar neutrinos by direct detection in borexino. *Phys. Rev. Lett.*, 108:051302, Feb 2012.

[13] M. et al. Agostini. Spectroscopy of geoneutrinos from 2056 days of borexino data. *Phys. Rev. D*, 92:031101, Aug 2015.

[14] Steven Weinberg. A model of leptons. *Phys. Rev. Lett.*, 19:1264–1266, Nov 1967.

[15] Y. Fukuda et al. Evidence for oscillation of atmospheric neutrinos. *Phys.Rev. Lett.*, Aug 1998.

[16] Ziro Maki, Masami Nakagawa, and Shoichi Sakata. Remarks on the Unified Model of Elementary Particles. *Progress of Theoretical Physics*, 28(5):870–880, 11 1962.

[17] Makoto Kobayashi and Toshihide Maskawa. CP Violation in the Renormalizable Theory of Weak Interaction. *Prog. Theor. Phys.*, 49:652–657, 1973.

[18] Nicola Cabibbo. Unitary symmetry and leptonic decays. *Phys. Rev. Lett.*, 10:531–533, Jun 1963.

[19] Boris Kayser. Neutrino Mass, Mixing, and Flavor Change, 2002.

[20] Marek Zralek. From kaons to neutrinos: Quantum mechanics of particle oscillations. *Acta Physica Polonica B*, 29, 11 1998.

[21] Boris Kayser. Neutrino Oscillation Phenomenology. In *Neutrinos in particle physics, astrophysics and cosmology. Proceedings, 61st Scottish Universities Summer School in Physics, SUSSP61, St. Andrews, UK, August 8-23, 2006*, pages 51–64, 2008.

[22] F. Capozzi, E. Lisi, A. Marrone, D. Montanino, and A. Palazzo. Neutrino masses and mixings: Status of known and unknown 3ν parameters. *Nuclear Physics B*, 908:218 – 234, 2016. Neutrino Oscillations: Celebrating the Nobel Prize in Physics 2015.

[23] B. Aharmim et al. Electron energy spectra, fluxes, and day-night asymmetries of B-8 solar neutrinos from measurements with NaCl dissolved in the heavy-water detector at the Sudbury Neutrino Observatory. *Phys. Rev.*, C72:055502, 2005.

[24] Super-Kamiokande Collaboration. Solar neutrino measurements in super-kamiokande-i. *Phys. Rev. D*, 73:112001, Jun 2006.

[25] E. Kh Akhmedov, M. A Tortola, and J.W.F Valle. A simple analytic three-flavour description of the day-night effect in the solar neutrino flux. *Journal of High Energy Physics*, 2004(05):057–057, may 2004.

[26] P. C. de Holanda, Wei Liao, and A. Yu. Smirnov. Toward precision measurements in solar neutrinos. *Nucl. Phys.*, B702:307–332, 2004.

[27] Samoil M. Bilenky, C. Giunti, and W. Grimus. Phenomenology of neutrino oscillations. *Prog. Part. Nucl. Phys.*, 43:1–86, 1999.

[28] John N. Bahcall, Aldo M. Serenelli, and Sarbani Basu. New solar opacities, abundances, helioseismology, and neutrino fluxes. *Astrophys. J.*, 621:L85–L88, 2005.

[29] N. Schmitz. *Neutrinophysik*. Springer, 1997.

[30] M. Agostini et al. First Simultaneous Precision Spectroscopy of pp, ^{7}Be, and pep Solar Neutrinos with Borexino Phase-II. 2017.

[31] G Bellini et al.(Borexino Collaboration). Measurement of the solar ^{8}b neutrino rate with a liquid scintillator target and 3mev energy threshold in the borexino detector. *Phys. Rev. D*, 2010.

[32] G Bellini et al.(Borexino Collaboration). First evidence of pep solar neutrinos by direct detection in borexino. *Phys. Rev. Lett.*, 2012.

[33] E. G. et. al. Adelberger. Solar fusion cross sections. ii. the pp chain and cno cycles. *Rev. Mod. Phys.*, 83:195–245, Apr 2011.

[34] H. A. Bethe. Energy production in stars. *Phys. Rev.*, 55:434–456, Mar 1939.

[35] John N. Bahcall and M. H. Pinsonneault. What do we (not) know theoretically about solar neutrino fluxes? *Phys. Rev. Lett.*, 92:121301, 2004.

[36] Martin Asplund, Nicolas Grevesse, and Jacques Sauval. The Solar chemical composition. *Nucl. Phys.*, A777:1–4, 2006. [ASP Conf. Ser.336,25(2005)].

[37] Sunny Vagnozzi. New solar metallicity measurements. *arXiv e-prints*, page arXiv:1703.10834, Mar 2017.

[38] C. Amsler. *Kern- und Teilchenphysik*. vdf Hochschulverlag AG, 2007.

[39] Fumihiko Suekane. *Neutrino Oscillations: A Practical Guide to Basics and Applications*, volume 898. 2015.

[40] Y. Abe et al. Improved measurements of the neutrino mixing angle θ_{13} with the Double Chooz detector. *JHEP*, 10:086, 2014. [Erratum: JHEP 02, 074 (2015)].

[41] Myoung Youl Pac. Recent Results from RENO. *PoS*, NuFact2017:038, 2018.

[42] Haoqi Lu. Recent results from daya bay reactor neutrino experiment. *Journal of Physics: Conference Series*, 1342(1):012032, jan 2020.

[43] Angel Abusleme et al. TAO Conceptual Design Report: A Precision Measurement of the Reactor Antineutrino Spectrum with Sub-percent Energy Resolution. 5 2020.

[44] S. Gariazzo, C. Giunti, M. Laveder, Y. F. Li, and E. M. Zavanin. Light sterile neutrinos. *J. Phys. G*, 43:033001, 2016.

[45] J. Schechter and J. W. F. Valle. Neutrino masses in su(2) $\bigotimes$ u(1) theories. *Phys. Rev. D*, 22:2227–2235, Nov 1980.

[46] A. Aguilar, L. B. Auerbach, R. L. Burman, D. O. Caldwell, E. D. Church, A. K. Cochran, J. B. Donahue, A. Fazely, G. T. Garvey, R. M. Gunasingha, R. Imlay, W. C. Louis, R. Majkic, A. Malik, W. Metcalf, G. B. Mills, V. Sandberg, D. Smith, I. Stancu, M. Sung, R. Tayloe, G. J. VanDalen, W. Vernon, N. Wadia, D. H. White, and S. Yellin. Evidence for neutrino oscillations from the observation of $\overline{\nu}_{\mathrm{e}}$ appearance in a $\overline{\nu}_{\mu}$ beam. *Phys. Rev. D*, 64:112007, Nov 2001.

[47] Laurent Canetti, Marco Drewes, and Mikhail Shaposhnikov. Matter and Antimatter in the Universe. *New J. Phys.*, 14:095012, 2012.

[48] M. Drewes et al. A White Paper on keV Sterile Neutrino Dark Matter. *JCAP*, 01:025, 2017.

[49] A. Aguilar-Arevalo et al. Evidence for neutrino oscillations from the observation of $\bar{\nu}_{\mathrm{e}}$ appearance in a $\bar{\nu}_{\mu}$ beam. *Phys. Rev. D*, 64:112007, 2001.

[50] A. Aguilar-Arevalo et al. MiniBooNE collaboration. Search for electron neutrino appearance at the $\Delta\mathrm{m}^2 \sim 1$ ev^2 scale. *Phys. Rev. Lett.*, 98:231801, Jun 2007.

[51] Th. A. Mueller, D. Lhuillier, M. Fallot, A. Letourneau, S. Cormon, M. Fechner, L. Giot, T. Lasserre, J. Martino, G. Mention, A. Porta, and F. Yermia. Improved predictions of reactor antineutrino spectra. *Phys. Rev. C*, 83:054615, May 2011.

[52] Carlo Giunti and T. Lasserre. eV-scale Sterile Neutrinos. *Ann. Rev. Nucl. Part. Sci.*, 69:163–190, 2019.

[53] W. Hampel et al. GALLEX solar neutrino observations: Results for GALLEX IV. *Phys. Lett.*, B447:127–133, 1999.

[54] J. N. Abdurashitov et al. Solar neutrino flux measurements by the Soviet-American Gallium Experiment (SAGE) for half the 22 year solar cycle. *J. Exp. Theor. Phys.*, 95:181–193, 2002. [Zh. Eksp. Teor. Fiz.122,211(2002)].

[55] Bruce T. Cleveland, Timothy Daily, Jr. Raymond Davis, James R. Distel, Kenneth Lande, C. K. Lee, Paul S. Wildenhain, and Jack Ullman. Measurement of the solar electron neutrino flux with the homestake chlorine detector. *The Astrophysical Journal*, 496(1):505–526, mar 1998.

[56] M. Altmann et al. Complete results for five years of GNO solar neutrino observations. *Phys. Lett.*, B616:174–190, 2005.

[57] Takaaki Kajita. Atmospheric neutrino results from Super-Kamiokande and Kamiokande: Evidence for neutrino(mu) oscillations. *Nucl. Phys. Proc. Suppl.*, 77:123–132, 1999. [,123(1998)].

[58] Earle L. Lomon. Classical electrodynamics. john david jackson. wiley, new york, 1962. xvii + 641 pp. illus. 13. *Science*, 136(3521):1046–1047, 1962.

[59] Michael Wurm. *Cosmic Background Discrimination for the Rare Neutrino Event Search in Borexino and LENA*. PhD thesis, TU München, 2009.

[60] K. Abe et al. Solar Neutrino Measurements in Super-Kamiokande-IV. *Phys. Rev.*, D94(5):052010, 2016.

[61] J. D. Jackson. *Classical Electrodynamics*. Wiley, New York, 1962.

[62] R. S. Raghavan, Sandip Pakvasa, and B. A. Brown. New tools for solving the solar-neutrino problem. *Phys. Rev. Lett.*, 57:1801–1804, Oct 1986.

[63] G. Alimonti et al. A large-scale low-background liquid scintillation detector: the counting test facility at gran sasso. *Nuclear Instruments and Methods in Physics Research Section A: Accelerators, Spectrometers, Detectors and Associated Equipment*, 406(3):411 – 426, 1998.

[64] C et al. Arpesella. First real time detection of 7be solar neutrinos by borexino. *Physics Letters B*, 658:101–108, 01 2008.

[65] Vincenz Felix Maria Zimmer. *Studies of Proton Recoils in Organic Liquid Scintillators Used in Present and Future Neutrino Experiments.* PhD thesis, TU München, 2015.

[66] G Bellini et al.(Borexino Collaboration). Final results of borexino phase-i on low energy solar neutrino spectroscopy. arXiv:1308.0443v1 [hep-ex] 2 Aug 2013.

[67] D. Bravo-Berguno et al. The Borexino Thermal Monitoring & Management System and simulations of the fluid-dynamics of the Borexino detector under asymmetrical, changing boundary conditions. *Nucl. Instrum. Meth.*, A885:38–53, 2018.

[68] G Bellini et al.(Borexino Collaboration). Precision measurement of the ^{7}be solar neutrino interaction rate in borexino. *Phys. Rev. Lett.*, 2011.

[69] G. Bellini et al. Observation of Geo-Neutrinos. *Phys. Lett.*, B687:299–304, 2010.

[70] G Bellini et al.(Borexino Collaboration). Measurement of geo-neutrinos from 1353 days of borexino. *Phys. Lett. B*, 2013.

[71] G Bellini et al.(Borexino Collaboration). Absence of a day–night asymmetry in the ^{7}Be solar neutrino rate in Borexino. *Phys. Lett. B*, 2012.

[72] Aldo M. Serenelli, W. C. Haxton, and Carlos Pena-Garay. Solar models with accretion. I. Application to the solar abundance problem. *Astrophys. J.*, 743:24, 2011.

[73] B. Aharmim et al. (SNO Collaboration). Low-energy-threshold analysis of the phase i and phase ii data sets of the sudbury neutrino observatory. *Phys. Rev. C*, 2010.

[74] J. P. et. al. Cravens. Solar neutrino measurements in super-kamiokande-ii. *Phys. Rev. D*, 78:032002, Aug 2008.

[75] G. Bellini et al. Neutrinos from the primary proton proton fusion process in the Sun. *Nature*, 512(7515):383–386, 2014.

[76] Ondrej Sramek, William F. McDonough, Edwin S. Kite, Vedran Lekic, Steve Dye, and Shijie Zhong. Geophysical and geochemical constraints on geoneutrino fluxes from Earth's mantle. *Earth Planet. Sci. Lett.*, 361:356–366, 2013.

[77] J. H. Davies and D. R. Davies. Earth's surface heat flux. *Solid Earth*, 1(1):5–24, 2010.

[78] M. Agostini et al. Comprehensive geoneutrino analysis with Borexino. 2019.

[79] Kei Kotake, Katsuhiko Sato, and Keitaro Takahashi. Explosion mechanism, neutrino burst, and gravitational wave in core-collapse supernovae. *Rept. Prog. Phys.*, 69:971–1144, 2006.

[80] M. Ikeda et. al. Search for supernova neutrino bursts at super-kamiokande. *The Astrophysical Journal*, 669(1):519–524, nov 2007.

[81] N. Yu. Agafonova et al. On-line recognition of supernova neutrino bursts in the LVD detector. *Astropart. Phys.*, 28:516–522, 2008.

[82] IceCube Collaboration. Icecube sensitivity for low-energy neutrinos from nearby supernovae. *A&A*, 535:A109, 2011.

[83] Richard Saldanha. *Precision Measurement of the ^{7}Be Solar Neutrino Interaction Rate in Borexino.* PhD thesis, Princeton University, 2012.

[84] Oleg Smirnov. Experimental aspects of geoneutrino detection: Status and perspectives, 10 2019.

[85] Johannes Quirin Meindl. *Reconstruction and Measurement of Cosmogenic Signals in the Neutrino Experiment Borexino.* PhD thesis, TU München, 2013.

[86] Andrea Pocar et al. A scintillator purification system for the borexino solar neutrino detector. *Nuclear Instruments and Methods in Physics Research*, 2008.

[87] J. Benziger, L. Cadonati, F. Calaprice, M. Chen, A. Corsi, F. Dalnoki-Veress, R. Fernholz, R. Ford, C. Galbiati, A. Goretti, and et al. A scintillator purification system for the borexino solar neutrino detector. *Nuclear Instruments and Methods in Physics Research Section*

A: Accelerators, Spectrometers, Detectors and Associated Equipment, 587(2-3):277–291, Mar 2008.

[88] Yves Lemiere. Search for evidence of lepton number violation by neutrinoless double beta decay process from 82se and 150nd in nemo-3 experiment. bi-po decay study from thoron chain. 09 2008.

[89] M. Agostini et al. Improved measurement of ^{8}B solar neutrinos with 1.5kt – y of Borexino exposure. *Phys. Rev. D*, 101(6):062001, 2020.

[90] H Back et al.(Borexino Collaboration). Borexino calibrations: hardware, methods, and results. *Journal of Instrumentation*, 2012.

[91] T. Enqvist et al. Measurements of muon flux in the Pyhasalmi underground laboratory. *Nucl. Instrum. Meth.*, A554:286–290, 2005.

[92] M. et al. Ambrosio. Measurement of the residual energy of muons in the gran sasso underground laboratories. *Astroparticle Physics*, 19:313–328, 06 2003.

[93] G Bellini et al.(Borexino Collaboration). Muon and cosmogenic neutron detection in borexino. *Journal of Instrumentation 6*, 2011. Reprinted by permission of the American Astronomical Society.

[94] Dominik Jeschke. *Modulations of the Cosmic Muon Flux & Identification of Atmospheric Neutrino Interactions in Borexino*. PhD thesis, TU München, 2018.

[95] G. Bellini et al. (Borexino Collaboration). Cosmogenic backgrounds in borexino at 3800 m water-equivalent depth. arXiv:1304.7381v2.

[96] B. Blank et al. Branching ratio of the super-allowed β decay of ^{10}C. *Eur. Phys. J. A*, 56(6):156, 2020.

[97] Davide D'Angelo. *Towards the detection of low energy solar neutrinos in BOREXino: data readout, data reconstruction and background identification*. PhD thesis, TU München, 2006.

[98] Richard B Firestone, Coral Baglin, and S Y Frank Chu. *Table of isotopes: 1998 update with CD-ROM*. Wiley, New York, NY, 1998.

[99] S. Abe et al. Production of Radioactive Isotopes through Cosmic Muon Spallation in KamLAND. *Phys. Rev. C*, 81:025807, 2010.

[100] T. Hagner, R. von Hentig, B. Heisinger, L. Oberauer, S. Schönert, F. von Feilitzsch, and E. Nolte. Muon-induced production of radioactive isotopes in scintillation detectors. *Astroparticle Physics*, 14(1):33–47, 2000.

[101] E. G. Adelberger et al. Solar fusion cross sections. ii. the pp chain and cno cycles. *Rev. Mod. Phys.*, Apr 2011.

[102] M. Agostini et al. The Monte Carlo simulation of the Borexino detector. *Astropart. Phys.*, 97:136–159, 2018.

[103] Wouter Verkerke and David P. Kirkby. The RooFit toolkit for data modeling. *eConf*, C0303241:MOLT007, 2003.

[104] J. Benziger, L. Cadonati, F. Calaprice, E. de Haas, R. Fernholz, R. Ford, C. Galbiati, A. Goretti, E. Harding, A. Ianni, An. Ianni, S. Kidner, M. Leung, F. Loeser, K. McCarty, A. Nelson, R. Parsells, A. Pocar, T. Shutt, A. Sonnenschein, and R.B. Vogelaar. The nylon scintillator containment vessels for the borexino solar neutrino experiment. *Nuclear Instruments and Methods in Physics Research Section A: Accelerators, Spectrometers, Detectors and Associated Equipment*, 582(2):509–534, 2007.

[105] J. Bahacall. Solar neutrino energy spectrum. http://www.sns.ias.edu/ jnb/.

[106] W. T. Winter, S. J. Freedman, K. E. Rehm, and J. P. Schiffer. The B-8 neutrino spectrum. *Phys. Rev. C*, 73:025503, 2006.

[107] John N. Bahcall, Marc Kamionkowski, and Alberto Sirlin. Solar neutrinos: Radiative corrections in neutrino - electron scattering experiments. *Phys. Rev. D*, 51:6146–6158, 1995.

[108] P. C. de Holanda and A. Yu. Smirnov. Solar neutrino spectrum, sterile neutrinos and additional radiation in the Universe. *Phys. Rev. D*, 83:113011, 2011.

[109] Alexander Friedland, Cecilia Lunardini, and Carlos Pena-Garay. Solar neutrinos as probes of neutrino matter interactions. *Phys. Lett. B*, 594:347, 2004.

[110] M. Askins et al. THEIA: an advanced optical neutrino detector. *Eur. Phys. J. C*, 80(5):416, 2020.

[111] Babak Abi et al. Deep Underground Neutrino Experiment (DUNE), Far Detector Technical Design Report, Volume I Introduction to DUNE. *JINST*, 15(08):T08008, 2020.

[112] Fengpeng An et al. Neutrino Physics with JUNO. *J. Phys.*, G43(3):030401, 2016.

[113] Christoph Genster, Michaela Schever, Livia Ludhova, Michael Soiron, Achim Stahl, and Christopher Wiebusch. . *JINST*, 13(03):T03003, 2018.

[114] T. Adam, E. Baussan, K. Borer, J. E. Campagne, N. Chon-Sen, C. de La Taille, N. Dick, M. Dracos, G. Gaudiot, and T. Goeltzenlichter. The OPERA experiment Target Tracker. *Nuclear Instruments and Methods in Physics Research A*, 577(3):523–539, Jul 2007.

[115] A. Gando et al. ^{7}Be Solar Neutrino Measurement with KamLAND. *Phys. Rev.*, C92(5):055808, 2015.

[116] Sebastian Zwickel. Studies on solar ^{7}be neutrino measurements and applications in juno. Masterthesis TU München, 2021.

[117] Juno Collaboration Angel Abusleme et al. Feasibility and physics potential of detecting ^{8}b solar neutrinos at JUNO. *Chinese Physics C*, 45(2):023004, feb 2021.

[118] P. Lombardi et al. Distillation and stripping pilot plants for the JUNO neutrino detector: Design, operations and reliability. *Nucl. Instrum. Meth. A*, 925:6–17, 2019.

[119] Alexandre Göttel. OSIRIS - A 20 ton liquid scintillator detector as a radioactivity monitor for JUNO. The XXIX International Conference on Neutrino Physics and Astrophysics, Chicago (US), 22 Jun 2020 - 2 Jul 2020, Jun 2020.

[120] H. de Kerret et al. Yields and production rates of cosmogenic ^{9}Li and ^{8}He measured with the Double Chooz near and far detectors. *JHEP*, 11:053, 2018.

[121] M. Apollonio et al. Search for neutrino oscillations on a long baseline at the CHOOZ nuclear power station. *Eur. Phys. J. C*, 27:331–374, 2003.

[122] Michael Franke. *The neutrino experiment Double Chooz and data analysis with the near detector*. Dissertation, Technische Universität München, München, 2016.

[123] H. de Kerret et al. The Double Chooz antineutrino detectors. 1 2022.

[124] H. de Kerret et al. Double Chooz θ_{13} measurement via total neutron capture detection. *Nature Phys.*, 16(5):558–564, 2020.

[125] T. Abrahão et al. Search for signatures of sterile neutrinos with Double Chooz. *Eur. Phys. J. C*, 81(8):775, 2021.

[126] Alessandro Strumia and Francesco Vissani. Precise quasielastic neutrino/nucleon cross-section. *Phys. Lett. B*, 564:42–54, 2003.

[127] F. et al. Boehm. Results from the palo verde neutrino oscillation experiment. *Physical Review D*, 62, 03 2000.

[128] D. et al. Adey. Measurement of the electron antineutrino oscillation with 1958 days of operation at daya bay. *Phys. Rev. Lett.*, 121:241805, Dec 2018.

[129] G. et al. Bak. Measurement of reactor antineutrino oscillation amplitude and frequency at reno. *Phys. Rev. Lett.*, 121:201801, Nov 2018.

[130] K. et al. Abe. Search for cp violation in neutrino and antineutrino oscillations by the t2k experiment with 2.2×10^{21} protons on target. *Phys. Rev. Lett.*, 121:171802, Oct 2018.

[131] Truesense s310 description. `https://www.lasertech.com/TruSense-S300-Laser-Sensor-Series.aspx`. Accessed: 2022-01-12.

[132] Patrick Pfahler. *Realization of the low background neutrino detector Double Chooz: From the development of a high-purity liquid & gas handling concept to first neutrino data*. Dissertation, Technische Universität München, München, 2012.

[133] Gvs disposal company. `https://gvs-ma.de/Verwertung-und-Beseitigung/`. Accessed: 2022-01-12.

[134] Y. J. et al. Ko. Sterile neutrino search at the neos experiment. *Phys. Rev. Lett.*, 118:121802, Mar 2017.

[135] I Alekseev et al. Search for sterile neutrinos at the DANSS experiment. *Phys. Lett. B*, 787:56–63, 2018.

[136] S. Gariazzo, C. Giunti, M. Laveder, and Y. F. Li. Model-independent $\bar{\nu}_e$ short-baseline oscillations from reactor spectral ratios. *Phys. Lett. B*, 782:13–21, 2018.

[137] Sebastian Böser, Christian Buck, Carlo Giunti, Julien Lesgourgues, Livia Ludhova, Susanne Mertens, Anne Schukraft, and Michael Wurm. Status of Light Sterile Neutrino Searches. *Prog. Part. Nucl. Phys.*, 111:103736, 2020.

[138] Y. Declais et al. Search for neutrino oscillations at 15-meters, 40-meters, and 95-meters from a nuclear power reactor at Bugey. *Nucl. Phys. B*, 434:503–534, 1995.

[139] J. et al. Ashenfelter. First search for short-baseline neutrino oscillations at hfir with prospect. *Phys. Rev. Lett.*, 121:251802, Dec 2018.

[140] C. Giunti. Statistical significance of reactor antineutrino active-sterile oscillations. *Phys. Rev. D*, 101:095025, May 2020.

[141] A. P. Serebrov et al. Search for sterile neutrinos with the Neutrino-4 experiment and measurement results. *Phys. Rev. D*, 104(3):032003, 2021.

[142] M. Andriamirado et al. Note on arXiv:2005.05301, 'Preparation of the Neutrino-4 experiment on search for sterile neutrino and the obtained results of measurements'. 6 2020.

[143] Mona et al. Dentler. Updated global analysis of neutrino oscillations in the presence of ev-scale sterile neutrinos. *JHEP*, 08:010, 2018.

[144] A. A. Aguilar-Arevalo et al. Updated MiniBooNE neutrino oscillation results with increased data and new background studies. *Phys. Rev. D*, 103(5):052002, 2021.

[145] G. Mention, M. Fechner, Th. Lasserre, Th. A. Mueller, D. Lhuillier, M. Cribier, and A. Letourneau. Reactor antineutrino anomaly. *Phys. Rev. D*, 83:073006, Apr 2011.

[146] M. Andriamirado et al. Improved short-baseline neutrino oscillation search and energy spectrum measurement with the PROSPECT experiment at HFIR. *Phys. Rev. D*, 103(3):032001, 2021.

[147] Mikhail Danilov. Recent results of the DANSS experiment. *PoS*, EPS-HEP2019:401, 2020.

[148] P. et al. Adamson. Improved constraints on sterile neutrino mixing from disappearance searches in the minos, MINOS+, daya bay, and bugey-3 experiments. *Phys. Rev. Lett.*, 125:071801, Aug 2020.

[149] H. Almazán et al. Improved sterile neutrino constraints from the STEREO experiment with 179 days of reactor-on data. *Phys. Rev. D*, 102(5):052002, 2020.

[150] M. et al. Agostini. Final results of gerda on the search for neutrinoless double-β decay. *Phys. Rev. Lett.*, 125:252502, Dec 2020.

[151] M. Aker et al. Improved eV-scale sterile-neutrino constraints from the second KATRIN measurement campaign. *Phys. Rev. D*, 105(7):072004, 2022.

[152] A. Diaz, C. A. Argüelles, G. H. Collin, J. M. Conrad, and M. H. Shaevitz. Where Are We With Light Sterile Neutrinos? *Phys. Rept.*, 884:1–59, 2020.

[153] P. et al. Adamson. Search for sterile neutrinos in minos and minos+ using a two-detector fit. *Phys. Rev. Lett.*, 122:091803, Mar 2019.

[154] M. G. et al. Aartsen. ev-scale sterile neutrino search using eight years of atmospheric muon neutrino data from the icecube neutrino observatory. *Phys. Rev. Lett.*, 125:141801, Sep 2020.

[155] Alexander Merle, Stefano Morisi, and Walter Winter. Common origin of reactor and sterile neutrino mixing. *JHEP*, 07:039, 2014.

[156] K. S. Babu, D. W. McKay, Irina Mocioiu, and Sandip Pakvasa. Light sterile neutrinos, lepton number violating interactions and short baseline neutrino experiments. *AIP Conference Proceedings*, 1743(1):030007, 2016.

[157] Marcela Carena, Ying-Ying Li, Camila S. Machado, Pedro A. N. Machado, and Carlos E. M. Wagner. Neutrinos in large extra dimensions and short-baseline ν_{e} appearance. *Phys. Rev. D*, 96:095014, Nov 2017.

[158] Jiajun Liao, Danny Marfatia, and Kerry Whisnant. MiniBooNE, MINOS+ and IceCube data imply a baroque neutrino sector. *Phys. Rev. D*, 99(1):015016, 2019.

[159] Peter B. Denton, Yasaman Farzan, and Ian M. Shoemaker. Activating the fourth neutrino of the $3+1$ scheme. *Phys. Rev. D*, 99:035003, Feb 2019.

[160] J. Kostensalo, J. Suhonen, C. Giunti, and P.C. Srivastava. The gallium anomaly revisited. *Physics Letters B*, 795:542–547, 2019.

[161] J. H. et al. Choi. Observation of energy and baseline dependent reactor antineutrino disappearance in the reno experiment. *Phys. Rev. Lett.*, 116:211801, May 2016.

[162] Feng Peng An et al. Measurement of the Reactor Antineutrino Flux and Spectrum at Daya Bay. *Phys. Rev. Lett.*, 116(6):061801, 2016. [Erratum: Phys.Rev.Lett. 118, 099902 (2017)].

[163] L. Hayen, J. Kostensalo, N. Severijns, and J. Suhonen. First-forbidden transitions in the reactor anomaly. *Phys. Rev. C*, 100:054323, Nov 2019.

[164] M. Estienne, M. Fallot, A. Algora, J. Briz-Monago, V. M. Bui, S. Cormon, W. Gelletly, L. Giot, V. Guadilla, D. Jordan, L. Le Meur, A. Porta, S. Rice, B. Rubio, J. L. Taín, E. Valencia, and A.-A. Zakari-Issoufou. Updated summation model: An improved agreement with the daya bay antineutrino fluxes. *Phys. Rev. Lett.*, 123:022502, Jul 2019.

[165] Jeffrey M. Berryman and Patrick Huber. Reevaluating reactor antineutrino anomalies with updated flux predictions. *Phys. Rev. D*, 101:015008, Jan 2020.

[166] A. A. Aguilar-Arevalo et al. Significant Excess of ElectronLike Events in the MiniBooNE Short-Baseline Neutrino Experiment. *Phys. Rev. Lett.*, 121(22):221801, 2018.

Danksagung

An dieser Stelle möchte ich mich noch bei allen bedanken, ohne die diese Arbeit so nicht möglich gewesen wäre. An erster Stelle möchte ich mich bei meinen Professoren Stefan Schönert und Lothar Oberauer für die Aufnahme am Lehrstuhl und die Möglichkeit zur Promotion bedanken. Ein besonderer Dank geht dabei an meinen Doktorvater Lothar Oberauer für seine hervorragende Betreuung. Er war sehr geduldig mit mir und hat mir die lange Promotion ermöglicht hat. Neben physikalischen Themen kann man mit ihm auch wunderbar über die Berge und die 60er philosophieren.
Ein großer Dank geht auch an Dominik Jeschke, der mich stets bei technischen Problemen unterstützt hat und sich für viele Diskussionen Zeit nahm. Am meisten werden unsere Fahrten nach Kochel und Franken in Erinnerung bleiben.
Ein weiterer Dank geht an Birgit Neumair für unsere unterhaltsamen Dienstreisen nach Paris.
Des weiteren möchte ich mich bei meinen zahlreichen Bürokollegen Konstantin Schweizer, Julia Sawatzki, Randolph Möllenberg, Nils Haag, Martin Hoffmann, Dominikus Hellgartner, Alexander Neumeier, Sebastian Zwickel und Simon Csakli für die immer sehr entspannte und freundschaftliche Arbeitsatmosphäre bedanken. Im Büro herrschte immer gute Stimmung und es wurde bei allen Problemen schnell geholfen.
Vielen Dank auch an unsere Sekretärinen Paola Mucciarelli, Sabine Wenzel, Sabine Kaps und Maria Bremberger für das Lösen aller bürokratischer Probleme.
Ein besonderer Dank auch an unsere Werkstatt Harald Hess, Lukas Hein, Georg Lerchl und Thomas Richter die mir sehr oft kurzfristig meine Bauteile anfertigen konnten.
Vielen Dank auch an alle aus dem Lehrstuhl E15 die hier namentlich nicht erwähnt werden für die gute Stimmung am Lehrstuhl und die freundliche Aufnahme.
A big thanks goes to my colleagues from the Borexino and Double Chooz collaborations for the nice times at Gran Sasso and Chooz. A special thank

you goes to everyone who was involved in the very stressful filling and unfilling of the Double Chooz detector.
Der größte Dank geht an meine Familie und meine Freundin Stefanie Rauchstein. Ohne ihre Unterstützung und Geduld wäre diese Doktorarbeit nicht möglich gewesen.